FRIEDRICH-SCHILLER-UNIVERSITÄT JENA

Physikalisch-Astronomische Fakultät

HI JENA

HELMHOLTZ

Helmholtz-Institut Jena

Probing the Impulse Approximation via Polarization Studies on Inelastically Scattered Hard X-Rays

Masterarbeit

FRIEDRICH-SCHILLER-UNIVERSITÄT JENA
PHYSIKALISCH-ASTRONOMISCHE FAKULTÄT
HELMHOLTZ-INSTITUT JENA

eingereicht von

Tobias Over

Gutachter

1. Gutachter: Prof. Dr. rer. nat. Thomas Stöhlker

2. Gutachter: Dr. rer. nat. Günter Weber

Contents

1 Introduction

Inelastic scattering is a fundamental interaction process between photons and matter. In spectroscopy, this scattering process is utilized to analyze the structure of material. Raman spectroscopy [1], for example, is used in the soft x-ray region to analyze the structure of substances. At higher photon energies, Compton scattering is more dominant. It is named after Arthur H. Compton, who published his ideas in 1923 [2, 3], for which he was awarded with the Nobel Prize in 1927 and describes the inelastic scattering of a photon on a free electron. The Compton effect is widely employed in Compton polarimetry to analyze the polarization of photons [4, 5]. To investigate the polarization characteristic of the light emitted by astronomical objects, Compton polarimetry is used in astrophysical polarization measurements [6–8]. Bright sources, such as the crab, are favorable for these measurements, as many photons are necessary for the polarization analysis [9, 10]. In addition to astronomical sources, experiments with various photon sources are also performed in the laboratory to investigate the polarization characteristics of scattered photons. This can provide a better understanding of the measured signals, which originate from a particularly large distance. Due to technological difficulties, highly polarized photon sources were not available for a long time. The effort to use radioactive sources in a safe working environment with a high intensity of hard x-rays in a small solid angle is enormous. Furthermore, the emitted radiation is not completely polarized. This can be circumvented with synchrotron radiation sources. They are able to provide a monoenergetic and very intense hard x-ray beam with a high degree of linear polarization.

In this thesis, the polarization characteristics of photons being Compton scattered of atomically bound electrons are investigated. Of particular interest is the behavior of the polarization across the Compton peak, where the influence of the electron momentum on the transferred energy varies. This influence becomes stronger for electrons from lower shells with an increasing atomic number Z, since the momentum increase. Additionally, the number of electrons with a high binding energy relative to the photon energy also increases. Therefore, a gold foil ($Z = 79$) was employed as a high-Z scatterer. A common approximation for Compton scattering with bound electrons is the impulse approximation [11, 12]. Here, the bound electrons are treated as free electrons with a momentum distribution. This approximation is valid when the binding energy is much smaller than the energy of the recoil electron [13]. Thus, at the tails of the Compton peak, the validity of the impulse approximation is weakened.

The linear polarization of inelastically scattered photons originating from an initially highly linearly polarized hard x-ray beam was measured. In addition to a previous experiment [14], the detection was also performed outside of the reference plane. Two criteria are relevant for the choice of the initial photon energy. It should be larger than the binding energies of the electrons in the gold target. For the electrons in the K-shell, the binding energy is $\approx 80.7\,\text{keV}$ [15]. In addition, the efficiency of the detector is a limiting factor. A relatively high efficiency can be reached with the detector

used in the experiment for energies up to 300 keV [16]. Considering these two criteria, a photon energy of 175 keV was chosen. The experiment was conducted at the DESY (Deutsches Elektronen-Synchrotron) facility in Hamburg, Germany. Here, the third-generation synchrotron radiation source PETRA III (Positron-Electron-Tandem Ring Accelerator) provided the photon beam. A lithium-drifted silicon strip detector specially designed as a Compton polarimeter was used to measure the linear polarization. The availability of a high intensity photon source in combination with the polarimeter allows the analysis of the "polarization transfer".

The thesis is organized as follows: Section 2 contains the main physical concepts relevant to this thesis. Fundamental photon-matter interaction processes as well as polarization phenomena are explained. In section 3, the experiment is described. The setup, including the synchrotron source and the used detectors, are introduced. A detailed explanation of the analysis used is provided in section 4. This involves the generation of spectra and the calculation of the polarization of the scattered and incident beam. In section 5, the results are discussed. A summary of the thesis is given in section 6. Section 7 concludes this thesis with an outlook on further experiments.

2 Physical background

The main physical concepts underlying this thesis are introduced in the following section. In subsection 2.1 the different types of interactions between photons and matter are explained and subsection 2.2 focus on the description of photon polarization. Finally, the concept of Compton polarimetry is discussed in subsection 2.3.

2.1 Interaction between photons and matter

In the x-ray regime, photon-matter interaction consists of several basic interaction processes that are briefly discussed in the following. The most relevant process in this thesis is the Compton scattering. Furthermore, the photoelectric effect and the elastic scattering are relevant for the measurement and the data evaluation. Pair production, which is also an important interaction process, is not discussed here, since this process will not take place in the energy regime relevant for this thesis. Figure 2.1 shows the cross sections of the particular processes as well as the total cross section in gold.
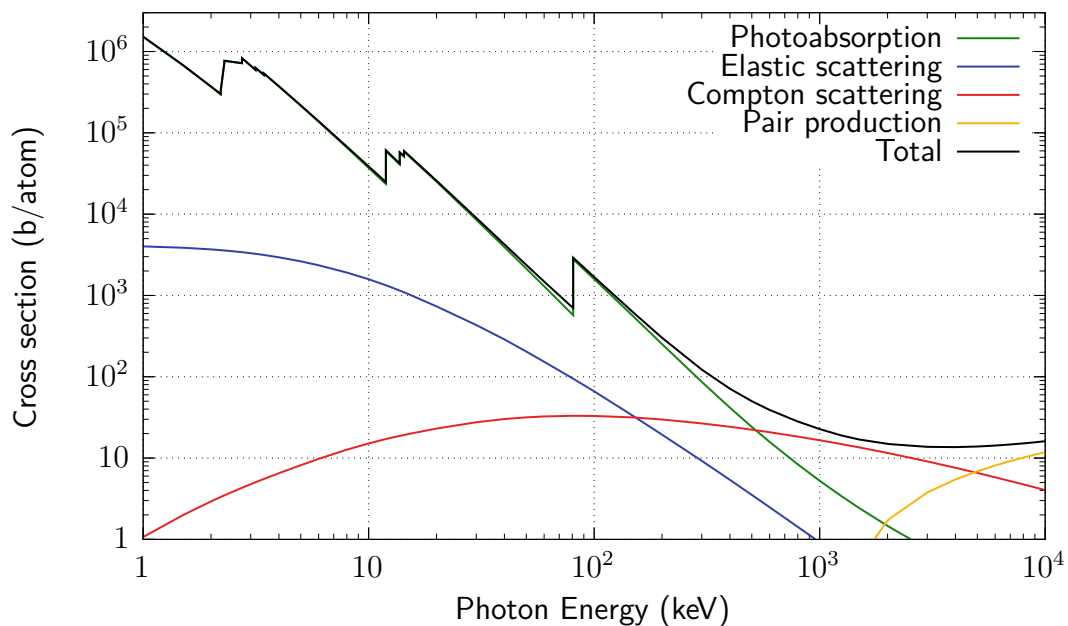
Figure 2.1: Cross sections for photon-matter interactions of x-rays in gold. Data are taken from [17].

2.1.1 Photoelectric effect

The photoelectric effect (or photoabsorption) was first explained in 1905 by Albert Einstein [18]. It is an important interaction process, whereby the energy of a photon $\hbar\omega$ is fully absorbed by an electron. Due to the conversation of momentum, this process can only occur for initially bound electrons where the nucleus takes over some of the momentum in form of a recoil. This increase in energy leads to an excitation

of the electron in a higher shell. Then the transferred energy is equal to the energy difference between these two shells. When the gain of energy is larger than the difference to the highest shell and therefore larger than the (negative) binding energy E_b, the electron is no longer bound and has a kinetic energy of $E_{kin} = \hbar\omega + E_b$ and the atom is ionized [19].

In figure 2.1 the photoelectric cross section of gold is shown in green. As can be seen, with increasing photon energy the cross section decreases. The decline is not continuous, it is interrupted by resonant structures. These interruptions appear at the binding energies of atomic shells and are referred to as absorption edges. Due to the fact that the innermost shell (K-shell) has the highest binding energy, the edge caused by this shell can be found as the last one from the high energy side at $-E_K$. The next lower absorption edge is consequently the L-edge from the L-shell at $-E_L$. The remaining edges follow this nomenclature. Photons whose energy is below a certain binding energy cannot interact with electrons from the corresponding shell so that the atom is ionized. Therefore the electrons from this shell do not contribute to the cross section in this energy range. When the photon energy overcomes this threshold, the cross section rises significantly and can be seen as an absorption edge. The Born approximation is valid for energies above the K-edge and in the non-relativistic regime, $-E_K < \hbar\omega \ll m_e c^2$, and can be applied to calculate the photoelectric cross section

$$\sigma_{photo} = \sigma_T \cdot 4\sqrt{2} \cdot \alpha^2 \cdot Z^5 \cdot \left(\frac{m_e c^2}{\hbar\omega}\right)^{\frac{7}{2}}, \tag{2.1}$$

with the fine structure constant $\alpha \approx 1/137$, the nuclear charge Z, the electron rest energy $m_e c^2 \approx 511\,\text{keV}$ and the Thomson cross section $\sigma_T \approx 0.665\,\text{b}$, see equation (2.2) [19].

The photoelectric effect plays an important role in choosing the detector and shielding material. Here, a high nuclear charge is favorable, as the Z^5 scaling in equation (2.1) indicates. Furthermore, this interaction process scales with the energy by $(\hbar\omega)^{-\frac{7}{2}}$. In this work two types of detectors were used. A polarimeter with silicon ($Z = 14$) and a detector with germanium ($Z = 32$) as active material (see 3.2.1 and 3.2.2). Lead ($Z = 82$) was used for shielding.

2.1.2   Elastic scattering

The characteristic of elastic photon scattering is that the energy of the photon does not change in the scattering process. In general, this is only applicable in the center-of-mass frame. For scattering by an atom and in the regime of photon energies below 10 MeV, the difference between center-of-mass and laboratory frame is negligible [20]. Elastic scattering of photons from a free point charge is called Thomson scattering. This process was first described by Joseph J. Thomson and is therefore named after him [21]. The corresponding cross section reads

$$\sigma_T = \frac{8}{3}\pi \cdot r_e^2 \tag{2.2}$$

with the classical electron radius $r_e = e^2 / (4\pi\varepsilon_0 m_e c^2) \approx 2.8 \cdot 10^{-13}$ cm depending on the elementary charge $e = 1.602 \cdot 10^{-19}$ C and the electric constant $\varepsilon_0 \approx 8.85 \cdot 10^{-12}$ C/(Vm) [19].

In comparison to Thomson scattering, the elastic scattering of photons by bound electrons is referred to as Rayleigh scattering. It is named after John W. Strutt, Lord Rayleigh III, who had worked on the scattering of light from air [22–24]. Since the 1930s atomic Rayleigh scattering of x-rays was researched [25]. The process is also called coherent scattering because all electrons of the atom interact coherently with the photon. In this coherent scattering process, the direction of the photon is changed and the atom is neither excited nor ionized [19].

Further elastic scattering processes are nuclear Thomson scattering, nuclear resonance scattering and Delbrück scattering. Whereby in the first process the photon scatters from an atomic nucleus and in the latter from a virtual electron-positron pair, which is created in the Coulomb field of the nucleus. For photon energies up to ≈ 1 MeV the dominant elastic scattering process is Rayleigh scattering [26]. The sum of all elastic scattering cross sections is shown in blue in figure 2.1. As can be seen, the cross section is strongly decreasing with rising photon energies.

2.1.3   Inelastic scattering

In contrast to elastic scattering, the energy of the photon changes in inelastic scattering. The process of scattering photons from free electrons at rest is called Compton scattering and is named after Arthur H. Compton, who discovered this effect [2, 3]. For this discovery he received the Nobel Prize in Physics in 1927.

After scattering, the energy of the photon is

$$\hbar\omega' = \frac{\hbar\omega}{1 + \frac{\hbar\omega}{m_e c^2} \cdot (1 - \cos(\theta))} \tag{2.3}$$

with the incident photon energy $\hbar\omega$, the electron rest mass m_e, the speed of light c and the angle θ (see figure 2.2) between the direction of the scattered and incident photon [19]. This results in the kinetic energy for the recoil electron of

$$E_{\text{kin}} = \hbar\omega - \hbar\omega'. \tag{2.4}$$

When the photon is backscattered, at $\theta = 180°$, the energy transfer is maximized and reaches

$$E_{\text{kin,max}} = \hbar\omega \frac{2k}{1 + 2k}, \tag{2.5}$$

with the energy expressed in units of $m_e c^2$

$$k = \frac{\hbar\omega}{m_e c^2}. \tag{2.6}$$

Equation (2.5) shows that for $k < \frac{1}{2}$ and thus for $\hbar\omega < \frac{m_e c^2}{2} \approx 255$ keV the kinetic energy of the electron is always smaller than the one of the scattered photon.

Figure 2.2 illustrates a Compton scattering process on a free electron at rest. The

reference plane is spanned by the x- and z-axis, in which the incident photon with energy $\hbar\omega$ (blue) propagates in the direction of the z-axis. The propagation of the scattered photon with energy $\hbar\omega'$ (yellow) is shifted by the polar angle θ with respect to the incident photon. Furthermore, the movement is in the scattering plane which is tilted by the azimuthal angle φ to the reference plane. The scattered electron propagates with the energy difference of the photon E_{kin} under the angle ψ with respect to the propagation direction of the reference plane.
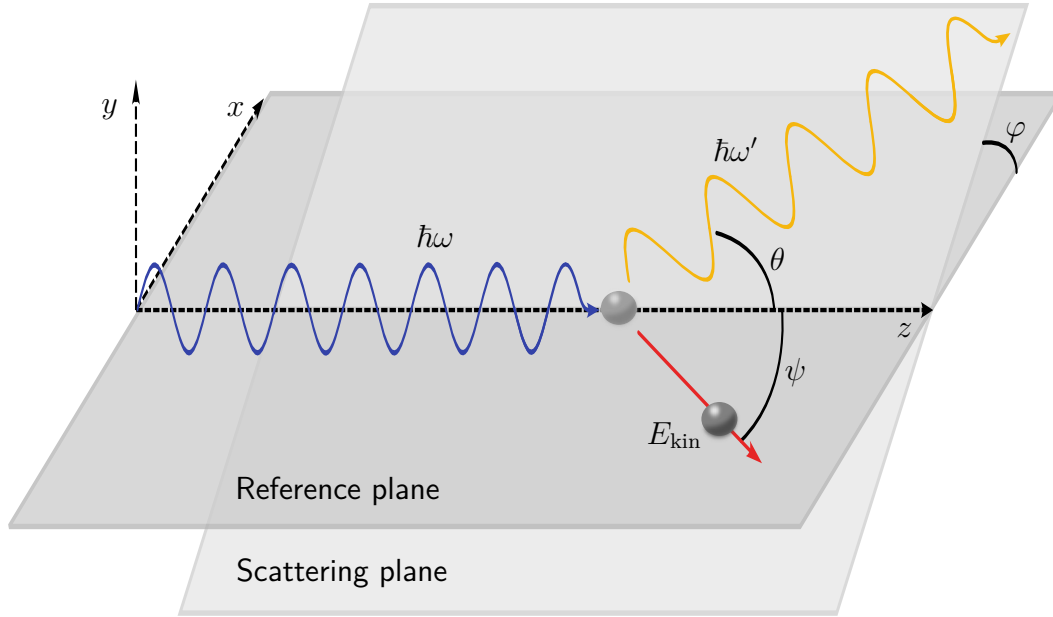
Figure 2.2: Schematic representation of the geometry of a photon undergoing Compton scattering on a free electron. With the polar angle θ, the azimuthal angle φ and the incident and scattered photon energy $\hbar\omega$ and $\hbar\omega'$, respectively. E_{kin} is the electron energy and ψ the angle between the propagation direction of the initial photon and the scattered electron in the scattering plane. A thorough description is provided in the text. Adapted from [27].

In 1929, Oskar Klein and Yoshio Nishina calculated the differential cross section for Compton scattering in the framework of QED (Quantum Electrodynamics) [28]. The determination depends on the electron spin as well as the initial and final photon polarization. For the calculation of the double-differential cross section, the following conditions are required. Both the final electron spin and the photon polarization are not observed. In addition, the electrons are initially unpolarized on average and the incident photons are linearly polarized in the reference plane. The double-differential Klein-Nishina cross section then reads

$$\left(\frac{\mathrm{d}\sigma}{\mathrm{d}\Omega}\right) = \frac{r_e^2}{2} \cdot \left(\frac{\hbar\omega'}{\hbar\omega}\right)^2 \cdot \left(\frac{\hbar\omega'}{\hbar\omega} + \frac{\hbar\omega}{\hbar\omega'} - 2\sin^2(\theta)\cos^2(\varphi)\right). \tag{2.7}$$

This cross section depends on the azimuthal angle φ, the polar angle θ, as well as the energy of the incident and scattered photon, $\hbar\omega$ and $\hbar\omega'$, respectively. In the case of unpolarized photons, the cross section only depends on θ, because the integration over φ in equation (2.7) leads to $\langle\cos^2(\varphi)\rangle \to \frac{1}{2}$. The polarization of the scattered photons and the scattering of partially polarized photon beams are not described by the Klein-Nishina formula (2.7). As these two scenarios are present in this thesis, the equation needs to be extended to include them, see subsection 2.2 regarding this.

When considering elastic scattering of photons by atomically bound electrons, the concept of the Compton effect needs to be extended. In this case, the energy of the recoil electron, given by equation (2.4), needs to overcome the binding energy for the electron to contribute to Compton scattering. As a result, the number of electrons per atom contributing to the total Compton cross section can differ for various angles θ and a constant initial photon energy [29]. Bound electrons have a momentum and therefore cause a Doppler broadening of the Compton peak.
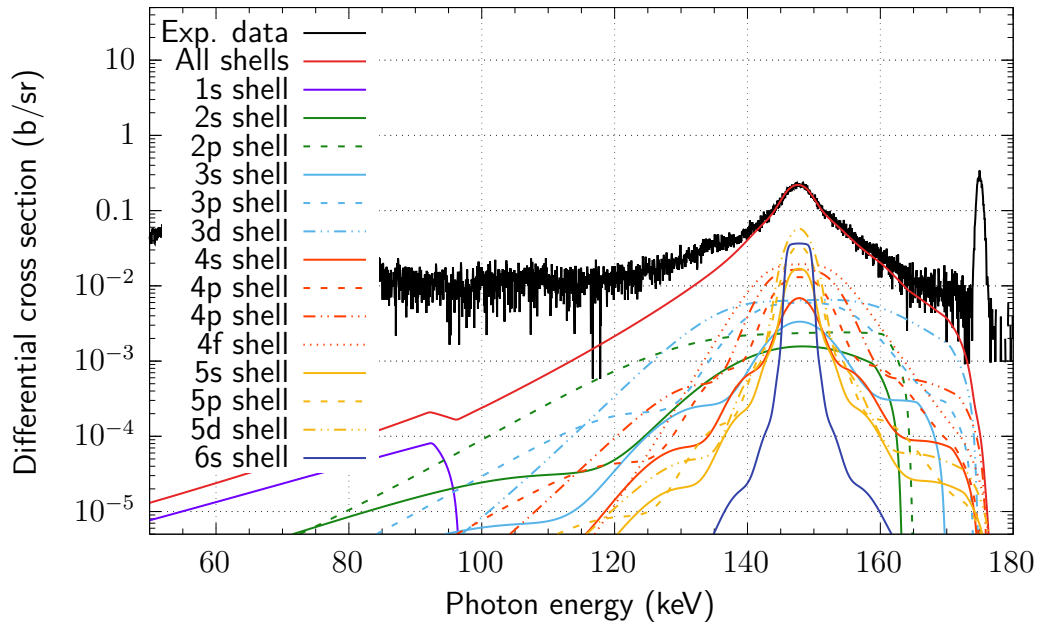
Figure 2.3: Differential cross section of Compton scattering for the individual shells of a gold atom with respect to the detected data (black). The sum of the contributions from all shells (red) is fitted to measured data. The detection was performed under the scattering angles $\theta = 63.3°$ and $\varphi = 0°$.

In figure 2.3, the influence of the individual shells on the broadening is displayed. The calculations, including the assumptions, are based on [30]. Due to the large ionization energy of the K-shell electrons, the contribution is limited to below the difference between the initial beam energy and the ionization energy. In contrast to this, the outermost shell contributes only in a narrow region around the center of the Compton peak, since the maximum electron momentum decreases for higher shells. The peak structure for the more inwards shells becomes broader with increasing elec-

tron momentum. Therefore, the dominant fraction at the edges of the Compton peak originates from lower shells, as can be seen in figure 2.3. Consequently, from Compton events with a high momentum transfer. By the width of the momentum distribution of all atomically bound electrons of the target, the broadening of the peak is defined [31]. Thus, equation (2.3) is no longer completely valid for a given polar scattering angle θ. This effect decreases for high Z materials, since more weakly bound electrons are available for scattering. Due to these difficulties, Compton scattering from weakly bound electrons can be described more simply.

First applied by DuMond in 1929 [32], in the impulse approximation, the weakly bound electrons are treated like free electrons with a momentum distribution. This distribution results from a bound electron wave function [29]. It leads to a broadening of the Compton peak. Due to the various velocity differences between the photons and the electrons, the Doppler effect occurs and causes this phenomenon [33]. The assumption to treat the bound electrons as free is based on the expectation that the interaction is so short that the other electrons will not react before the end of the scattering process. Consequently, the potential seen by the electron before and shortly after the interaction is the same and can be neglected. The irrelevance of the potential is equivalent to the assumption that the photon scatters at an individual free electron, which has a finite momentum greater zero [34]. For the case that the binding energy is much smaller than the recoil energy of the electron, the impulse approximation is valid. The closer the ratio between these two energies is to unity, the greater the influence of the binding and the worse this approximation becomes [13]. In the peak region a good agreement could be found to experimental data [13, 32, 33]. For a relativistic treatment see [35].

Another, more complex and relativistic approach is the independent particle approximation. For further explanations see [36, 37].

2.2   Polarization

A fundamental property of light is polarization. In this subsection, the main concepts of polarization of x-rays are introduced, including the formalism of the Stokes parameters. Additionally, polarized Compton scattering is discussed.

2.2.1   Polarization of photons

The electromagnetic wave is defined by an electric and a magnetic field, which oscillate perpendicular to each other and transverse to the propagation direction of the wave. For a characterization of the photons often either the description of the electric or of the magnetic field is sufficient. By convention the electric field is used [38]. The behavior of the oscillation of the electric field vector defines the polarization of the photon. In general, the projection of this vector perpendicular to the direction of motion of the photon forms an ellipse, the so called polarization ellipse as shown in figure 2.4. This polarization type is referred to as elliptical polarization [39].

Nonetheless, there are two important special cases, which are displayed in figure 2.5. If the orientation of the electric field oscillation is constant over time, the photon is
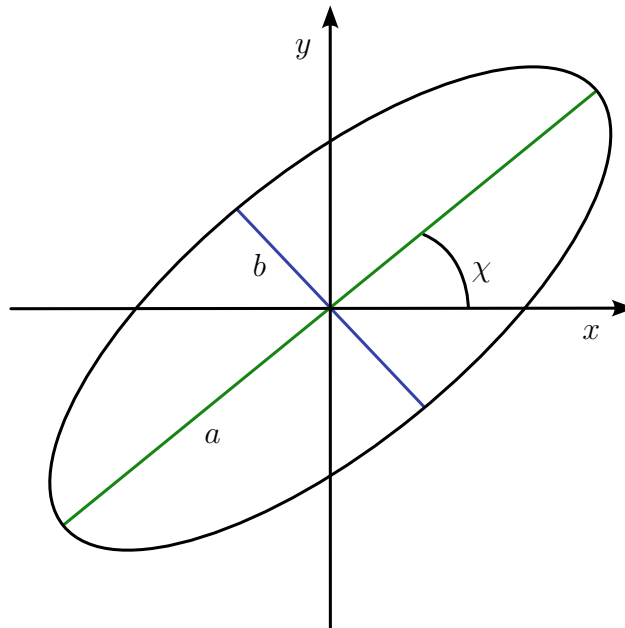
Figure 2.4: Schematic illustration of the polarization ellipse. The orientation is given by χ and the semi-major- and the semi-minor-axis are denoted by a and b, respectively. The electromagnetic wave propagates along the z-axis. Adapted from [40].

linearly polarized. To put it differently, one of the semi-axis vanishes and the projection of the electric field results in a straight line, see figure 2.5 (a). In the second case, the semi-major- and the semi-minor-axis (which correspond to a and b in figure 2.4) are equal and the projection forms a circle. The electric field is not constant over time and instead rotates. In contrast to elliptical polarization, the amplitude in this case remains constant over time. This is called circular polarization, see figure 2.5 (b). A distinction can be made between right-handed (R) and left-handed (L) circularly polarized photons [41].

Another suitable way to describe the polarization is the use of the Stokes parameters [42]. Especially for the transfer of the formalism from a single photon to a photon beam. If the electric field vectors of all photons are directed in the same direction, the beam is completely polarized. The beam is partially polarized when only a certain proportion of the photons oscillate in the same direction. The Stokes parameters are not restricted to the case of no, partial or complete polarization [38]. Therefore, they are well suited for the analysis in this thesis.
The relation between the polarization and the intensity of the photon beam can be used to calculate the Stokes parameters [39]. For a photon beam, the total Stokes
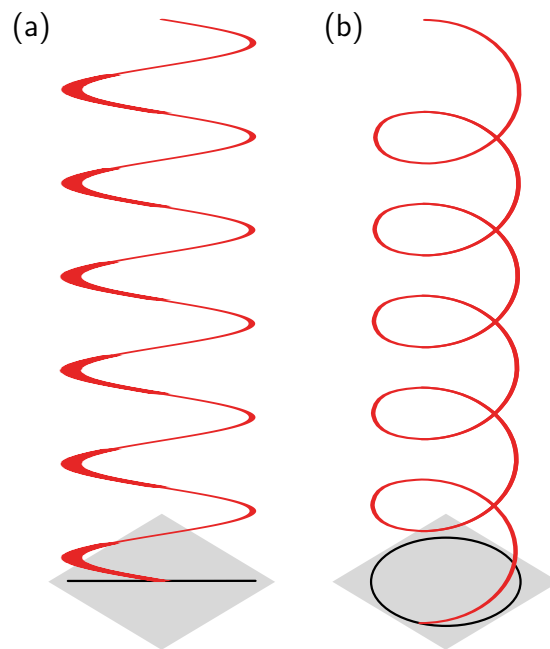
Figure 2.5: Schematic representation of polarization states of a single photon. In red is the trajectory of the electric field vector of (a) a linearly polarized and (b) a circularly polarized photon shown. The trajectory in the plane perpendicular to the propagation direction (gray) is displayed in black. Adapted from [39].

parameters are defined as [39]

$$
\begin{aligned}
S_0 &:= I_{0°} + I_{90°}, \\
S_1 &:= I_{0°} - I_{90°}, \\
S_2 &:= I_{45°} - I_{135°}, \\
S_3 &:= I_R - I_L.
\end{aligned}
\tag{2.8}
$$

S_0 denotes the total intensity. The circular polarization is given by S_3 with the intensity difference between right- and left-handed circular polarized photons. Distinctions in the intensity between orthogonal polarization states are expressed by the Stokes parameters S_1 and S_2, which represent linear polarization. Thereby the intensity I_χ corresponds to the beam transmitted through a polarization filter which is tilted by the angle χ to the orientation of the electric field vector. Beyond the optical regime, conventional polarization filtering techniques are not applicable anymore. Thus, indirect polarimetry measurements are necessary as for example Compton polarimetry, see subsection 2.3.

Alternately, instead of the total Stokes parameters S_n, the normalized Stokes parameters P_n can be used [41], which are defined as

$$
P_n = \frac{S_n}{S_0}, \qquad n = 0, 1, 2, 3.
\tag{2.9}
$$

Nevertheless, both sets are called Stokes parameters and can be written in vectorial form as

$$\boldsymbol{S} = \begin{pmatrix} S_0 \\ S_1 \\ S_2 \\ S_3 \end{pmatrix}, \qquad \boldsymbol{P} = \begin{pmatrix} 1 \\ P_1 \\ P_2 \\ P_3 \end{pmatrix}. \tag{2.10}$$

This matrix representation enables some special cases to be easily identified. An unpolarized photon beam is expressed as $P_1 = P_2 = P_3 = 0$. For a fully linearly polarized beam in the direction tilted by the angle χ along the direction of movement, follows $P_1 = \cos(2\chi), P_2 = \sin(2\chi), P_3 = 0$. A completely circular polarized beam is given by $P_1 =, P_2 = 0, P_3 = \pm 1$, with "$+$" for right-handed and "$-$" for left-handed [43].

As discussed earlier, a photon beam can be in a state between unpolarized and completely polarized. To quantify the polarization, one can use the degree of polarization, defined as [41]

$$P = \sqrt{P_1^2 + P_2^2 + P_3^2} \leq 1. \tag{2.11}$$

Equation (2.11) can be specified for beams without circularly polarized photons, so that $P_3 = 0$. This results in the degree of linear polarization

$$P_L = \sqrt{P_1^2 + P_2^2}. \tag{2.12}$$

From this, the Stokes parameter P_1 and P_2 can be calculated as

$$P_1 = P_L \cdot \cos(2\chi), \qquad P_2 = P_L \cdot \sin(2\chi). \tag{2.13}$$

The orientation χ of the polarization ellipse, see figure 2.4, follows from equation (2.13) as

$$\chi = \frac{1}{2} \cdot \arctan\left(\frac{P_2}{P_1}\right). \tag{2.14}$$

2.2.2   Transfer matrix formalism

As above mentioned, the Stokes parameters are well suited to characterize the scattering of photon beams. Therefore, let the total Stokes vector of the incident photon be $\boldsymbol{S}$. Of the scattered photon, the Stokes vector is denoted as $\boldsymbol{S'}$. As the definitions given in equations (2.8) show, the Stokes parameters depend on the orientation χ of the polarization and thus on the coordinate system. Due to this fact, a coordinate system for both the incident and the scattered photon is required. Before scattering the coordinate system is given by the x-, y- and z-axis and after by x'-, y'- and z'-axis, they are illustrated in figure 2.6. The coordinate system of the initial photon is chosen as the laboratory system. Here, the z- and z'-axis, which correspond to the direction of motion of the initial photons are equal.

As can be seen in figure 2.6, the scattering plane can be tilted to the reference plane by the angle φ along the z-axis. This rotation can be linearly transformed to the
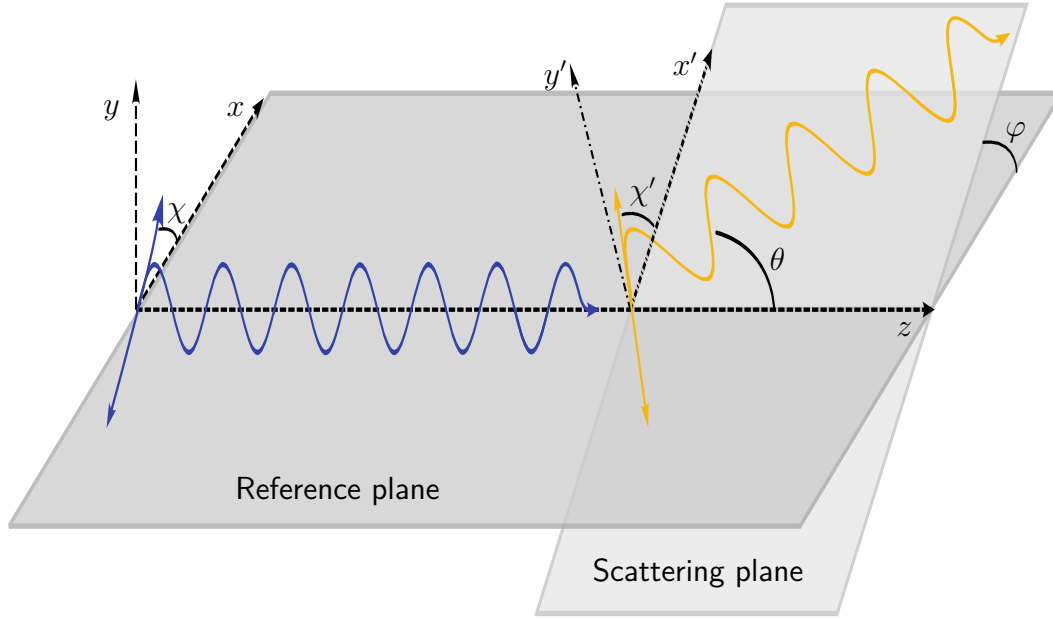
Figure 2.6: Schematic representation of a scattering process of linearly polarized photons. θ is the polar and φ the azimuthal angle which characterize the propagation direction of the scattered photon. The orientation of the linear polarization is given by χ and χ' for the incident (blue) and the scattered (yellow) photon, respectively. Adapted from [27].

laboratory system with the rotation matrix [44]

$$\hat{M}(\varphi) = \begin{pmatrix} 1 & 0 & 0 & 0 \\ 0 & \cos(2\varphi) & \sin(2\varphi) & 0 \\ 0 & -\sin(2\varphi) & \cos(2\varphi) & 0 \\ 0 & 0 & 0 & 1 \end{pmatrix}. \tag{2.15}$$

The scattering process is described in form of the differential cross section in the transfer matrix $\hat{T}$. This matrix depends on the incident photon, the scattering target, and the polar angle θ, but not on the second scattering angle, the azimuthal angle φ [44].
For the relation between $\boldsymbol{S}$ and $\boldsymbol{S}'$ follows

$$\boldsymbol{S}' = \hat{T}(\theta) \cdot \hat{M}(\varphi) \cdot \boldsymbol{S}, \tag{2.16}$$

by combining the coordination transformation under $\hat{M}(\varphi)$ and the physical description of the scattering process with $\hat{T}(\theta)$. From equation (2.16), the differential cross section of the scattering process results in [43]

$$\frac{\mathrm{d}\sigma}{\mathrm{d}\Omega}(\theta, \varphi) = \frac{S_0'}{S_0} = (1, 0, 0, 0) \cdot \hat{T}(\theta) \cdot \hat{M}(\varphi) \cdot \boldsymbol{P}. \tag{2.17}$$

2.2.3 Compton scattering with polarized photons

The physical characterization of the Compton scattering in equation (2.16) is given by $\hat{T}$. This matrix formalism is discussed in detail in [44]. In this thesis, the coordinate systems are chosen somewhat differently than in the paper, so that not all entries are the same. An equivalent choice of the coordinate systems can be found in [45]. For the coordinate systems used in this thesis, the according transfer matrix reads

$$\hat{T} = \frac{r_e^2}{2} \cdot \left(\frac{k'}{k}\right)^2$$
$$\times \begin{pmatrix} 1 + \cos^2(\theta) + (k - k')\,(1 - \cos(\theta)) & -\sin^2(\theta) & 0 & T_{03} \\ -\sin^2(\theta) & 1 + \cos^2(\theta) & 0 & T_{13} \\ 0 & 0 & 2\cos(\theta) & T_{23} \\ T_{30} & T_{31} & T_{32} & T_{33} \end{pmatrix} . \quad (2.18)$$

This is the matrix representation of the Klein-Nishina formula. It is based on the assumption that the photon scatters from a free electron. Additionally, only the simplified case of Compton scattering, in which the spin of the final electron is not observed, is considered in equation (2.18). To improve readability, the last row and column in the matrix are not explicitly given. The terms of the last column correspond to the incident photon and those of the last row to the scattered photon and their circular polarization component. Besides T_{33}, all vanish on average for non-spin-polarized targets, due to the fact that they are proportional to the electron spin. In this thesis this is especially the case. The detector used, a polarimeter, is not sensitive to circular polarization. Furthermore, it can be assumed that circular polarization is negligible in the experiment discussed in this thesis. This allows neglecting the complete last row, including T_{33}. From this an effective 3×3 matrix results. Only this upper submatrix is used for calculation. Accordingly, the Stokes vectors $\boldsymbol{P}$ and $\boldsymbol{S}$ are then dealt with as three-component vectors.

2.3 Compton polarimetry

To analyze the scattering process, it is of interest to determine the "polarization transfer" of the scattered photon, when the polarization of the incident photon is known. The polarization can reveal the anisotropic behavior of Compton scattering.

In the low energy x-ray regime between $\approx 1\,\text{keV}$ and few tens of keV, different types of polarimeters have been developed. They are based, for example, on Bragg reflection, photoabsorption and Thomson scattering [46–48]. Above several hundreds of MeV, electron-positron pair production is used to measure polarization [49]. In the intermediate energy range from $\approx 50\,\text{keV}$ to several MeV, Compton scattering is usually employed, due to the sensitivity of the atimuthal scattering distribution of the Compton process.

A demonstration of this sensitivity is visualized with a scattering distribution in figure 2.7. Here, the dependency of the differential cross section on the azimuthal angle is shown. The orientation of the φ-distribution is given by the direction of the electric field vector $\vec{E}$ of the incident photons.
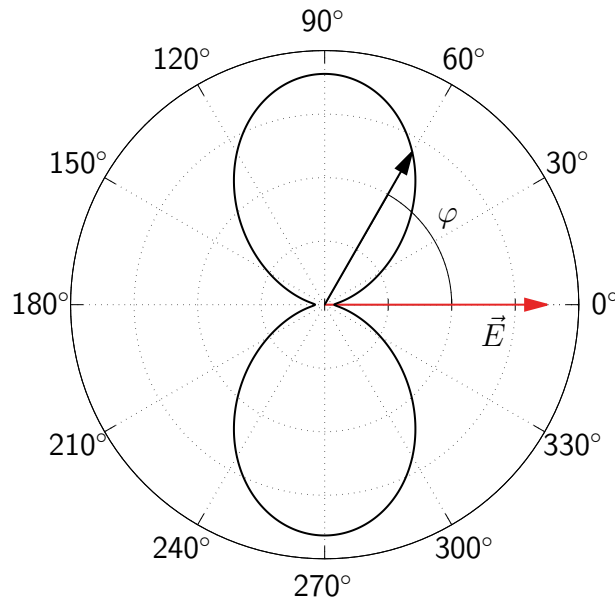
Figure 2.7: Differential cross section for Compton scattering of x-rays. Example φ-distribution of initially linearly polarized photons with the orientation of the polarization given by the electric field vector $\vec{E}$ (red).

Since the 1950s, Compton scattering polarimetry has been discussed [50]. Most of these detectors are only able to analyze linear polarization, as well as the detector used in this thesis. Nonetheless, it is possible to investigate circular polarization through scattering by spin-aligned electrons from a ferromagnetic scatterer [51].

Existing Compton polarimeters differ in various detector combinations, technical constructions, energy resolutions, sensitivities, efficiencies, and detector materials [53]. Figure 2.8 illustrate a basic method consisting of at least two x-ray detectors, one acting as a scatterer and the other(s) as an absorber. This is similar to the setup first discussed, used in [50]. In the first detector, photons Compton scatter from electrons and then exit the crystal. The latter detectors are positioned to detect these scattered photons at a specific azimuthal angle φ and a given polar angle θ. This setup is used to measure the intensity distribution of Compton scattering for various azimuthal scattering angles. As shown by equations (2.7), (2.17) and (2.18), this distribution strongly depends on the polarization. In particular, perpendicular to the polarization direction of the incident beam, the differential cross section reaches its maximum, such as illustrated in figure 2.7. Thus, the intensity distribution of the scattered photons reveals the polarization of the incident beam. At least two detection positions are necessary to obtain P_1 ($\varphi = 90°$ and $\varphi = 0°$) and P_2 ($\varphi = 135°$ and $\varphi = 45°$). Therefore, the degree of linear polarization can be determined by measuring the angular distribution of the scattered photon intensities.

The polarization of a single photon cannot be measured with a Compton polarimeter, because the reconstruction of the probability distribution results in the observed emission pattern. As a result, only the information about the average polarization state of
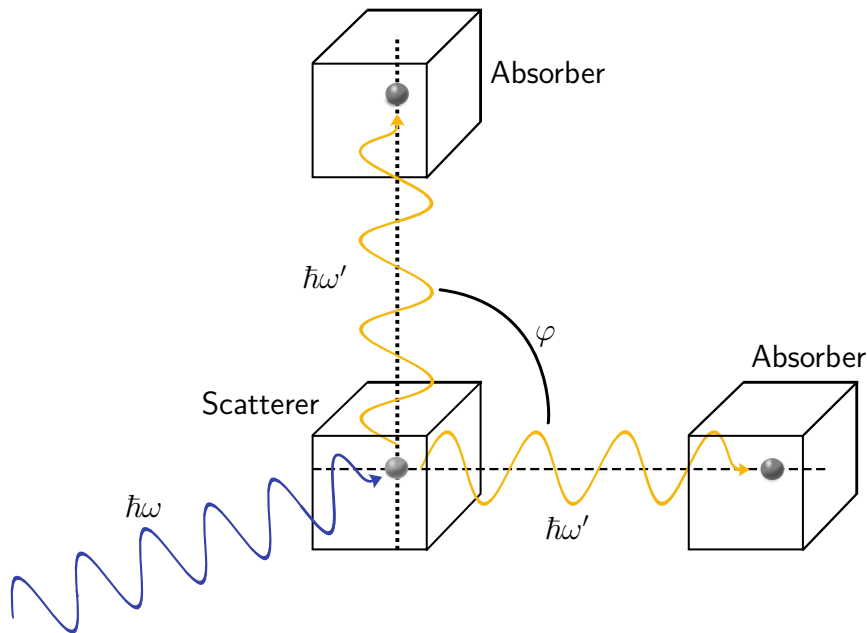
Figure 2.8: Schematic representation of a basic polarimeter setup. The incident
photon scatters in the first detector, the scatterer, and is then absorbed
in the second detector, the absorber. The latter detector can be moved
with the azimuthal angle φ at a fixed polar angle. Adapted from [52].

a large number of photons can be extracted. This is in contrast to polarization filters
in the optical regime, where the polarization of a single photon can be identified [54].
The difference in intensity between orthogonal and parallel scattered photons of an
initially completely linearly polarized photon beam defines the modulation [53]

$$M(\varphi) = \frac{I_{\varphi+90°} - I_\varphi}{I_{\varphi+90°} + I_\varphi}. \tag{2.19}$$

I_φ corresponds to the intensity of the photons scattered at the azimuthal angle φ
relative to the orientation of the electric field vector. M is proportional to the polar-
ization and minimized when φ is perpendicular to the direction of the polarization,
and maximized parallel to it. Note that the azimuthal asymmetry of the Klein-Nishina
distribution, equation (2.7), depends also on the polar scattering angle θ. Thus, the
scattering angle should be chosen so that the modulation is maximal. For the energy
of about 175 keV used in this thesis, this would be the case for a polar scattering
angle of $\theta \approx 90°$ [55].
The dependence of the differential cross section on the polar scattering angle θ is
shown in figure 2.9. In (a) the differential cross section is displayed for three energies
at a fixed azimuthal angle of $\varphi = 0°$. As can be seen, the minima for all energies
are at $\theta \approx 90°$ and the angular scattering distribution maximizes at forward angles.
This is also the case for different azimuthal angles, which are illustrated in (b) at an
energy of 175 keV. The minimum of the differential cross section is less pronounced
at higher azimuthal angles and is almost absent at $\varphi = 45°$.
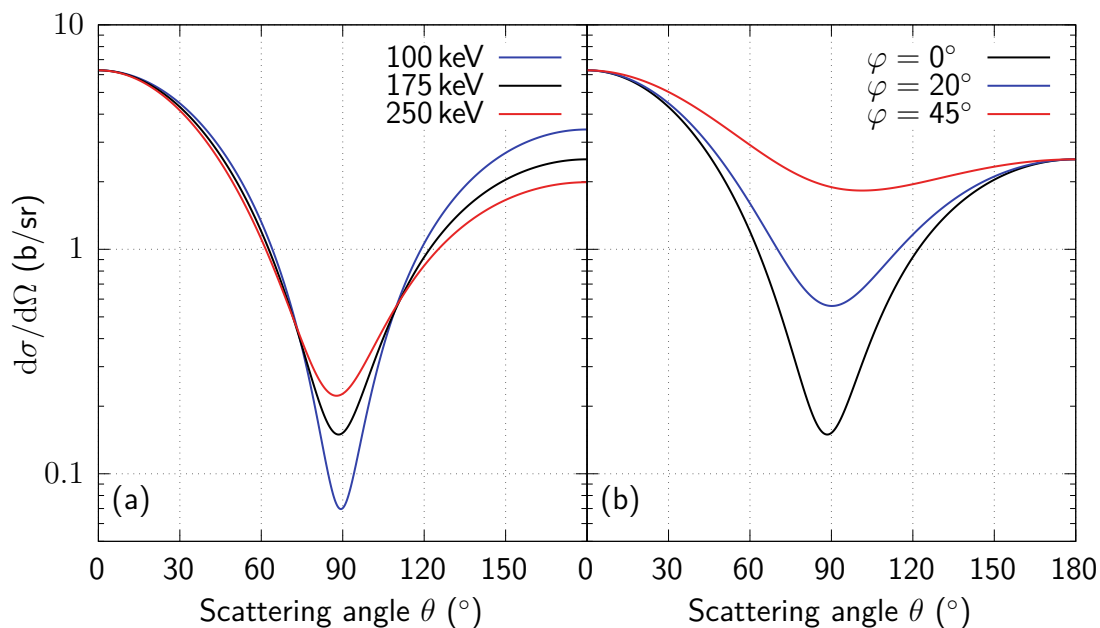
Figure 2.9: Differential cross sections of Compton scattering of completely linearly polarized photons on gold. In (a) calculated for three different energies at $\varphi = 0°$ and in (b) for three azimuthal angles at 175 keV.

To obtain a φ-distribution as shown in figure 2.7, in the discussed setup, the absorber detector needs to be positioned at several azimuthal angles. Besides this, there are some other disadvantages of this setup. The scatterer needs to be particularly small so that the probability of the photon leaving the detector after Compton scattering is high. If the two detectors are too close, the uncertainty of the angular position increases and become more significant. Additionally, the efficiency is particularly low, because the photons scatter in all azimuthal angles and the detector covers only a small fraction. Due to this, the setup requires a lot of space at experiments and a lot of time to accumulate data for the several detector positions [52].

Some of the disadvantages can be eliminated or decreased by using a different setup. By combining the scatterer and absorber, a higher efficiency can be achieved. This means that the photon scatters and gets absorbed in the same detector. In order not to lose the angular resolution it is necessary that the detector consists of individual pixels. Each pixel can be used as the scatterer as well as the absorber. Figure 2.10 demonstrates such a detector setup, which enables to detect the entire φ-distribution at a certain spatial position. The much smaller distance between the pixels is not leading to a large angular uncertainty compared to the basic setup, since the size of these is much smaller.

Furthermore, for initial photon energies less than half the electron rest energy, a clear distinction between the energy of the photon and that of the electron is possible, see equation (2.5). The distribution of the initial photon energy between the scattered photon and the recoil electron depending on the scattering angle is displayed in 2.11.
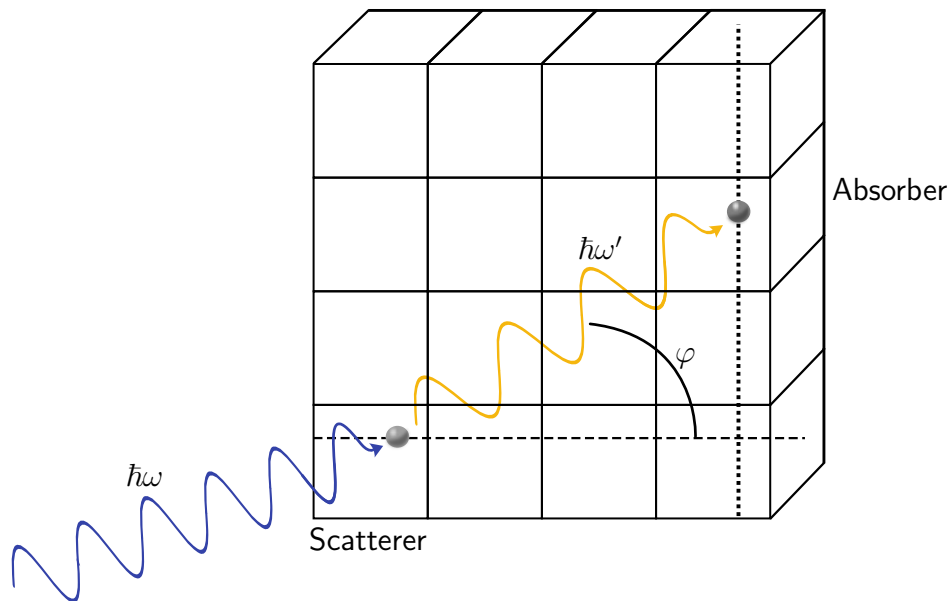
Figure 2.10: Schematic representation of a pixel detector polarimeter. The azimuthal angle φ can be obtained from the position of the two involved pixels. Every pixel can act as a scatterer and absorber. Adapted from [54].

The disadvantage of this structure is the large set of readout electronics. Since each pixel acts as a detector, a separate readout chain is required. This is especially true for thick crystals and high segmentation. Another and unconventional approach to reduce the amount of electronics is to replace the pixel structure with two layers of strips that are orthogonal to each other. A schematic representation is illustrated in figure 2.12. From this, the number of readout electronics is given by the sum of the vertical and horizontal strips instead of the product in the case of a pixel detector. The two layers of strips are positioned at the front and back side of the crystal. At the measurement of a signal, one strip from the front and one from the back will detect this signal. With the help of these two strips, the vertical and horizontal positions can be determined. Combined, they result in a quasi-pixel at the position of detection. As can be seen in figure 2.12, two simultaneously measured signals can be distinguished, if they have different energies. This enables the detection of the Compton scattered photon and electron, providing the basis of a Compton polarimeter.
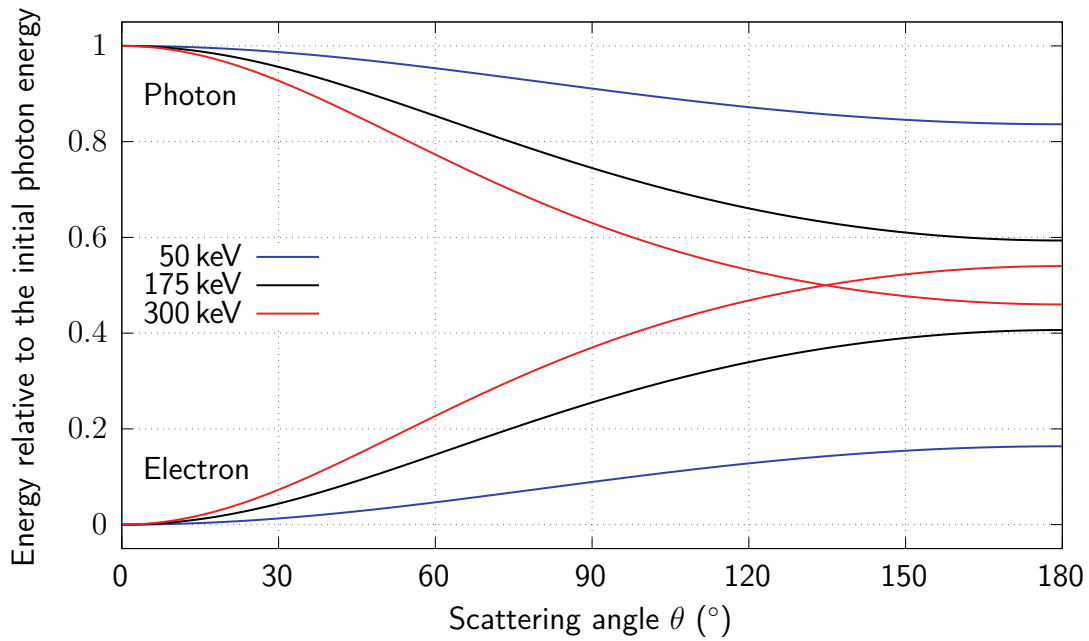
Figure 2.11: Kinematic energy of the scattered photon and the recoil electron relative to the initial photon energy for Compton scattering. Dependency of the energy splitting on the scattering angle θ for three different initial energies.
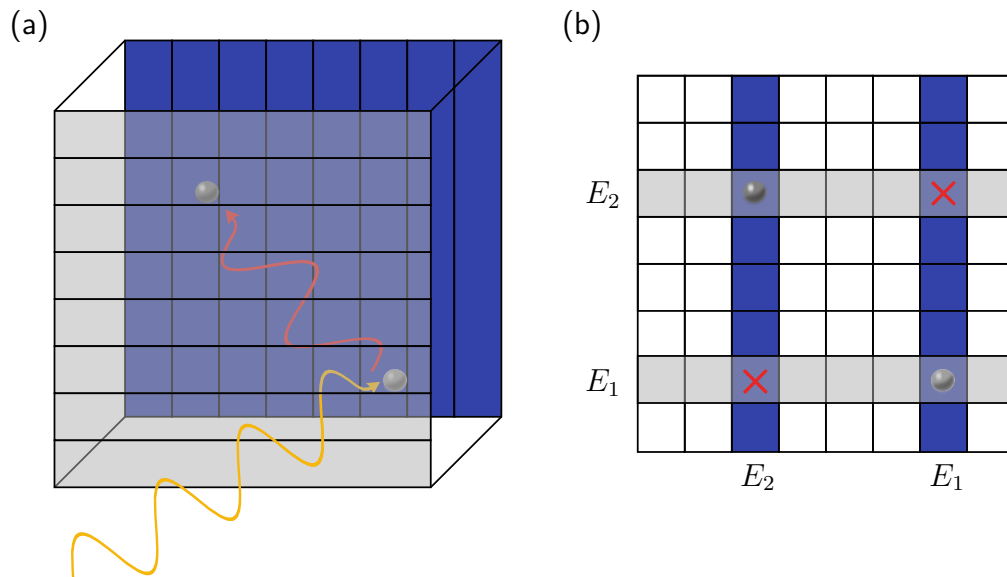
Figure 2.12: Schematic representation of a segmented polarimeter and the position determination of two measured signals. The detection of a Compton event between two strip layers with orthogonal orientation to each other is shown in (a). In (b) the energy condition results in the determination of the quasi-pixel positions. Adapted from [56].

3 Experiment

The experiment is discussed in detail in this section. Thereby, a gold target was positioned in a synchrotron beam to investigate the resulting scattering processes. In subsection 3.1, the x-ray source is described. The detectors used are explained in subsection 3.2 and the setup of the experiment in subsection 3.3. An overview of the individual measurements is given in subsection 3.4.

3.1 Synchrotron radiation source

Charged particles can be accelerated through an electric field. A linear accelerator is conceptually the simplest type of accelerator to realize. In this design, the particles can be accelerated only once when they pass the accelerator section. Another approach is to bend the trajectory of the charged particles into a circle. This can be done with magnets. The particles are accelerated in some of the straight sections. If the trajectory is closed and circular, such an accelerator is called a synchrotron [57]. In contrast to a linear accelerator, the particles can be accelerated many times. Therefore, only a few accelerator sections are needed. The particles lose energy during their passage through the magnets by emitting photons. This effect can be exploited as a light source, which is then referred to as a synchrotron radiation source. Here, the synchrotron acts as a storage ring. The charged particles orbit at a mean constant velocity. In the accelerator sections, the energy losses get compensated [57].

Originally, particle accelerators were exploited as the first generation of synchrotron radiation sources. Storage rings specifically designed as a radiation source are referred to as second generation. Technically more developed sources can be considered as the third generation of synchrotrons.

A periodically alternating magnetic field pattern, displayed in figure 3.1, serves as a dedicated photon source. Due to the magnetic field, the charged particles oscillate on a sinusoidal trajectory, resulting in the emission of radiation. By the undulator period λ_u, see figure 3.1, the period of the magnetic structure is given. The relation between the synchrotron radiation wavelength λ and undulator period is given by the undulator equation [58]

$$\lambda(\theta) = \frac{\lambda_u}{2\gamma^2} \left(1 + \frac{K^2}{2} + \gamma^2\theta^2\right). \tag{3.1}$$

The wavelength of the synchrotron radiation depends on the Lorentz factor γ, the emission angle θ with respect to the direction of the particle beam and the dimensionless undulator parameter K. It is defined as [58]

$$K = \frac{eB\lambda_u}{2\pi m_e c}, \tag{3.2}$$

where e is the elementary charge, m_e the electron mass, c the speed of light and B the magnetic field. The undulator parameter characterizes the strength of the deflection of the particles. To adjust this parameter, the magnetic field can be changed. In the case of permanent magnets, this is done through changing the distance between

the magnets. The generated radiation is emitted forward in a cone with a maximum opening angle of

$$\theta_{\max} \approx \frac{K}{\gamma} \tag{3.3}$$

for a reduced velocity of $\beta \approx 1$ [58]. For $K \gg 1$ the cone is large and the emission spectrum is quasi-continuous. The setup is referred to as a wiggler [58], see figure 3.1 (a). In the case of $K \leq 1$, the cone is particularly narrow. Due to this fact, photons in most sections of the cone overlap and interfere with each other. This results in an almost monochromatic spectrum [58], which is an important characteristic of a so called undulator, see figure 3.1 (b).
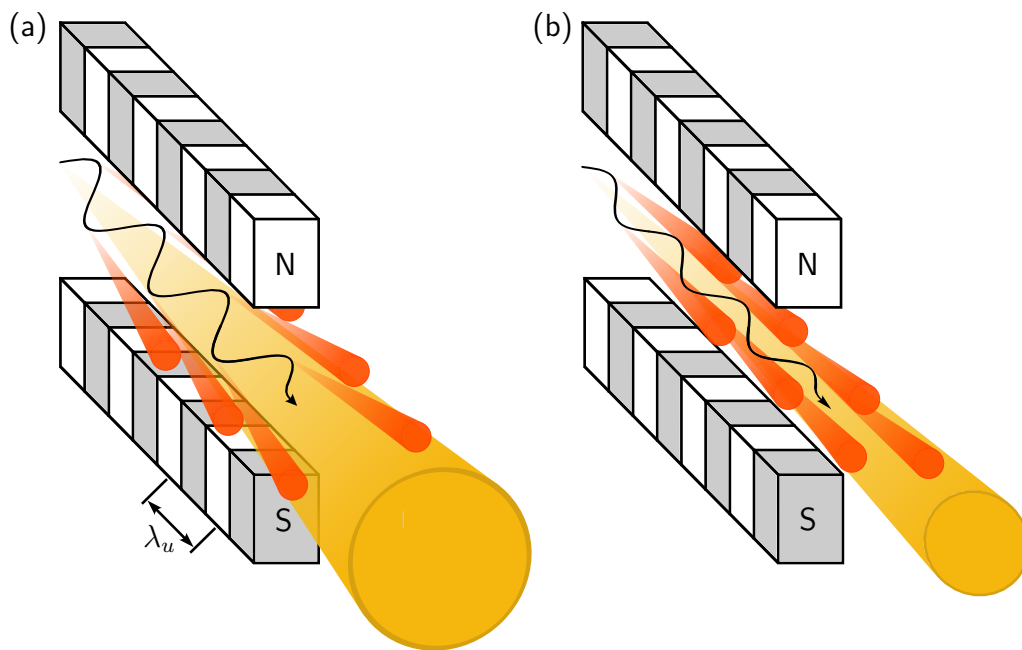
Figure 3.1: Schematic representation of (a) a wiggler and (b) an undulator. The magnetic poles are indicated in white (north) and gray (south). The trajectory of the charged particles is shown in black. The emitted photons are represented as the red cones and the total beam as the yellow cone. Adapted from [59, 60].

The experiment presented in this thesis was performed at the third generation synchrotron radiation source PETRA III [61], which is located at the large-scale research facility DESY, a research center of the Helmholtz Association in Hamburg, Germany [62]. At DESY the scientific focus is mainly on particle physic, accelerators, and photon science [62]. The latter two are related to the here discussed experiment.

The properties and parameters of PETRA III given in the following paragraph are taken from the DESY website [61]. PETRA III is a particle storage ring, designed to accelerate electrons for the production of x-rays. It operates at an electron energy of 6 GeV. The circumference of the storage ring is 2304 m. Three experimental halls, "Max von Laue", "Paul P. Ewald" and "Ada Yonath", offer at 26 beamlines the opportunity for several experiments at the same time. With a length of 300 m is the "Max

von Laue" hall the largest, including 15 beamlines and more than 30 experimental stations, which are open for user proposals. Further explanations and parameters can be found in [63].
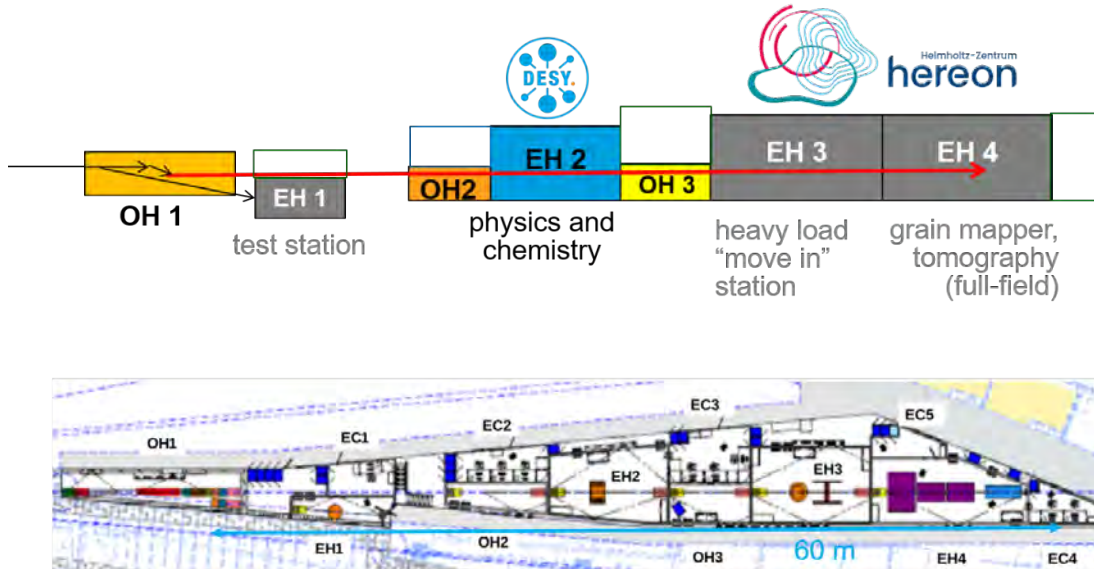
Figure 3.2: Schematic representation of the beamline P07. The abbreviations are OH (Optics Hutch), EH (Experimental Hutch) and EC (Experimental Control cabin). Graphic from [64].

The experiment described in this thesis was performed at the High Energy Materials Science Beamline P07 [65] in the "Max von Laue" hall at PETRA III. From the datasheet on the DESY website [66], the subsequent information is extracted. This beamline was operated by the Helmholtz Center Geesthacht and DESY. It provides a tuneable energy from 30 keV to 200 keV of linearly polarized photons. The source of the x-rays is an undulator with $\lambda_u = 21.2$ mm and 188 periods.

A schematic representation of the P07, including the different experimental hutches, is presented in figure 3.2. In OH1 a double crystal monochromator enables to tune the photon energy and in OH2 the focusing optics are positioned [67]. After the monochromator, a beamline spectral resolution of 5 eV to 250 eV at an energy of 80 keV can be expected [66]. The experiment was performed in EH3 with a beam energy of 175 keV and a diameter of 1 mm^2.

3.2   Semiconductor detectors

Two different semiconductor detectors were used to measure the photons in the discussed experiment. The basic principal of a semiconductor detector can be considered as an ionization chamber in a solid. When a photon hits the crystal, it creates a cloud of positively and negatively charged charge carriers. In the conduction band of the semiconductor, these charge carriers can propagate freely to the corresponding contacts. The advantage of semiconductor detectors is a high efficiency due to a large

density of free electrons. In addition, semiconductor detectors provide a high resolution, as the charge carriers can propagate with a particularly low loss rate inside the crystal, which are then detected at the contacts. In subsections 3.2.1 and 3.2.2 the detectors are presented in detail. The following is a general explanation of semiconductor detectors.

A crystal with electric contacts on both sides acts as the detection part of the detector. The most commonly used crystal materials are silicon and germanium. These two elements have four valence electrons. The conduction property of the crystal can be modified by introducing impurities in a controlled manner. Then the crystal is doped. This is done on both sides of the detector crystal. On one side with atoms that have fewer valence electrons than the crystal material. In the case of silicon and germanium, these are atoms with three valence electrons. They are called acceptors or p-dopants. On the other side atoms with more valence electrons. For silicon and germanium, atoms with five valence electrons are chosen. These atoms are referred to as donors or n-dopants [68]. An acceptor leads to a defect, also called a hole, in the structure, because it has one valence electron less than the crystal material. This hole can be seen as a positive charge carrier. In contrast to this, a donor has one valence electron more, which can move almost freely inside the crystal. The spatially different concentration of the n- and p-dopants leads to a charge distribution. This is increased by the recombining of the donor electron and the acceptor holes in the border region of these two parts. In this so called depletion zone, no free charge carriers are left [19]. The initially neutral regions are charged, after recombination of electrons and holes. Extra holes in the n-region cause a positive charge and the additional electrons in the p-region cause a negative charge, respectively. By this, an electric field is generated with a gradient between the n- and p-region [19]. Nevertheless, the complete crystal is still electrically neutral, due to the fact that the doped atoms are neutral [68]. The depletion region can be increased by applying an external reversed bias voltage. Here the positive pole is at the n-region and the negative at the p-region. Through this voltage, the free charge carriers drift to their related poles. By the depletion zone, the active area of the detector is defined [68]. Typically applied external voltages to maximize the depletion zone are in the order of kV.

The energy of a photon E is absorbed in the depletion area, resulting in local electron-hole pairs. This cloud has a total negative charge Δq, which is proportional to E. These free charge carriers drift to their opposite poles of the detector. By this movement, a change of the voltage ΔU is induced

$$\Delta U = \frac{\Delta q}{C},\tag{3.4}$$

where C is the capacity of the detector, which depends on the geometry [19]. For semiconductor detectors a planar geometry is common. Here, the contacts are positioned parallel to each other on the crystal. The capacity of a planar detector is

$$C = \epsilon_r \cdot \epsilon_0 \cdot \frac{A}{d},\tag{3.5}$$

where d is the width, A the area of the depletion area, ϵ_r the dielectric constant and ϵ_0 the vacuum permittivity [19]. To achieve a good signal-to-noise ratio, ΔU should

be maximized and thus C should be minimized. A larger capacity can be realized by a maximization of d, which is technically limited and can be realized though a different geometry. For larger thicknesses, a coaxial crystal can be realized. It has a cylindrical shape where one contact is on the outer surface and the other on the inner surface of the cylinder. In addition, A needs to be chosen so that the capacity is minimized and the efficiency is not too low due to the reduced active area.

Thermal excitation can lead to spontaneous creation of electron-hole pairs, leading to a decrease in energy resolution and an increased noise. This effect is not negligible at room temperature but can be diminished by cooling down the detector crystal [68]. Liquid nitrogen is a commonly used choice for cooling. Besides the crystal, the connected electronic readout system can be a source of noise. Here the preamplifier, which is directly connected to the crystal, is most critical. Additional cooling of these components can improve the resolution [43].

3.2.1   Ge-detector

For the experiment described in this thesis, a commercial high purity germanium (HPGe) detector from ORTEC was used to gain high energy resolution spectra. The model number is GEM-SP5020P4-B. A coaxial crystal geometry is used in this detector. The crystal has an active diameter of 49.7 mm and a depth of 21.1 mm. For the coaxial shape, a hole with a diameter of 5.2 mm and a depth of 3 mm is positioned in the center of the backside. As previously discussed, to improve the energy resolution, the crystal and the preamplifier are cooled down. The liquid nitrogen for cooling was provided by a connected dewar. Due to the cooling, the detector crystal and the preamplifiers need to be in a vacuum. This is shielded by a 0.5 mm thick beryllium window from the ambient air. An energy resolution of 293 eV at 5.9 keV and 526 eV at 122 keV can be achieved with the detector. This resolution is defined by the Full Width at Half Maximum (FWHM). The parameters given in this paragraph are taken from [69].

3.2.2   Si(Li) detector

A segmented semiconductor detector was used for the polarization measurement. In figure 3.3 (a) is a picture of the detector illustrated. The detector crystal is made of lithium-driven silicon (Si(Li)). It was developed and manufactured at the Forschungszentrum Jülich and the Semicon Detector GmbH within SPARC (Stored Particle Atomic Research Collaboration) [70].

The raw material of the crystal is p-doped silicon. Boron is implanted on one side of the crystal, resulting in a few μm thick p^+-contact layer. On the opposite side, lithium is diffused into the crystal, acting as a donor. Therefore, it compensates the holes of the p-type doping. As in the case of the implanted boron, the lithium creates a few μm thick n-doped layer. Correspondingly, the structure of a p-i-n diode is obtained. The silicon serves as the intrinsic layer of the diode. In order to achieve the segmented structure, photolithography was used on both sides. Each of the surfaces is segmented into 32 strips. The strips from both sides are orthogonal to
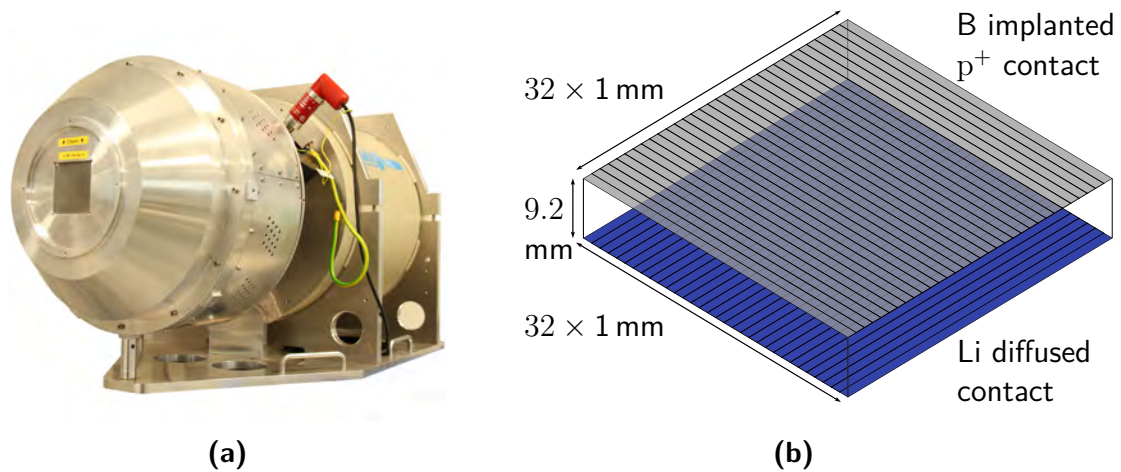
Figure 3.3: (a) Photograph of the Si(Li) detector [71]. (b) Schematic representation of the strip geometry. Adapted from [72].

each other, which results in a quasi-pixel structure. With a strip width of 1 mm, the active area is 32 mm × 32 mm. Two neighboring strips are electrically isolated by a gap (groove). This structure yield a grid with 1024 quasi-pixels with a size of 1 mm^2 each. A schematic representation of the strip structure is shown in figure 3.3 (b). The segmented structure is positioned in the center of the crystal, which has a total width and height of 46 mm.

Each strip is individually connected to the electronics and can therefore be read out independently. A detailed overview of the readout electronics follows in subsection 3.3.2. Especially, the preamplifiers are connected directly to the strips. They are in the vacuum together with the crystal. Via a thermal connection with the liquid nitrogen dewar, they are cooled collectively. A 0.3 mm thin beryllium window separates the vacuum from the environment. Including the dewar, the complete detector has a size of 76 cm × 43 cm × 44 cm. All parameters and data from the last two paragraphs can be found in [73].

For an individual strip, an energy resolution of 0.8 keV to 1.2 keV FWHM at a photon energy of 60 keV is achievable [72]. Furthermore, a time resolution of ≈ 50 ns can be reached. This enables via coincidence conditions the suppression of the background [72]. Further details can be found in [40, 56, 72].

3.3   Experimental setup

For the description of the experiment, especially the geometry and the data acquisition are of great importance. Subsection 3.3.1 shows the geometry and explains the individual components as well as their arrangement. The data acquisition of the two detectors is described in subsection 3.3.2.

3.3.1 Geometry of the experiment

In this subsection, the geometry of the experiment is discussed. The experiment was conducted in EH3 of beamline P07 of the PETRA III synchrotron ring. The preparation of the beam until the experimental hutch is described in subsection 3.1. A schematic representation of the experiment is illustrated in figure 3.5.
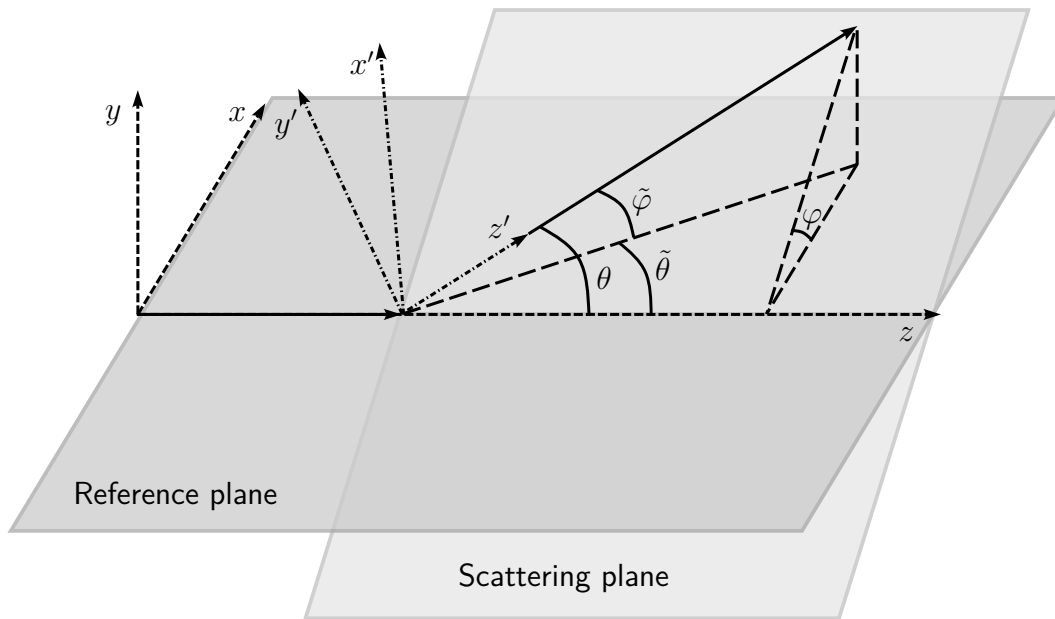
Figure 3.4: Schematic representation of the definitions of the scattering angles. The solid lines correspond to the propagation direction of a photon. θ and φ are utilized for the analysis and $\tilde{\theta}$ and $\tilde{\varphi}$ were used for the construction of the target chamber.

Before the description of the complete setup, the different angles by which the detector positions can be described, are discussed. The scattering angles defined in figure 2.6 are utilized for the analysis in section 4. A different set of angles was used for the design of the target camber. These angles are denoted by the tilde symbol below. For clarity, the definitions of the scattering angles are shown in figure 3.4. θ and φ correspond to the polar and azimuthal angles in spherical coordinates. Whereas $\tilde{\theta}$ and $\tilde{\varphi}$ are characterized by the projection of the scattered photon onto the reference plane.

In subsection 4.2, the determination of θ is described. For the experiment, a target chamber was designed with viewports for various detection points. These positions were set in the design by $\tilde{\theta}$ and $\tilde{\varphi}$. For all positions $\tilde{\theta}$ was measured at the target chamber after the construction. This was also done for $\tilde{\varphi}$ for the detection positions outside the reference plane. Other than that, $\tilde{\varphi}$ is zero. The relation between the different scattering angles is determined as

$$\cos(\tilde{\theta}) = \frac{\cos(\theta)}{\cos(\tilde{\varphi})} \tag{3.6}$$

and

$$\cos(\varphi) = \frac{\sin(\tilde{\theta}) \cdot \cos(\tilde{\varphi})}{\sqrt{(\sin(\tilde{\varphi}))^2 + (\sin(\tilde{\theta}) \cdot \cos(\tilde{\varphi}))^2}}. \tag{3.7}$$

If the denominator is zero in equation (3.6), then the scattering is along the y-axis. For equation (3.7), the scattering occurs in the reference plane.
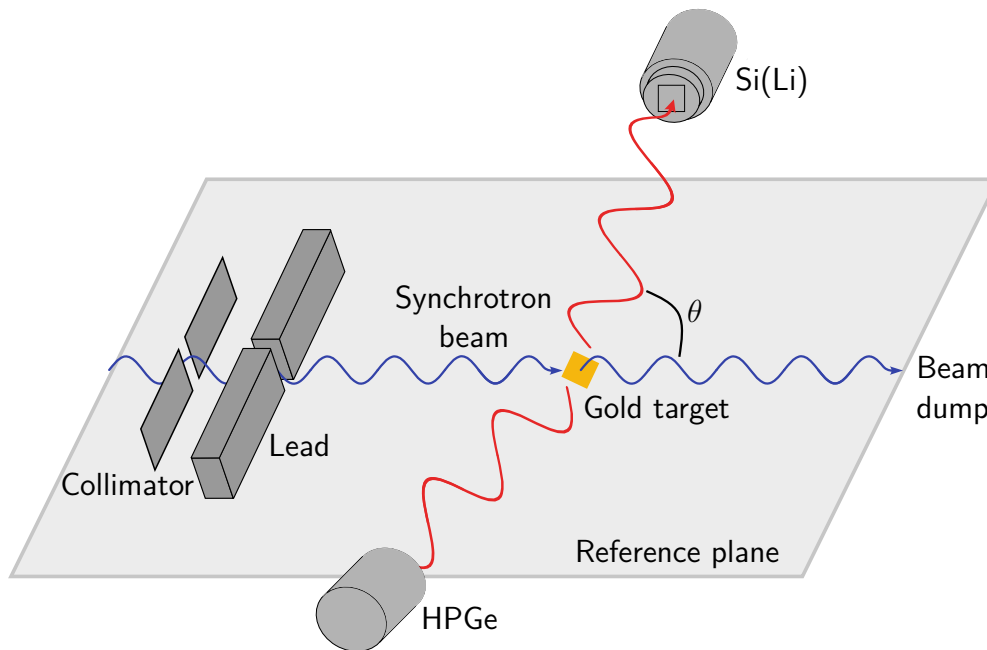
Figure 3.5: Schematic representation of the experimental setup. To shield the detector from radiation scattered at the collimator, lead shielding was installed. The collimated beam entered an evacuated target chamber which is not displayed for clarity. A HPGe detector was positioned in the reference plane and a Si(Li) detector in as well as out of the reference plane under different scattering angles. Adapted from [27].

In figure 3.5 the setup of the experiment is presented. The photons enter from the left with a linear polarization that is orientated in the reference plane. First, the PETRA III beam passes through a collimator, followed by lead shielding around the beam path. To suppress the unwanted scattered photons from the collimator, the shielding is necessary. The collimated beam enters the target chamber. It is a vertical cylinder with a diameter of 450 mm and a height of 380 mm. In figure 3.5, the chamber is not displayed for better clarity. During the experiment, the target chamber was evacuated to a pressure between $\approx 4 \cdot 10^{-6}$ mbar and $\approx 6 \cdot 10^{-6}$ mbar. If the experiment were realized at normal pressure, the scattering of photons at particles from the ambient air would dramatically disturb the measurement. To minimize this effect, several meter long beam-tubes were mounted on the target chamber. They are positioned in front of and behind it in the beam line. Both tubes as well as all other flanges on the target chamber were equipped with 50 μm thick stainless steel windows. The two detectors were mounted as close as possible to the various viewports and thus outside

Table 3.1: Overview of the measurement positions of the two detectors. Here the position is indicated by the Scattering angles. θ and φ as well as $\tilde{\theta}$ and $\tilde{\varphi}$ are defined in figure 3.4. The distance between the target and the detector crystal is given by l.

Detector	Scattering angles				l (cm)
	θ (°)	φ (°)	$\tilde{\theta}$ (°)	$\tilde{\varphi}$ (°)	
HPGe	38.7	0	39	0	47.2
	63.3	0	63	0	46.0
	87.6	0	88	0	46.5
	113.7	0	113	0	45.1
Si(Li)	63.4	0	63	0	53.4
	65.2	158	62.5	160.2	53.5
	71.7	133	63	135.7	53.6
	88.2	161	88	161	53.2
	89.1	136	88	136.5	53.3

the chamber and vacuum. Table 3.1 lists all angular positions of the flanges used in the experiment, including the distance between the target and the detector crystal.

From the top, a target holder was positioned in the center of the chamber. It is rotatable around the vertical axis. The holder provides space for five targets and was equipped with a gold foil and a fluorescence screen. Each of them can be positioned in the beam. The fluorescence screen was used for positioning. A $1\,\mu$m thick gold foil was utilized as the main target. Since the mean free path length of $\approx 400\,\mu$m [43] in gold is much larger compared to the thickness of the foil, multiple scattering is minimized. To measure the background, an empty slot of the target holder was placed in the beam. The beam dump for the residual photons was positioned in EH4.

3.3.2   Data acquisition

Data acquisition for the Si(Li) and the HPGe detectors differs due to the large discrepancy in complexity between the two detectors. Therefore, they will be separately discussed, starting with the one for the Si(Li).

Commercial standard analog NIM (Nuclear Instrumentation Module) and VME (Versa Modular Eurocard bus) modules were used for readout. For a detailed explanation see [19]. Following, the readout chain is given for a single strip. As already discussed, the signal from the strip is first amplified by the preamplifier ("preamp") stage consisting of a field-effect transistor and a feedback resistor and capacitor, which is positioned directly on the crystal. This signal is divided into a time and an energy branch. A fast TFA (Timing Filter Amplifier) shapes the time branch signal to a short pulse. When the amplitude exceeds a set threshold, a CFD (Constant Fraction Discriminator) converts the signal to a logic pulse. The output of the CFD is split and distributed to three modules. A TDC (Time to Digital Converter) was used to obtain the infor-

mation about the timing of the event. Furthermore, the TDC increments a scalar that counts the incoming pulses per event. The third branch of the signal is a logical "OR" of all channels of the CFDs and is passed into a trigger box ("trig."). If one channel of the CFDs has a signal, the "OR" will have an output signal. This leads to the generation of a trigger signal in the trigger box.

In the energy branch the signal from the preamplifier is further magnified by the spectroscopy amplifier ("spec. amp."). Thus the pulse is spread and smoothed (low noise). The amplitude is proportional to the deposited energy in the crystal. An ADC (Analog to Digital Converter) converts the amplitude into a digital number, here betwenn 0 and 4095.
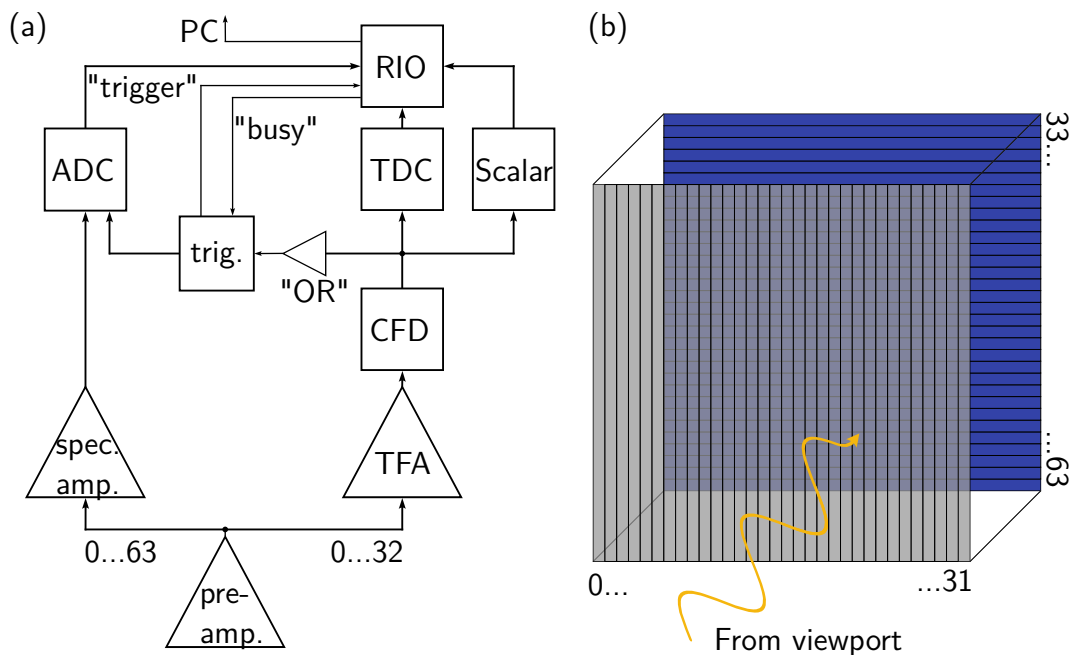
Figure 3.6: Schematic representation of the data acquisition for the Si(Li). (a) The simplified readout electronics. The numbers correspond to the connected strips. Abbreviations are explained in the text. (b) Allocation of the strip numbers. Adapted from [43].

Through the trigger signal the ADC is gated, i.e. the readout is exclusively done in the case of an output signal of the CFD. In the RIO (Remote Input Output) the outputs of the ADCs, TDCs and scalars are grouped and written to files. In addition, the RIO communicates with the trigger box and can give the signal that no further events will be accepted while an event is being readout. A schematic representation of the data acquisition for the polarimeter as well as the choice of strip numbering is shown in figure 3.6. As illustrated in figure 3.6 (a), not all strips were connected with the time branch. For the timing information it was sufficient to use only the grounded strips on the front side of the polarimeter.

The data acquisition for the HPGe detector was much simpler, since the crystal is not segmented and thus only has a single output. Moreover, the timing of the events was not of interest and therefore not detected. As with the Si(Li), the preamplifier

is mounted directly to the crystal. With a spectroscopy amplifier, the preamplified signal was shaped and spread. A commercial EASY-MCA (Multichannel Analyzer) with 4096 channels was used to convert the amplitude of the signal into a digital number. The gating was done directly by the EASY-MCA.

3.4   Overview of the measurements

In this subsection the individual measurements during the experiment are discussed. The positioning of the target chamber is given in subsection 3.4.1. Subsection 3.4.2 explains the background measurements. The determination of the strip orientation is described in subsection 3.4.3. A summary of the runs with the gold target in the beam is given in 3.4.4.

3.4.1   Beam alignment

Before the measurement, the target chamber needed to be aligned with the synchrotron beam. A laser was used to align the chamber so that the light passes through the center of it and thus passes through a position of the target holder. For this, the laser was placed in the position of the synchrotron beam. Final alignment was conducted with a fluorescence screen which was mounted on the target holder. To monitor the fluorescence, a video camera was employed at a flange equipped with a glass window.

3.4.2   Background measurement

All events measured in the detector that do not originate from photons scattered at the target are referred to as background. Primary source of background is scattering of the PETRA III beam from objects other than the target. In a previous experiment, this had a significant influence. For this reason, lead shielding was installed to minimize this issue. It is discussed in detail in [74]. Based on this knowledge, the experiment discussed in this thesis used lead shielding from the beginning, see subsection 3.3.1. Still, this measure will not yield background free data. In order to determine the residual background, test measurements were performed. Thereby an empty slot of the target holder was positioned in the beam. This was done for both detectors. Example background spectra are displayed in figure 3.7. Both spectra from figure 3.7 were measured for scattering angles of $\theta \approx 63°$ and $\varphi = 0°$. The polarimeter data shown correspond to the average energy of single hit events, see subsection 4.1.1. Due to a strong noise contribution below $5\,\mathrm{keV}$, this energy range is not displayed in both spectra for clarity. For the HPGe detector, these background measurements were performed for all positions, see subsection 3.3.1. The data from the detection runs with the gold target in the beam were corrected with the respective background spectrum. This was not done for the data of the polarimeter. Here, the background in the region of interest (above $120\,\mathrm{keV}$) is comparatively low. The applied correction for the Si(Li) detector is explained in subsection 4.3.2. Due to the substantial decreasing efficiency of the polarimeter, the measured background also declines, see figure 3.7
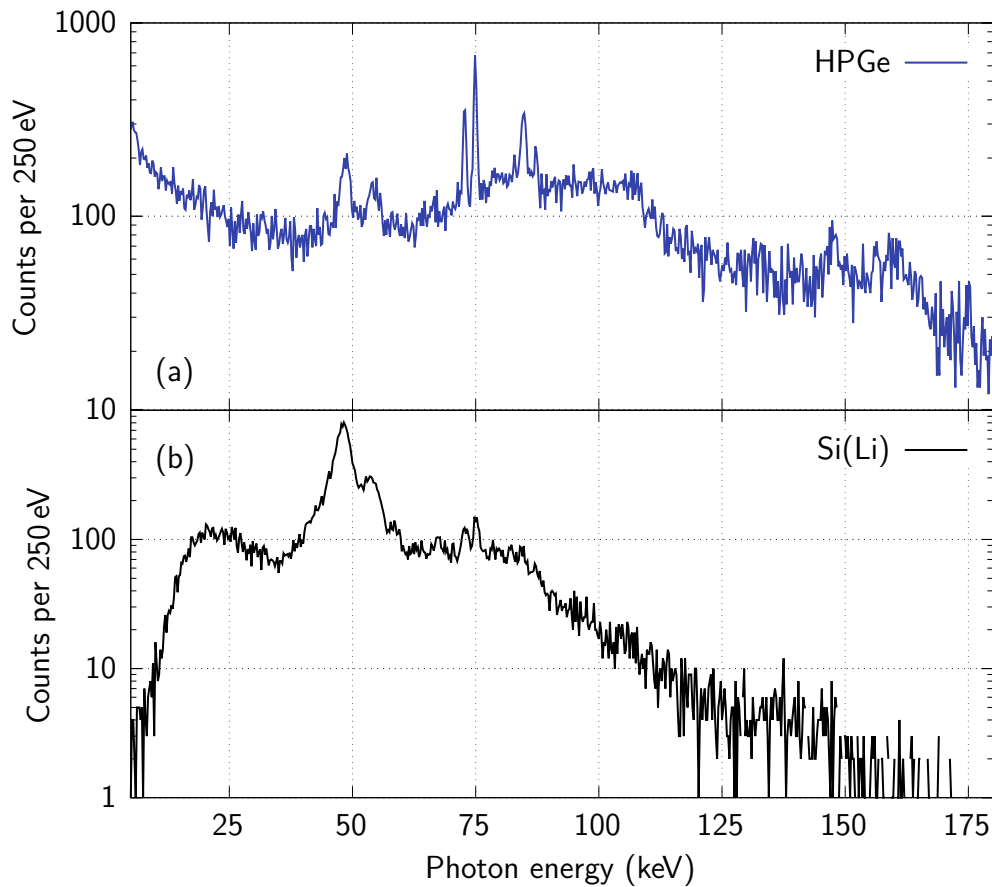
Figure 3.7: Background energy spectra for scattering angles of $\theta \approx 63°$ and $\varphi = 0°$. The HPGe detector spectrum is shown in (a) and the one of the polarimeter in (b). The energy calibration is discussed subsection 4.1.3.

(b).

As discussed earlier, the lead shielding was used to minimize the background radiation. Especially the elastically scattered incident photons are an indicator of how good the shielding was, since they can only originate from objects other than the target. In figure 3.7 it can be seen that there is no significant contribution in this energy regime. Due to the shielding, characteristic fluorescence lines of lead are visible in both background spectra. These lines correspond to $K_{\alpha,1}$ at 74.969 keV, $K_{\alpha,2}$ at 72.804 keV and $K_{\beta,1}$ at 84.936 keV [15]. Whereby the latter can only be seen in the spectrum of the germanium detector.

The peak at $\approx$ 48.5 keV could not be identified. In figure 3.7 (b), a double-peak structure appears, indicating characteristic fluorescence. Based on the width, it can be assumed that the peak is broadened by a scattering process such as Compton scattering. The relative intensity difference between this peak and the K_α lines deviates distinctly for the two detectors. A reason for this could be the difference in the shielding of the detectors. Around the HPGe detector was a much thicker

lead shielding than around the polarimeter. Another explanation could be that most photons with this energy enter the crystal of the Si(Li) detector from the side. In addition, the efficiency in this case is significantly higher due to the larger possible penetration depth.

3.4.3 Strip orientation

In order to identify the correct allocation of the strips of the polarimeter, two measurements were performed. For this purpose, a block of metal was placed in front of the crystal in various orientations. Since the strips of the front and back side are rotated by $90°$ relative to each other, the metal was position to block a vertical and horizontal part of the detector, respectively. A radioactive source of $^{241}\mathrm{Am}$ was used as a photon source.

The used right-handed coordinate system is defined by the propagation direction of the photons in positive z-direction. In this coordinate system, the analysis of the detected histograms is performed, whereas the generation of the spectra is done in respect of looking in direction of the target. This means that the detector "sees" the photons propagating towards it. The two measurement setups and the resulting histograms are displayed in figure 3.8.

3.4.4 Summary of main runs

The individual beam runs are summarized in table 3.2. For each run the used detectors and their position, defined by the scattering angles, are listed. Furthermore, the duration of the measurements with the beam on target and of the background detection are given.

Table 3.2: Beam runs in chronological order.

Run	Detector	Scattering angle (°)		Duration (min)	
		θ	φ	Background	Beam on Target
1	Si(Li)	65.2	158	91	995
	HPGe	63.3	0	30	30
2	Si(Li)	88.2	161	85	1105
	HPGe	87.6	0	30	30
3	Si(Li)	89.1	136	/	780
	HPGe	38.7	0	30	30
4	Si(Li)	71.7	133	65	727
	HPGe	113.7	0	30	30
5	Si(Li)	63.4	0	40	1133
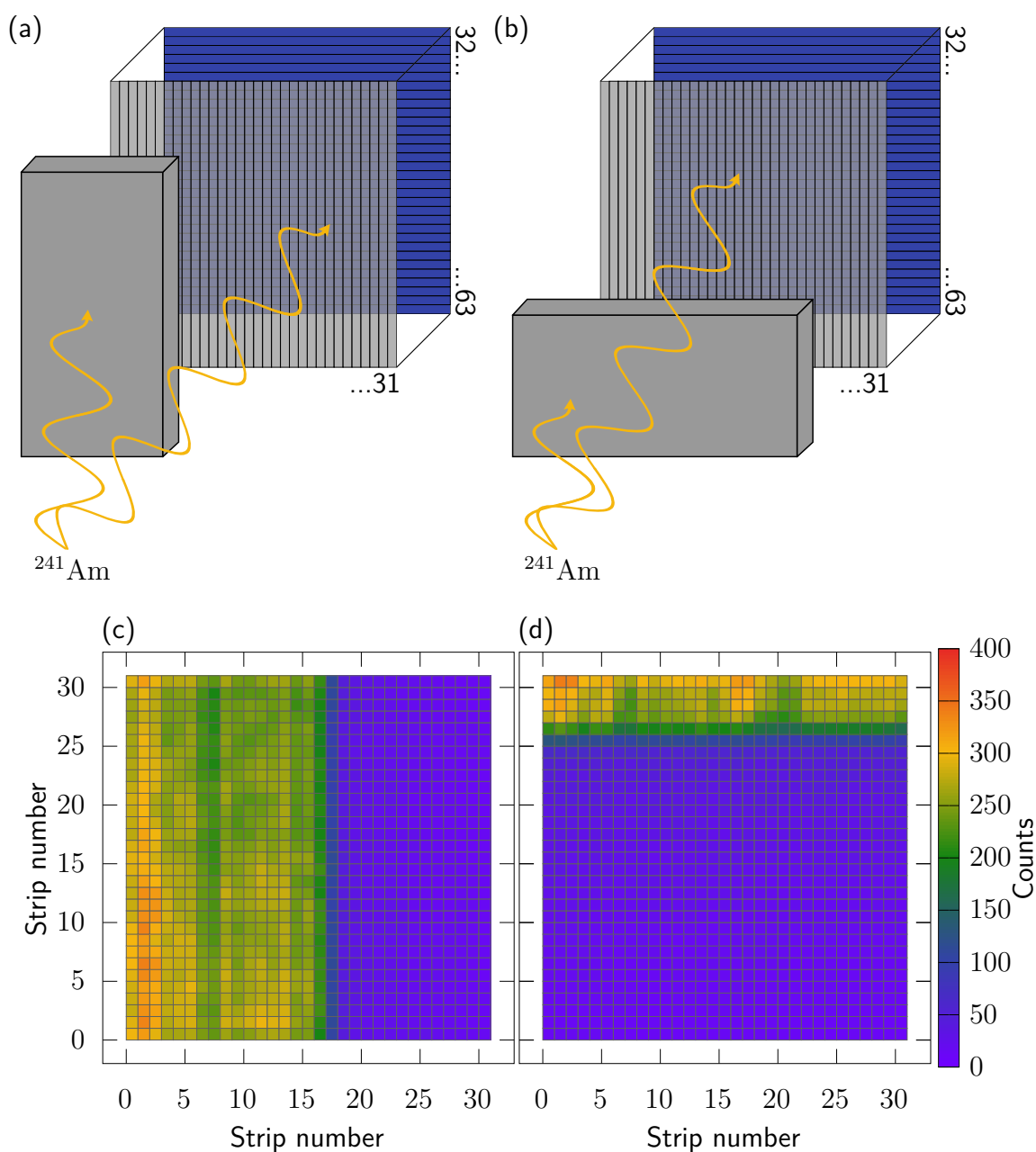
Figure 3.8: Schematic representation of the two measurements to determine the strip orientation of the polarimeter, where a metal block was positioned (a) vertically and (b) horizontally in front of the detector. In (c) and (d) are the corresponding histograms with respect to the detector that "sees" the beam propagating towards the crystal.

4 Analysis

The analysis leading to the final results of the polarization properties is explained in this section. These are the Stokes parameter P_1 and P_2 or the degree of linear polarization P_L and the polarization angle χ, respectively. For the incident PETRA III beam as well as the scattered photons, these parameters are calculated. The different types of spectra used in this thesis and the corresponding conditions to fill them are described in subsection 4.1. In subsection 4.2, the determination of the scattering angles θ and φ are explained. The analysis of the polarization of the scattered photons, based on the measured data, is discussed in subsection 4.3. Subsection 4.4 describes the relation between the polarization of the incident and the scattered photons.

4.1 Generation of spectra

This subsection describes the conditions for filling the various spectra. Different types of events can be analyzed from the data of the polarimeter. These events differ in the number of strips that detected a valid signal. A signal from a strip is valid if the measured energy is in a certain range. The lower limit is a set threshold that is adjusted for each strip. This threshold was fixed slightly below the high energy end of the noise level, to eliminate most of the noise. Through the allowed voltage range of the ADC, the upper limit is defined. For the polarimeter, only events where one or two strips from the front- and backside of the crystal had a valid signal are considered in this thesis. The generation of the resulting spectra is discussed in subsection 4.1.1 and 4.1.2. Here, the crystal of the HPGe detector was considered as a single strip. The spectra were therefore generated similarly to the case of a signal from one strip per side from the Si(Li) detector. Energy calibration is necessary to extract the energy information from the ADC channels and is discussed in subsection 4.1.3.

4.1.1 Single hit spectra

The HPGe detector records only single events, i.e. one measured energy value per event, since the crystal has no segmentation. Due to the segmentation of the polarimeter, the definition of a single hit is different. Events where exactly one strip from the front and one from the back detect a signal are defined as a single hit. These two signals from the front- and backside are averaged to determine the energy of the event. It is possible to include events with more than one strip per detector side that have a valid signal. Here, the cloud of charge carriers is distributed across two adjacent strips. In this case, the energy of each strip per detector side is summed before the average of both sides is taken. This would increase the statistics, but also the noise contribution, accumulated from the strips. The latter results in a broader spectrum. To avoid this effect, only single hit events as defined above were used to generate the spectra. For all measurement positions of the Si(Li) detector these single hit spectra were used for energy calibration, see subsection 4.1.3. Furthermore, for both detectors, the determination of the polar scattering angle θ was done with the single hit spectra, see subsection 4.2.

4.1.2   Compton polarimetry spectra

Compared to the direct absorption of the photon, Compton scattering in the crystal forms the basis for Compton polarimetry. For Compton scattered photons, the Stokes vector S' given in equation (2.16) depends on both, the polar θ and the azimuhtal φ scattering angle, as well as the Stokes vector of the incident beam. The angle-dependent intensity $I_{\mathrm{det}}(\theta, \varphi) = S_{\mathrm{scat},0}(\theta, \varphi)$ is given as follows

$$I_{\mathrm{det}}(\theta, \varphi) = (1, 0, 0, 0) \cdot \hat{T}(\theta) \cdot \hat{M}(\varphi) \cdot \boldsymbol{S}$$
$$\propto (1, 0, 0, 0) \cdot \hat{T}(\theta) \cdot \hat{M}(\varphi) \cdot \boldsymbol{P}. \tag{4.1}$$

From the measured intensity I_{det} the Stokes vector $\boldsymbol{P}$ is derived. As explained in subsection 2.2.3, the Si(Li) detector is not sensitive to the circular polarization component P_3. Thus, it cannot be determined in the experiment discussed in this thesis. The remaining components P_1 and P_2 corresponding to the linear polarization are analyzed.

In the following, the conditions for the events that fill the θ-φ-spectrum are discussed. Since both the Stokes parameters and the scattering angles are used in several phases of the experiment, a distinct nomenclature will be given. For the PETRA III beam, the Stokes vectors are denoted by the subscript "inc" and for the scattered photons at the target, the parameters are denoted by "scat". In the crystal, the scattering angles as well as the intensity are denoted by "det". For clarity, the nomenclature for all parameters are shown in figure 4.1. Consequently, the variables in equation (4.1) are now $\theta = \theta_{\mathrm{det}}$, $\varphi = \varphi_{\mathrm{det}}$ and $\boldsymbol{P} = \boldsymbol{P}_{\mathrm{scat}}$.

It is essential for Compton polarimetry to reconstruct the Compton scattering events. This requires that the absorption of the photon and the electron occur inside the detector crystal and in separate strips. The simplest structure is a valid signal from two strips from both crystal sides. A different signature would be the case when two strips on one side and one strip on the other side have a valid signal.

Lets consider now the first case. Here, the energy of the x- and y-strips is defined as $E_{x1} > E_{x2}$ and $E_{y1} > E_{y2}$, respectively. Since the energy of the incident photon beam is smaller than $\frac{1}{2} m_e c^2$, E_{x1} and E_{y1} correspond to the energy of the photon and E_{x2} and E_{y2} to the energy of the electron. As discussed in subsection 4.1.1, the average of the two corresponding strips of each detected absorption is taken. This results in

$$E_{\mathrm{ph}} = \frac{E_{x1} + E_{y1}}{2}, \quad E_{\mathrm{el}} = \frac{E_{x2} + E_{y2}}{2} \quad (2\,x\text{-strips}, 2\,y\text{-strips}), \tag{4.2}$$

where E_{ph} is the energy of the photon and E_{el} the energy of the electron.

Compton scattering can also be measured when three strips record a valid signal. This will be demonstrated by the example of the detection of the event by one x-strip and two y-strips. The energy for the x-strip is now defined as E_x and the energies of the y-strips are as given above. Analogues to equation (4.2), the energy of the photon and the electron are determined as

$$E_{\mathrm{ph}} = \frac{E_{y1} \cdot E_{\mathrm{av}}}{E_{y1} + E_{y2}}, \quad E_{\mathrm{el}} = \frac{E_{y2} \cdot E_{\mathrm{av}}}{E_{y1} + E_{y2}} \quad (1\,x\text{-strip}, 2\,y\text{-strips}), \tag{4.3}$$
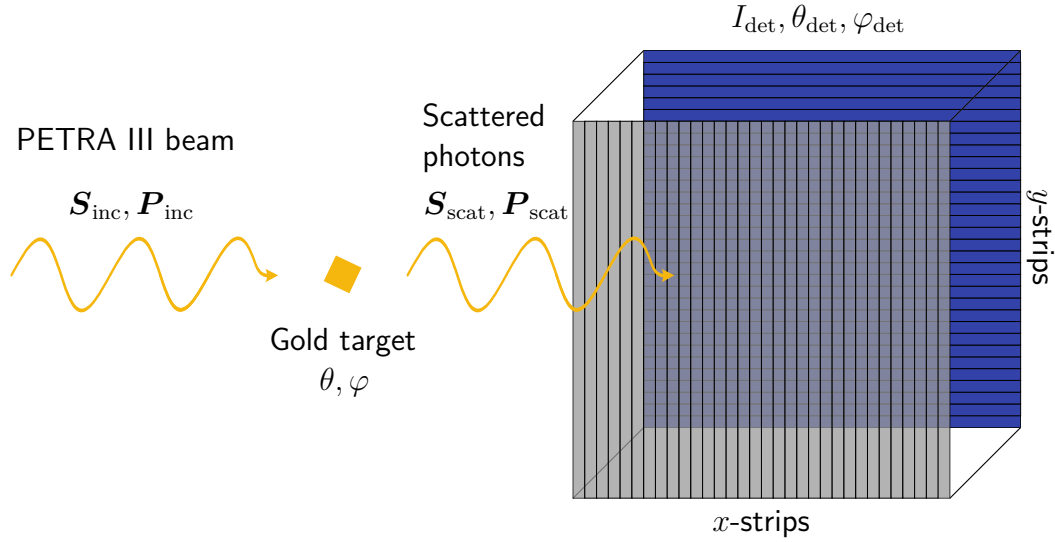
Figure 4.1: Schematic illustration of the nomenclature for the different Stokes vectors and the scattering angles. θ and φ are the scattering angles of the scattering process in the gold target and θ_{det} and φ_{det} of the scattering process in the detector. Adapted from [43].

where $E_{\text{av}} = \frac{1}{2} \cdot (E_x + E_{y1} + E_{y2})$ is the average energy of the detected event. Events where two x-strips and one y-strip recorded a valid signal were analyzed similarly.

The incident photon energy $\hbar\omega$ and the polar scattering angle θ_{det} can be calculated using the equations (2.3) and (2.4) with the results of equation (4.2) and (4.3). Let Δn_x and Δn_y be the difference in numbers of strips between the photon and electron absorption in the x- and y-directions, respectively. These differences are defined with respect to the position of the absorption of the electron. Using the strip width w and groove w_{g}, see subsection 3.2.2, the spatial distance is given as $\Delta x = \Delta n_x \cdot (w + w_{\text{g}})$ and $\Delta y = \Delta n_y \cdot (w + w_{\text{g}})$. From this, the azimuthal scattering angle φ_{det} is derived as

$$\tan(\varphi_{\text{det}}) = \frac{\Delta n_y}{\Delta n_x}. \tag{4.4}$$

Equation (4.4) is strictly valid only if the absorption occurs in the center of the strips. To include the finite strip width, a correction was performed to the distances resulting from Δx and Δy, see subsection 4.3.1.

Additional conditions for filling the Δn_x-Δn_y-histogram are the following. The positions of the absorptions should not be too close to each other. A minimum distance of $|\Delta n_x| > 1$ and $|\Delta n_y| > 1$ was defined. As a result, there is at least one strip between the absorptions. Otherwise, the uncertainty of the azimuthal angle φ_{det} would become large for these short distances between the measured signals. This would then cause an unnecessary increase of the overall uncertainty. In addition, events detected close to each other could be origin from something other than Compton scattering. Instead,

Table 4.1: Calibration lines and their corresponding peak energy from the gold target. Data for $K_{\alpha,1}$, $K_{\alpha,2}$, $K_{\beta,1}$, $K_{\beta,2}$ and $K_{\beta,3}$ are taken from [15].

Line	Energy (keV)
$K_{\alpha,1}$	68.804
$K_{\alpha,2}$	66.990
$K_{\beta,1}$	77.984
$K_{\beta,2}$	80.150
$K_{\beta,3}$	77.580
Rayleigh	175.265

they could arise by splitting the energy deposition into two neighboring strips. This is the so called charge sharing effect. The energy deposition in the crystal distributes to two adjacent strips, both of which then detect a valid signal. Furthermore, an energy condition is applied. The reconstructed energy of the photons scattered at the gold target should be in a defined range $[E_{\mathrm{min}}, E_{\mathrm{max}}]$. Through this condition, an energy interval of photons hitting the detector in the region of interest is selected. Here, two regions of length $\pm 1\,\mathrm{keV}$ and $\pm 2\,\mathrm{keV}$ were used around the chosen energies.

4.1.3   Energy calibration

The measured data are stored in steps of the ADC channels. Due to this, it is necessary to calibrate the detectors to yield the relation between the ADC value x and the deposited energy E. This has to be done for each strip of the Si(Li) detector and once for the crystal of the HPGe detector. For the calibration, a linear dependence with a offset b is assumed as follows

$$E = a \cdot x + b. \tag{4.5}$$

In the recorded spectra, the energies E_i of the two lines of the K_α and the K_β peaks as well as the Rayleigh peak are well known. The corresponding energies are listed in table 4.1. Therefore, these lines were used to determine the slope a and the offset in equation (4.5). Additional calibration measurements were therefore not required. For each of these lines, the ADC value x_i corresponds to the center of the respective line. A linear fit of all calibration peaks (x_i, E_i) yields the parameters a and b. This was done for each detector position. Figure 4.2 illustrates a calibration spectrum of the germanium detector and strip 17 of the polarimeter for the same scattering angles. As can be seen in figure 4.2, the energy resolution of the HPGe detector is significantly better than that of the Si(Li) detector. In the spectrum of the polarimeter is a large noise peak around channel 100. Since it does not contain any relevant information, the peak has been truncated for clarity. The shift between the two spectra is due to a difference in the amplification of the detector signal.
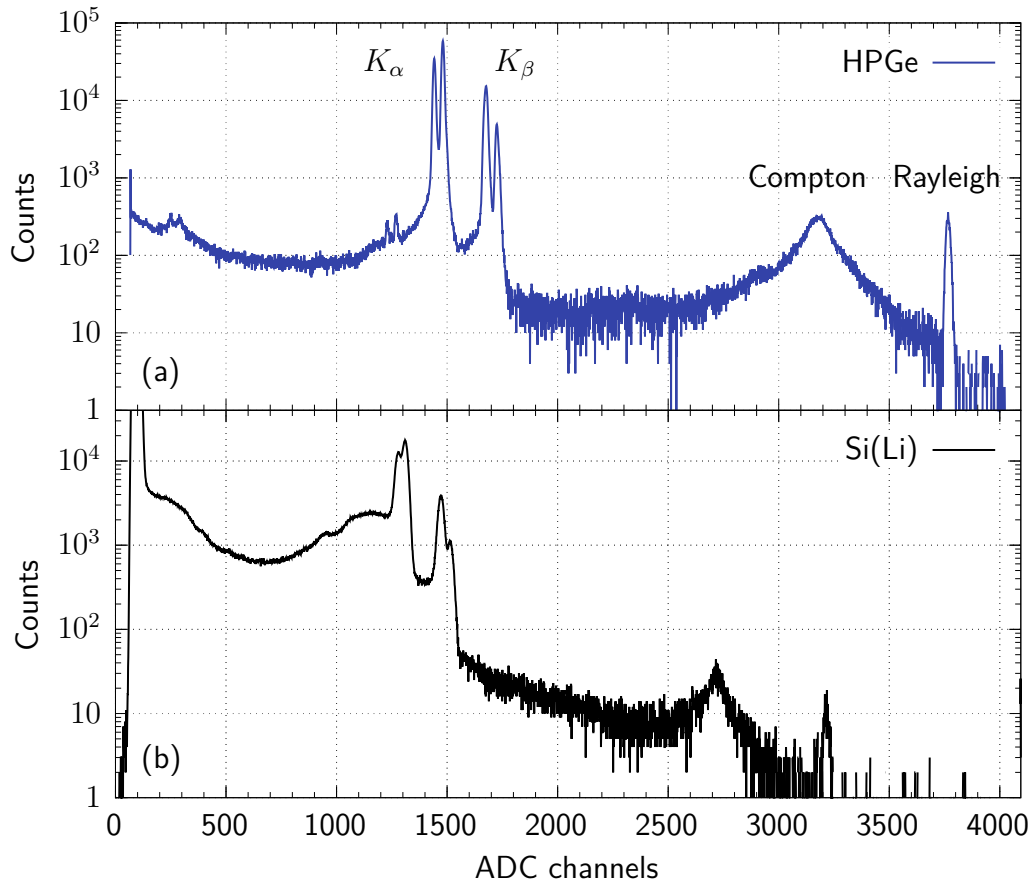
Figure 4.2: Calibration spectrum for scattering angles of $\theta \approx 63°$ and $\varphi = 0°$. The upper panel (a) shows measured data from the HPGe detector and the lower panel (b) from strip 17 of the Si(Li) detector.

4.2   Angle determination

The exact polar scattering angle θ can be determined by fitting the Compton peak with simulated Compton profiles. For the simulation, the code was provided by G. Weber [75]. 150 profiles were computed in the range of $\theta_i \pm 3°$, where θ_i are the angles used for constructing the flanges at the target chamber.

The idea is to fit a set of Compton profiles to the experimental data, to identify the corresponding profile that best aligns with the measured data. This method relies on the relation between the peak energy and the scattering angle and is defined in equation (2.3).

For the HPGe detector, the data from the experiment are corrected with the detector efficiency to get a better comparability with the simulation. This is not done for the data from the polarimeter, as it is assumed that the efficiency for the regions of interest across the Compton peak can be considered constant. Since the exact shape of the Compton profile cannot be easily described, the fit is done in several

steps. First, a Gauss function is fitted to the monoenergetic Rayleigh peak. The width of the Gaussian corresponds to the FWHM of the detector, which is used in the further calculations. The fit is performed using the Maximum-Likelihood method. This method is also used for the subsequent fits. For further information see [76].

This fit function is defined as follows: At first, an extended Compton profile is generated. Therefore, all simulated profiles belonging to a specified range around the scattering angle are superimposed. This angular range is defined by twice the size of the opening angle of the crystal, with the scattering angle in the middle. The opening angle is determined by half the width of the crystal and the distance between the target and the detector crystal. At the edges of the range a special case occurs. The profiles of the angles where the limit of the interval lies in between are added with their corresponded fractions. They are added to the number of Compton profiles as well as to the sum. This is done for the lower and upper edge of the interval. The resulting extended profile is convoluted with a Gauss function using the FWHM obtained from the Rayleigh peak. This integrates the resolution of the detector into the simulations. The obtained Compton profile is fitted to the measured data with a constant amplitude and offset. Besides the scattering angle, these two parameters are the additional fit variables.

The angle yielded from this fit is used as the polar scattering angle θ. Since not all uncertainties are accounted for in the fit, a more conservative uncertainty of $0.1°$ is used for θ than that obtained from the fit. This procedure is performed for all measurement positions of the two detectors.

The azimuthal scattering angle φ is measured at the target chamber in several steps. This results in a combined uncertainty of $\Delta\varphi = 1°$ for all φs determined.

4.3   Polarization analysis

From the analysis of Δn_x-Δn_y-spectra, the Stokes vector $\boldsymbol{P}_{\text{scat}}$ and the orientation of the polarization χ are obtained. The limitation of the distance between the absorption of the electron and the photon is discussed in subsection 4.3.1. Subsection 4.3.2 explains the background correction of the polarimeter data. The angle correction between the scattering plane and the detector plane is described in subsection 4.3.3. In subsection 4.3.4, the determination of the polarization by fitting simulations to the experimental data is explained.

4.3.1   Distance limitation

The position of the recoil electron and the absorption of the Compton scattered photon can each be assigned to a quasi-pixel. Of these pixels, the positions of the absorption of the electron and photon are given by the coordinates (x_1, y_1) and (x_2, y_2). The relative coordinates are defined as $\Delta x = x_2 - x_1$ and $\Delta y = y_2 - y_1$. From this, the definition of the absolute distance between the absorption of the photon and the electron is as follows

$$d = \sqrt{(\Delta x)^2 + (\Delta y)^2}. \tag{4.6}$$
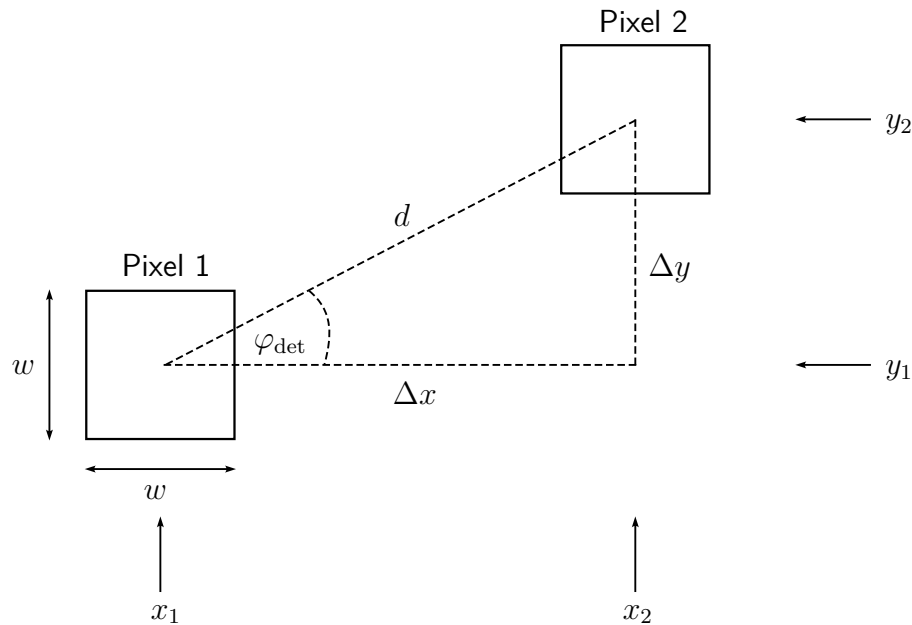
Figure 4.3: Schematic representation of the geometry of a Compton scattering event. From a combination of a front- and backside strip the pseudo-pixels are constructed. Adapted from [43].

For each event individually, the distance is calculated. The geometry of a detected Compton scattering event and all variables are displayed in figure 4.3. In the determination of φ_{det} and d with the equations (4.4) and (4.6), an uncertainty is caused by the finite pixel size. This is due to the fact that the absorption can occur at any position of the quasi-pixel. A continuous range of both parameters for each pixel combination is the result of the various possible absorption positions. For the absorption positions, the finite pixel size imposes limits on the coordinates in the following way

$$x_1 \in \left[x_{1,\mathrm{min}}, x_{1,\mathrm{max}}\right], \qquad y_1 \in \left[y_{1,\mathrm{min}}, y_{1,\mathrm{max}}\right],$$
$$x_2 \in \left[x_{2,\mathrm{min}}, x_{2,\mathrm{max}}\right], \qquad y_2 \in \left[y_{2,\mathrm{min}}, y_{2,\mathrm{max}}\right]. \tag{4.7}$$

For φ_{det} and d this results in

$$\varphi_{\mathrm{det}} \in \left[\varphi_{\mathrm{min}}, \varphi_{\mathrm{max}}\right], \qquad d \in \left[d_{\mathrm{min}}, d_{\mathrm{max}}\right]. \tag{4.8}$$

Since this uncertainty is comparatively small, it can be neglected. Thus, it is assumed that the energy deposition is always at the center of the quasi-pixel, as illustrated in figure 4.3. φ_{det} and d have a discrete value for a particular Compton event.
The distances between the Compton photons and the recoil electrons are used to determine the influence of background signals on the corresponding distances. This method is adapted from [77]. Not all double hits satisfying the conditions defined in subsection 4.1.2 are Compton events. Instead, some of them are caused by the independent absorption of two photons hitting the detector at random positions in

a particularly short time interval. For this reason, it is assumed, that the measured distance spectra can be reconstructed from the sum of a distance spectrum stemming from a pure simulated histogram and a random distance distribution, with a corresponding scaling factor. The simulations of the measurements are discussed in subsection 4.3.4. Random distances are generated by creating pairs of strip numbers. These pairs correspond to the position of the absorption of two photons. For each of these pairs, the distance was calculated with equation (4.6).

The sum of the simulation and the random distribution is fitted to the measured data. Here, the scaling factors are the fit parameters. These results are used for the distance and the background correction.

To determine whether or not the random distribution has a strong influence at a given distance, two conditions are implemented. They are defined as

$$\frac{E(i)}{s_{\mathrm{rand}} \cdot R(i)} > \frac{3}{2} \qquad \text{and} \qquad \frac{s_{\mathrm{sim}} \cdot S(i)}{s_{\mathrm{rand}} \cdot R(i)} > \frac{3}{2}, \qquad (4.9)$$

where E, R and S are the counts in the experimental, random and simulated distance histograms for the ith distance. Resulting from the fit are s_{sim} and s_{rand} the scaling factors. If one of the two ratios of equation (4.9) is not valid, the data will no longer be used in the following analysis. The largest distance at which the conditions are fulfilled, represent the new limit for the distances of the data used.
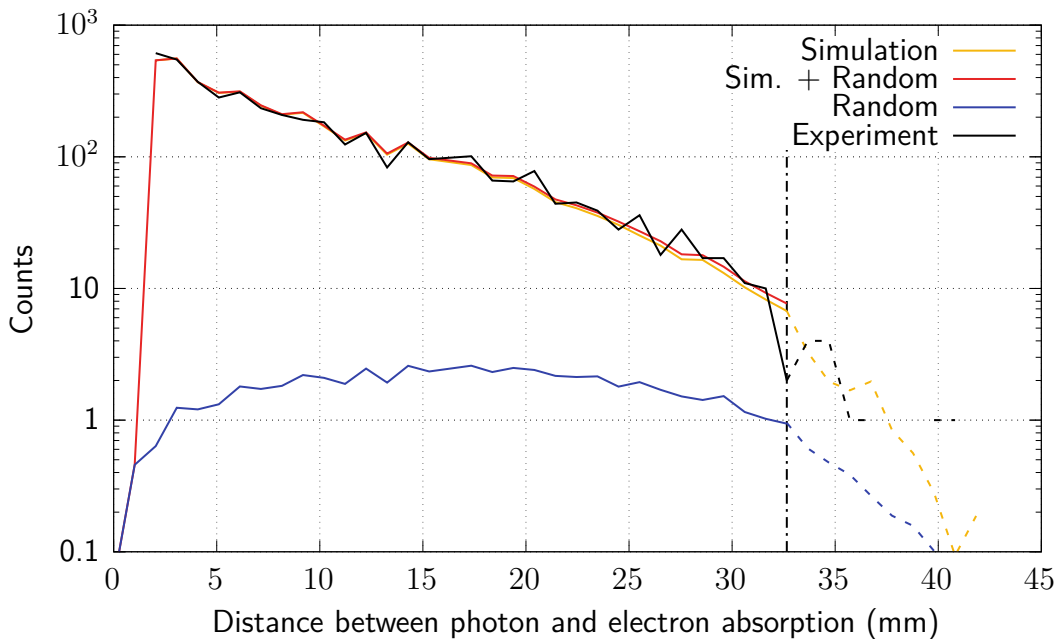
Figure 4.4: Distance correction for the detector position $\theta = 71.7°$ and $\varphi = 133°$ and a photon energy of 141.9 keV with a new maximum distance of 33 mm (dash-dot line). The distribution resulting from fitting the simulation plus the random distribution to the measured data (black) is given in red. The simulated (yellow) and the random (blue) data are multiplied by the scaling factors derived from the fit.

Since the intensity for large distances between the absorption of the photon and electron is low, a upper limit of 35 mm is set, if the conditions, given in (4.9), are satisfied up to this length. An example for the reduction of the largest distance used for the detector position $\theta = 71.7°$ and $\varphi = 133°$ and a photon energy of 141.9 keV is illustrated in figure 4.4.

4.3.2   Background correction

The polarimeter data contains background signals resulting from the signal of two strip pairs at the same event, without being real Compton event. As discussed in subsection 3.4.2, the background measurements with the Si(Li) detector are not used for the correction in the polarization analysis.

For the polarization analysis, simulated histograms were utilized, which do not contain any background. The simulated data were considered with random double hits to complement for the background signals of the experimental data. To adjust the number of random events for each simulation, the corresponding percentage of the generated distance distribution, see subsection 4.3.1, from the measured data was determined. For each of the used simulated data sets, this portion is multiplied by the length of the individual set. The resulting length represents the amount of random numbers added to the set. As a result, the experimental and simulated data contain a comparable background and no further corrective measures are required.

4.3.3   Angle correction

This subsection discusses the influence of the orientation of the front of the scattering plane relative to the x-axis of the detector. The detector is always aligned so that the scattering plane is perpendicular to the crystal surface. When the scattering and the reference plane are overlapping, the horizontal direction of the detector plane is then parallel to these. If this is not the case and the scattering plane is tilted with respect to the reference plane, the horizontal component of the detector plane is no longer parallel to the scattering plane. However, these two planes are still perpendicular to each other. The horizontal direction of the detector plane remains parallel to the reference plane. Figure 4.5 illustrates the relation between the planes. Additionally, an exemplary polarization vector is shown (yellow), which has the orientation χ with respect to the x- axis of the scattering plane.

The aim is to identify the angle difference $\delta\chi$ between the x-axis of the scattering plane and the parallel component of the detector plane, see figure 4.5. Since the orientation of the polarization χ is defined with respect to the x-axis of the scattering plane, while the polarization measurements are performed with respect to the detector axes, the result of the polarization analysis has to be corrected by this angle difference $\delta\chi$.

It is therefore necessary to determine the orientation between the axes of these two planes. The difference of the angle can be calculated between the normal vector of the scattering plane and the vertical direction of the detector plane. To determine the orientation of the axes of these planes in the lab frame, it is required to rotate
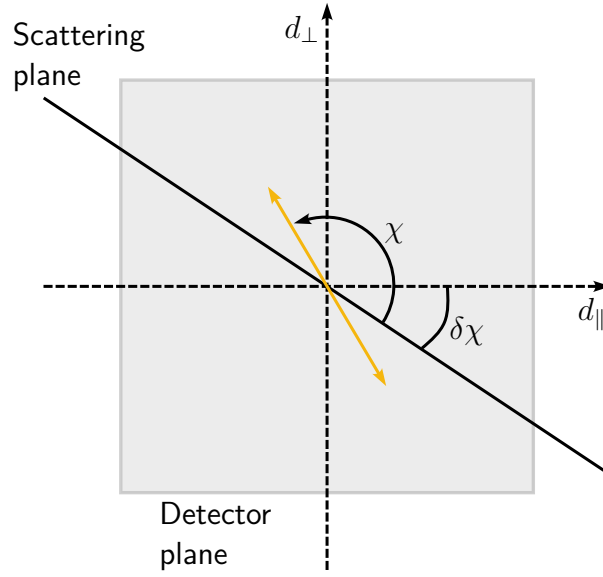
Figure 4.5: Schematic representation of the relation between the scattering and detector plane. The scattering plane is visualized by a solid black line and the orientation of the polarization in yellow. The photons propagate out off the plane towards the reader.

vectors for the coordination transformation. The basic rotation matrices for a rotation around a single axis are defined as [78]

$$\hat{R}_x(\alpha) = \begin{pmatrix} 1 & 0 & 0 \\ 0 & \cos(\alpha) & -\sin(\alpha) \\ 0 & \sin(\alpha) & \cos(\alpha) \end{pmatrix}, \; \hat{R}_y(\alpha) = \begin{pmatrix} \cos(\alpha) & 0 & \sin(\alpha) \\ 0 & 1 & 0 \\ -\sin(\alpha) & 0 & \cos(\alpha) \end{pmatrix}$$

$$\text{and} \quad \hat{R}_z(\alpha) = \begin{pmatrix} \cos(\alpha) & -\sin(\alpha) & 0 \\ \sin(\alpha) & \cos(\alpha) & 0 \\ 0 & 0 & 1 \end{pmatrix}. \tag{4.10}$$

Combining the three matrices given in equation (4.10) forms the general rotation matrix around an arbitrary vector $\boldsymbol{v}$. It is given as [79]

$$\hat{R}(\alpha, \boldsymbol{v}) = \begin{pmatrix} v_1^2 \cdot \xi + \cos(\alpha) & v_1 \cdot v_2 \cdot \xi - v_3 \cdot \sin(\alpha) & v_1 \cdot v_3 \cdot \xi + v_2 \cdot \sin(\alpha) \\ v_1 \cdot v_2 \cdot \xi + v_3 \cdot \sin(\alpha) & v_2^2 \cdot \xi + \cos(\alpha) & v_2 \cdot v_3 \cdot \xi - v_1 \cdot \sin(\alpha) \\ v_1 \cdot v_3 \cdot \xi - v_2 \cdot \sin(\alpha) & v_2 \cdot v_3 \cdot \xi + v_1 \cdot \sin(\alpha) & v_3^2 \cdot \xi + \cos(\alpha) \end{pmatrix}$$
$$\tag{4.11}$$

where $\xi = (1 - \cos(\alpha))$ and

$$\boldsymbol{v} = \begin{pmatrix} v_1 \\ v_2 \\ v_3 \end{pmatrix} \tag{4.12}$$

corresponds to the orientation of the axis around which the rotation is performed.

In the lab frame, the incident beam propagates in the z-direction, so

$$\boldsymbol{k} \propto \begin{pmatrix} 0 \\ 0 \\ 1 \end{pmatrix}. \tag{4.13}$$

This vector has to be rotated by the two scattering angles $\tilde{\theta}$ and $\tilde{\varphi}$. First with the polar angle $\tilde{\theta}$ around the y-axis. Consequently, the orientation of $\boldsymbol{v}_y$, is defined as $v_2 = 1$ and $v_1 = v_3 = 0$. The rotation of the beam vector is calculated as

$$\boldsymbol{k}_{\text{scat}} = \hat{R}(\tilde{\theta}, \boldsymbol{v}_y) \cdot \boldsymbol{k}. \tag{4.14}$$

Additionally, the resulting vector needs to be rotated by $\tilde{\varphi}$ around the x'-axis. Rotating the x- around the y-axis with the angle $\tilde{\theta}$ yields $\boldsymbol{x}'$, which is determined as

$$\boldsymbol{x}' = \hat{R}(\tilde{\theta}, \boldsymbol{v}_y) \cdot \boldsymbol{x}. \tag{4.15}$$

The second rotation of $\boldsymbol{k}_{\text{scat}}$ by the azimuthal scattering angle $\tilde{\varphi}$ around the x'-axis follows then as

$$\boldsymbol{k}'_{\text{scat}} = \hat{R}(\tilde{\varphi}, \boldsymbol{x}') \cdot \boldsymbol{k}_{\text{scat}}. \tag{4.16}$$

For the scattering plane the normal vector can be determined using the cross product of the incident beam vector and the rotated beam vector,

$$\boldsymbol{n}_{\text{scat}} = \boldsymbol{k}_{\text{in}} \times \boldsymbol{k}'_{\text{scat}}. \tag{4.17}$$

In addition to the scattering plane, the detector plane also has to be determined. This plane is constructed with the parallel $\boldsymbol{d}_{\parallel}$ and vertical direction $\boldsymbol{d}_{\perp}$ of the detector screen as

$$\boldsymbol{d}_{\parallel} = \begin{pmatrix} 1 \\ 0 \\ 0 \end{pmatrix} \quad \text{and} \quad \boldsymbol{d}_{\perp} = \begin{pmatrix} 0 \\ 1 \\ 0 \end{pmatrix}. \tag{4.18}$$

Similar to the incident beam vector $\boldsymbol{k}$, the vectors are first rotated around the y-axis with the polar scattering angle $\tilde{\theta}$ and then around the x'-axis by the azimuthal scattering angle $\tilde{\varphi}$. After both rotations, the vectors are denoted as $\boldsymbol{d}'_{\parallel,\text{scat}}$ and $\boldsymbol{d}'_{\perp,\text{scat}}$. The angle difference is calculated from the normal vector of the scattering plane and the vertical direction of the detector plane. It is determined as

$$\cos(\delta\chi) = \frac{\boldsymbol{n}_{\text{scat}} \cdot \boldsymbol{d}'_{\perp,\text{scat}}}{\sqrt{(\boldsymbol{n}_{\text{scat}} \cdot \boldsymbol{n}_{\text{scat}}) \cdot (\boldsymbol{d}'_{\perp,\text{scat}} \cdot \boldsymbol{d}'_{\perp,\text{scat}})}}. \tag{4.19}$$

To correct the orientation of the polarization χ, this angle difference is added to the uncorrected measured angle χ_{uncor}

$$\chi = \chi_{\text{uncor}} + \delta\chi. \tag{4.20}$$

4.3.4   Fit with simulated spectra

The simulated data used in this thesis are generated with an EGS5 [80] code provided by G. Weber [75]. For each simulation, a list of energy values for each strip per event is obtained, containing the following information: Δn_x, Δn_y and the polar angle θ_{det} of the Compton scattering inside the crystal. From the resulting event lists, Δn_x-Δn_y-histograms are generated as well as the azimuthal scattering angles φ_{det} are calculated with equation (4.4). Using the definition of the Stokes vector in equation (2.10), the following Stokes vectors are generated

$$\boldsymbol{S}_{\text{unpol}} = \begin{pmatrix} I_{\text{unpol}} \\ 0 \\ 0 \\ 0 \end{pmatrix}, \boldsymbol{S}_{0°} = \begin{pmatrix} I_{0°} \\ I_{0°} \\ 0 \\ 0 \end{pmatrix}, \boldsymbol{S}_{45°} = \begin{pmatrix} I_{45°} \\ -I_{45°} \\ 0 \\ 0 \end{pmatrix},$$

$$\boldsymbol{S}_{90°} = \begin{pmatrix} I_{90°} \\ 0 \\ I_{90°} \\ 0 \end{pmatrix}, \boldsymbol{S}_{135°} = \begin{pmatrix} I_{135°} \\ 0 \\ -I_{135°} \\ 0 \end{pmatrix}. \tag{4.21}$$

$\boldsymbol{S}_{\text{unpol}}$ correspond to the Stokes vector of a completely unpolarized photon beam. The others correspond to fully polarized beams with an inclination of the polarization of 0°, 45°, 90° and 135° with respect to the x-axis of the scattering plane. I_i are the intensities of the detected simulated events. All simulations create 10^8 photons. In the simulation the generated beam diameter matches the diagonal of the crystal. The Δn_x-Δn_y-histograms correspond to the simulated polarization states for a photon energy of 146 keV are shown in figure 4.6.

To determine the polarization of the scattered photons, the experimental data are fitted with the simulations. The orientation χ and the degree of linear polarization P_L are used as the fit variables. For the fit, the distribution of θ_{det} and φ_{det} are determined for different numbers of bins. For the angular range of 360° of the azimuthal scattering angle, 15 different binnings for the distribution are used. The total number of bins varies between 20 and 34 bins. For the polar scattering angle, only angles in the interval $[30°, 150°]$ are considered. This is due to the fact that the probability of detection decrease strongly for the remaining scattering angles close to 0° and 180°. For angles close to 0° the low energy of the electron has to exceed the noise level to generate a valid signal. In addition, the scattering distribution becomes more isotropic at these angles and the data of the angles outside the range can therefore be neglected. Two sets of binning are used, with a total number of four and five bins. This results in 30 combinations, which are individually fitted.

For a consistency check, three different fit functions are used. They are defined as

$$I_1 = (1 - (P_1(P_L, \chi) + P_2(P_L, \chi))) \cdot I_{\text{unpol}} + P_1(P_L, \chi) \cdot I_{0°} + P_2(P_L, \chi) \cdot I_{45°},$$
$$I_2 = (1 + (P_1(P_L, \chi) + P_2(P_L, \chi))) \cdot I_{\text{unpol}} - P_1(P_L, \chi) \cdot I_{90°} - P_2(P_L, \chi) \cdot I_{135°},$$
$$I_3 = I_{\text{unpol}} + P_1(P_L, \chi) \cdot (I_{0°} - I_{90°})/2 + P_2(P_L, \chi) \cdot (I_{45°} - I_{135°})/2. \tag{4.22}$$

Here, P_L and χ are expressed in terms of equation (2.13) with the Stokes parameter P1 and P2 for clarity. Due to the necessity of correcting χ, given in equation (4.20),
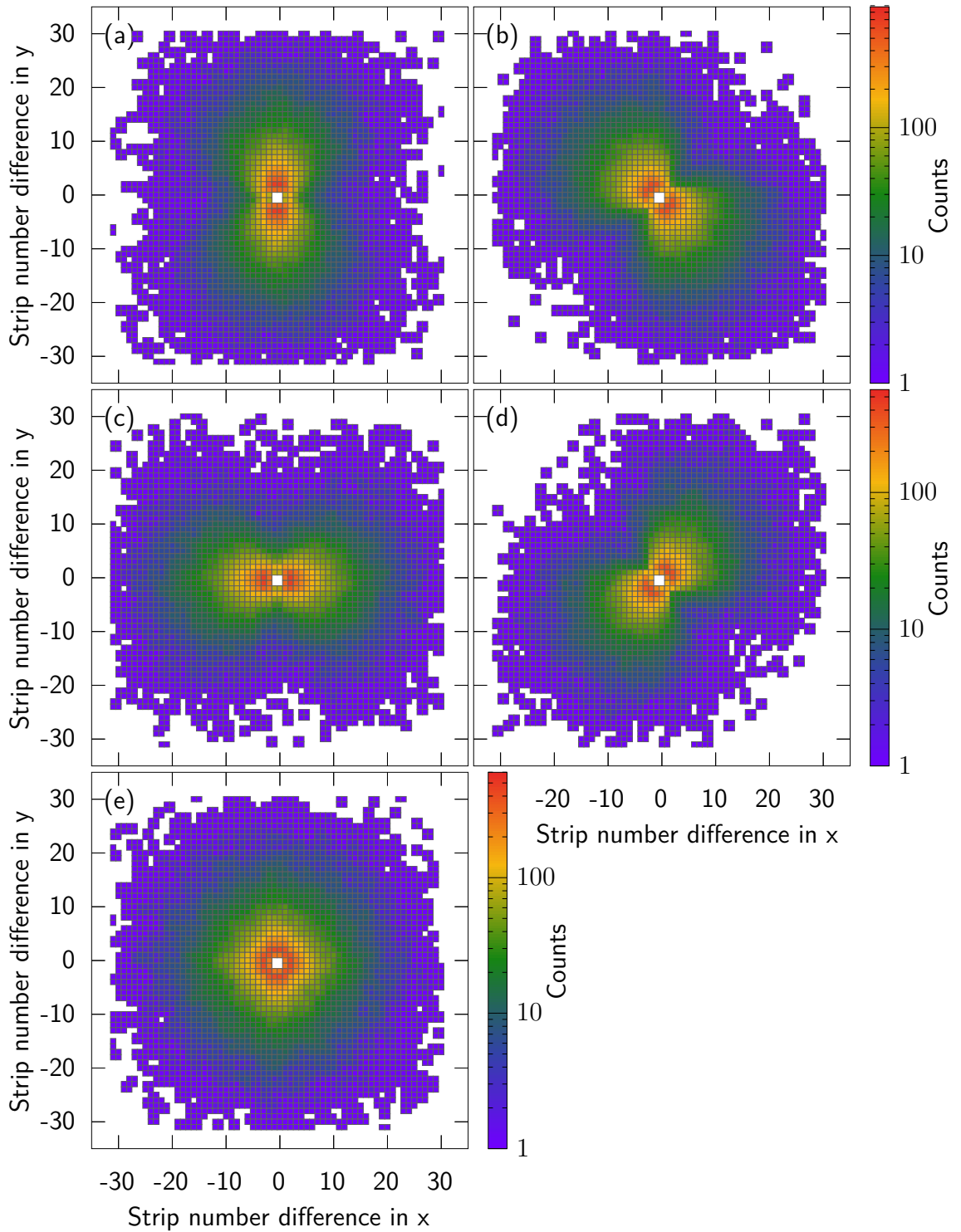
Figure 4.6: Simulated Δn_x-Δn_y-spectra for a photon energy of 146 keV. For 100% polarized photons with the orientation of (a) 0°, (b) 45°, (c) 90° and (d) 135°. (e) correspond to the Stokes vector of completely unpolarized photons.

it needs to be taken into account in the results from equation (4.22). This leads to the definition of the orientation of polarization in equation (4.22) as $\chi_{\mathrm{uncor}} - \delta\chi$, where χ_{uncor} is the fit variable. The fits are performed with the Maximum-Likelihood method based on Poisson distributed experimental data.

The three fit functions are fitted to the experimental data. For each function, the weighted means are calculated from the results of all combinations of θ_{det}-φ_{det}. The weighted mean is defined as

$$x = \left[\sum_i \frac{x_i}{\Delta x_i} \right] \cdot \left[\sum_i \frac{1}{\Delta x_i} \right]^{-1}, \tag{4.23}$$

where Δx_i is the uncertainty of x_i. Since it cannot be assumed that the x_i from the individual fitting procedures are independent, a conservative error estimation is considered. It reads

$$\Delta x = \max_i \left\{ \max \left\{ \Delta x_i, |x_i - x| \right\} \right\}. \tag{4.24}$$

As the resulting angle corresponds to χ_{uncor}, $\delta\chi$ is added to yield χ. The Stokes parameter P_1 and P_2 are determined with equation (2.13). For the values P_L, χ, P_1, and P_2 obtained from the three fit functions, the average is calculated with equations (4.23) and (4.24). They correspond to the final values of the parameters.

4.4 Scattering analysis

Calculations of the influence of the detector size as well as the polarization of the incident beam are subjects of this subsection. Using equation (2.16), the Stokes vector of the incident and scattered photons are related to each other as follows

$$\boldsymbol{S}_{\mathrm{scat}}(\theta, \varphi) = \hat{T}(\theta) \cdot \hat{M}(\varphi) \cdot \boldsymbol{S}_{\mathrm{inc}}. \tag{4.25}$$

For the relative Stokes vectors $\boldsymbol{P}_{\mathrm{inc}}$ and $\boldsymbol{P}_{\mathrm{scat}}$, which are of interest in this thesis, follows from equation (4.25)

$$\boldsymbol{P}_{\mathrm{scat}}(\theta, \varphi) = \frac{\hat{T}(\theta) \cdot \hat{M}(\varphi) \cdot \boldsymbol{P}_{\mathrm{inc}}}{(1, 0, 0, 0) \cdot \hat{T}(\theta) \cdot \hat{M}(\varphi) \cdot \boldsymbol{P}_{\mathrm{inc}}}. \tag{4.26}$$

In equation (4.26) the Stokes vector $\boldsymbol{P}_{\mathrm{inc}}$ of the incident photon beam is used to determine the Stokes vector $\boldsymbol{P}_{\mathrm{scat}}$ of the scattered photons. Up to now, it is assumed that the detector is point-like. In subsection 4.4.1, the adjustments to consider an extended detector are described. The reconstruction of $\boldsymbol{P}_{\mathrm{inc}}$, to calculate the polarization of the incident photons is explained in subsection 4.4.2. In subsection 4.4.3, the error estimations are given.

4.4.1 Detector size effects

The effect of the size of the detector crystal on equation (4.25) can be taken into account by integrating over the surface of the crystal. This is calculated for the square detection area of the Si(Li) detector. The scattering angles (θ, φ) are defined to point

to the center of the detector. Any other position of the crystal can be described by (θ', φ'). They are defined as

$$\theta' \in [\theta_{\min}, \theta_{\max}], \quad \text{and} \quad \varphi' \in [\varphi - \delta\varphi(\theta'), \varphi + \delta\varphi(\theta')], \tag{4.27}$$

where $\theta_{\min}$ and $\theta_{\max}$ are the angles with respect to the edges of the crystal and $\delta\varphi(\theta')$ corresponds to half of the angular range of the crystal depending on θ'. The integration of (4.25) is defined as

$$\boldsymbol{S}_{\text{scat}}^{(\text{ext})}(\theta, \varphi) = \int_{\theta_{\min}}^{\theta_{\max}} \mathrm{d}\theta' \sin(\theta') \cdot \hat{T}(\theta') \int_{\varphi - \delta\varphi(\theta')}^{\varphi + \delta\varphi(\theta')} \mathrm{d}\varphi' \, \hat{M}(\varphi') \cdot \boldsymbol{S}_{\text{inc}}$$

$$= \int_{\theta_{\min}}^{\theta_{\max}} \mathrm{d}\theta' \sin(\theta') \cdot \hat{T}(\theta') \int_{-\delta\varphi(\theta')}^{\delta\varphi(\theta')} \mathrm{d}\dot{\varphi} \, \hat{M}(\dot{\varphi}) \cdot \hat{M}(\varphi) \cdot \boldsymbol{S}_{\text{inc}}. \tag{4.28}$$

The subscript (ext) indicates that the extended detector size is taken into account. In equation (4.28), a variable substitution is applied in the second line. The azimuthal angle is substituted so that the detector is at $\varphi = 0°$, resulting in $\dot{\varphi} = \varphi' - \varphi$. Furthermore, the property $\hat{M}(\dot{\varphi} + \varphi) = \hat{M}(\dot{\varphi}) \cdot \hat{M}(\varphi)$ of the rotation matrix is used. Resulting from equation (4.28), the transfer matrix for the extended detector $\hat{T}^{(\text{ext})}$ reads

$$\hat{T}^{(\text{ext})}(\theta) = \int_{\theta_{\min}}^{\theta_{\max}} \mathrm{d}\theta' \sin(\theta') \cdot \hat{T}(\theta') \int_{-\delta\varphi(\theta')}^{\delta\varphi(\theta')} \mathrm{d}\dot{\varphi} \, \hat{M}(\dot{\varphi}). \tag{4.29}$$

The Stokes vector $\boldsymbol{S}_{\text{scat}}^{(\text{ext})}(\theta, \varphi)$ can then be written as

$$\boldsymbol{S}_{\text{scat}}^{(\text{ext})}(\theta, \varphi) = \hat{T}^{(\text{ext})}(\theta) \cdot \hat{M}(\varphi) \cdot \boldsymbol{S}_{\text{inc}}. \tag{4.30}$$

In figure 4.7 are the important parameters to determine $\hat{T}^{(\text{ext})}$ shown. The equally width and height of the quadratic detector crystal surface is given by w. The synchrotron beam propagates in z-direction. For the description of the crystal a new coordinate system is introduced. Its origin lies in the center of the detector surface. The unit vectors $\boldsymbol{e}_l$, $\boldsymbol{e}_{\text{h}}$, and $\boldsymbol{e}_{\text{v}}$ point in the direction from the gold target towards the detector and along the horizontal and vertical detector axes, respectively. They are illustrated in figure 4.7 and are given as

$$\boldsymbol{e}_l = \begin{pmatrix} \sin(\theta) \\ 0 \\ \cos(\theta) \end{pmatrix}, \quad \boldsymbol{e}_{\text{h}} = \begin{pmatrix} \cos(\theta) \\ 0 \\ -\sin(\theta) \end{pmatrix}, \quad \boldsymbol{e}_{\text{v}} = \begin{pmatrix} 0 \\ 1 \\ 0 \end{pmatrix}. \tag{4.31}$$

These unit vectors are used to parameterize any point $\boldsymbol{r}$ on the crystal as

$$\boldsymbol{r} = l \cdot \boldsymbol{e}_l + h \cdot \boldsymbol{e}_{\text{h}} + v \cdot \boldsymbol{e}_{\text{v}}, \tag{4.32}$$

with $h \in [-\frac{w}{2}, \frac{w}{2}]$ and $v \in [-\frac{w}{2}, \frac{w}{2}]$. Another expression for the position can be derived from θ' and $\dot{\varphi}$. Then $\boldsymbol{r}$ reads

$$\boldsymbol{r} = L \cdot \begin{pmatrix} \sin(\theta') \cos(\dot{\varphi}) \\ \sin(\theta') \sin(\dot{\varphi}) \\ \cos(\theta') \end{pmatrix}. \tag{4.33}$$
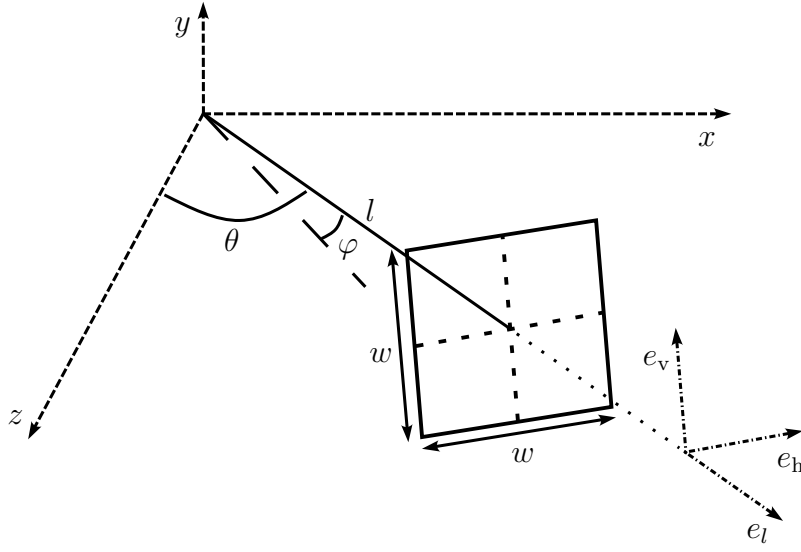
Figure 4.7: Schematic representation of the detector geometry defined for the integration in equation (4.29) to determine the transfer matrix $\hat{T}^{(\text{ext})}$. Adapted from [43].

The combination of the equations (4.32) and (4.33) yields

$$\check{L} \cdot \begin{pmatrix} \sin(\theta') \, \cos(\dot{\varphi}) \\ \sin(\theta') \, \sin(\dot{\varphi}) \\ \cos(\theta') \end{pmatrix} = \cdot \boldsymbol{e}_l + \check{h} \cdot \boldsymbol{e}_{\text{h}} + \check{v} \cdot \boldsymbol{e}_{\text{v}} \tag{4.34}$$

where $\check{L} = \frac{L}{l}$, $\check{h} = \frac{h}{l}$ and $\check{v} = \frac{v}{l}$.
The first component of the equation (4.34) results in

$$\dot{\varphi} = \arccos \left(\frac{\sin(\theta) + \check{h} \cdot \cos(\theta)}{\check{L} \cdot \sin(\theta')} \right). \tag{4.35}$$

In addition, $\check{L} = \sqrt{1 + \check{h}^2 + \check{v}^2}$ and thus a relation between $(\theta', \dot{\varphi})$ and $(\check{h}, \check{v})$ can be obtained from equation (4.34).
The calculation of the Jacobi determinant provides

$$\sin(\theta') \, \mathrm{d}\theta' \, \mathrm{d}\dot{\varphi} = \check{L}^{-3} \, \mathrm{d}\check{h} \, \mathrm{d}\check{v}. \tag{4.36}$$

For the extended detector, the transfer matrix with the new variables can be written as

$$\hat{T}^{(\text{ext})}(\theta) = \int_{-\frac{w}{2l}}^{\frac{w}{2l}} \mathrm{d}\check{h} \int_{-\frac{w}{2l}}^{\frac{w}{2l}} \mathrm{d}\check{v} \, \check{L}^{-3} \cdot \hat{T}(\theta'(\check{h}, \check{v})) \cdot \hat{M}(\dot{\varphi}(\check{h}, \check{v})). \tag{4.37}$$

θ' needs to be characterized in terms of $\check{h}$ and $\check{v}$ to calculate the transfer matrix $\hat{T}^{(\mathrm{ext})}$. From the last component of equation (4.34), θ' follows as

$$\theta' = \arccos\left(\frac{\cos(\theta) - \check{h} \cdot \sin(\theta)}{\check{L}}\right). \qquad (4.38)$$

Equation (4.38) indicates that θ' and hence $\hat{T}$ are even functions of $\check{h}$. The rotation matrix $\hat{M}$ encloses $\dot{\varphi}$ only in the form of $\sin(2\dot{\varphi})$ and $\cos(2\dot{\varphi})$, as shown by the equation (2.15). These terms are odd and even functions of $\dot{\varphi}$. This leads to the vanishing of all elements of the matrix multiplication $\hat{T} \cdot \hat{M}$ by the integration, which are proportional to $\sin(2\dot{\varphi})$. The remaining components are even functions of $\check{h}$. Applying this for an extended detector, the transfer matrix reads

$$\hat{T}^{(\mathrm{ext})}(\theta) = \int_{-\frac{w}{2l}}^{\frac{w}{2l}} \mathrm{d}\check{h} \int_{-\frac{w}{2l}}^{\frac{w}{2l}} \mathrm{d}\check{v}\ \check{L}^{-3} \cdot \begin{pmatrix} T_{00} & T_{01}\cos(2\dot{\varphi}) & 0 \\ T_{10} & T_{11}\cos(2\dot{\varphi}) & 0 \\ 0 & 0 & T_{22}\cos(2\dot{\varphi}) \end{pmatrix}, \qquad (4.39)$$

where only the upper left 3×3 part of T is considered. The matrix in equation (4.39) is similar to the transfer matrix of a point like detector given in equation (2.18). A structural difference is that there is no symmetry between T_{01} and T_{10} anymore.
Using a grid of 1000×1000 points in $(\check{h}, \check{v})$, the integrals in the equation (4.39) are calculated. For comparison between a point-like and an extended detector, $\hat{T}^{(\mathrm{ext})}$ can be divided by the solid angle covered by the detector. The solid angle is defined as

$$\Delta\Omega = \int_{-\frac{w}{2l}}^{\frac{w}{2l}} \mathrm{d}\check{h} \int_{-\frac{w}{2l}}^{\frac{w}{2l}} \mathrm{d}\check{v}\ \check{L}^{-3}. \qquad (4.40)$$

4.4.2   Calculation of the incident beam polarization

The polarization of the incident beam $\boldsymbol{P}_{\mathrm{inc}}$ can be reconstructed from the measured polarization of the scattered photons $\boldsymbol{P}_{\mathrm{scat}}(\theta, \varphi)$. Inverting equation (4.25) yields the general Stokes vector of the incident photons

$$\boldsymbol{S}_{\mathrm{inc}} = \hat{M}^{-1}(\varphi) \cdot \hat{T}^{-1}(\theta) \cdot \boldsymbol{S}_{\mathrm{scat}}(\theta, \varphi). \qquad (4.41)$$

Instead of $\hat{T}^{(\mathrm{ext})}$, $\hat{T}$ is used in the equation (4.41) for clarity.
Since $\hat{M}$ is a rotation matrix, it is always invertible. The transpose is equal to the inverse matrix $\hat{M}^{\mathrm{T}} = \hat{M}^{-1}$. A complete inversion of the transfer matrix including the integrated version is in general not possible. Only the upper left 3×3 part can be inverted. The relative Stokes vector of the incident photon beam is obtained from $\boldsymbol{S}_{\mathrm{inc}}$ as

$$\boldsymbol{P}_{\mathrm{inc}} = \frac{\hat{M}^{\mathrm{T}}(\varphi) \cdot \hat{T}^{-1}(\theta) \cdot \boldsymbol{P}_{\mathrm{scat}}(\theta, \varphi)}{(1, 0, 0, 0) \cdot \hat{M}^{\mathrm{T}}(\varphi) \cdot \hat{T}^{-1}(\theta) \cdot \boldsymbol{P}_{\mathrm{scat}}(\theta, \varphi)}. \qquad (4.42)$$

From the fourth column and row of the matrix $\hat{T}^{-1}$ all elements are set to zero. As in equation (4.41), the extended detector size can be considered by using $\hat{T}^{(\mathrm{ext})}$ instead of $\hat{T}$.

4.4.3 Error estimation

The error estimation of the Stokes vector of the incident beam $\boldsymbol{P}_{\mathrm{inc}}$, calculated with equation (4.42), and that of the scattered photons $\boldsymbol{P}_{\mathrm{scat}}$, determined with equation (4.26), are discussed.

From the scattering angles θ and φ, the distance l between target and detector, and the input Stokes parameters, either $P_{j,inc}$ or $P_{j,scat}$ depending on the equation, are the uncertainties considered. Let y be the output parameter and x_i the input quantities. Here the error of x_i is referred to as Δx_i and the resulting contribution of the overall deviation of y as Δ_{x_i}.

For the Stokes parameter P_j and thus also for $\hat{T}$ and $\hat{M}$, Δ_{x_i} is determined with $x_i \pm \Delta x_i$. Thereby, the other parameters are kept constant. The largest of these deviations is used, which is defined as

$$\Delta_{x_i} = \max \left\{ |y(x_i + \Delta x_i) - y(x_i)| \, , |y(x_i) - y(x_i - \Delta x_i)| \right\}. \tag{4.43}$$

From these individual contributions Δ_{x_i}, the total error Δy of the output parameter y is determined as

$$\Delta y = \sqrt{\sum_i \Delta_{x_i}^2}. \tag{4.44}$$

Since the distance l was measured in several steps, the uncertainty results in $\Delta d = 1 \, \mathrm{cm}$.

5 Results and discussion

The results of the experiment explained in this thesis are discussed in this section. The linear polarization of Compton scattered photons measured for various energies per detector positions are discussed in subsection 5.1. Based on the polarization of the incident beam, the theoretical predictions are calculated. The results of the reconstruction of the polarization parameters of the incident photon beam, determined with the yields of the scattered photons, are discussed in subsection 5.2.

5.1 Linear polarization of Compton scattered photons

For determining the polarization parameters, only those events that satisfy the criteria for the double hit spectrum, given in subsection 4.1.2, are used. The steps required for the analysis are described in subsection 4.3. As a result, the degree of linear polarization P_L and the orientation of the polarization χ are obtained. From these, the Stokes parameters P_1 and P_2 are calculated then with equation (2.13). The obtained results of the degree of linear polarization P_L and the orientation of the polarization χ for all analyzed points, including the corresponding theoretical values, are listed in table 5.1. In addition, figures 5.1 to 5.5 displays the obtained values of the different parameters for each detection position of the Si(Li) detector. All five figures have the same structure. The polarization parameter P_L is shown in (a), χ in (b), P_1 in (c) and P_2 in (d). In each plot, the theoretical value (dashed line) including the uncertainty (rectangle) is illustrated in green. An energy spectrum of the Compton peak is displayed in (e). Additionally, the corresponding transferred momentum to the Compton scattered photons is given in the upper x-axis in atomic units. It is equal to the projection of the electron momentum in the direction of the incident photon. In the theoretical prediction it is assumed that the electron is at rest so that only the parameters for center of the Compton peak can be determined. Due to this, the predicted theory is constant for the complete Compton peak. For the required Stokes parameters of the incident beam, the results of [27] are used, which are listed in table 5.2. See for further details subsection 5.2. As mentioned in subsection 4.1.2, two energy windows with widths of $\pm 1\,\mathrm{keV}$ and $\pm 2\,\mathrm{keV}$ are applied in the analysis. In figures 5.1 to 5.5 (e), the different analyzed energy regions of the Compton distribution are displayed with their $\pm 2\,\mathrm{keV}$ window.

Like in subsection 4.3.4, the weighted mean and the corresponding uncertainty of the results are calculated for each parameter from the yields of both energy windows. Equations (4.23) and (4.24) are used for the determination. As the influence of the transferred electron momenta to the scattered photons is of interest in this thesis, five energy windows (around E_{pos}) across the Compton profile are investigated for each measurement position of the detector. This includes the center of the peak, one window at the low energy side and three on the high energy side of the Compton peak. The latter are marked with a yellow, purple and orange dashed line in figures 5.1 to 5.5 (e). As the statistics decreases with growing distances to the peak center, also the uncertainty increases. This leads to a lower significance especially for the position furthest away from to center of the peak. Due to a large influence of photons

from other processes superimposing the Compton tail of the Compton distribution, as can be seen in figure 4.2, only one energy is analyzed on the low energy side. In figures 5.1 to 5.5 (e) it is indicated with a red dashed line. For lower energies the results would be distorted by this influence.

The obtained results in the peak center agree with the theoretical values for the two scattering angles illustrated in figure 5.1 (63.4°, 0°). In addition, the values for χ agree for the scattering angles displayed in figures 5.2 (65.2°, 158°) and 5.3 (71.7°, 133°). Unlike prediction, this is not the case for P_L. For the other two measurement positions shown in figure 5.4 (88.2°, 161°) and 5.5 (89.1°, 136°), the results for both polarization parameters do not agree with the theoretical prediction. The main reason for the deviation is the small number of the Compton peak counts, especially at the tails of the profile. In particular, this is the case for the scattering angles (88.2°, 161°), since the cross section for completely polarized incident photons is minimal at polar scattering angles of 0°, 90° and 180°.

As previously mentioned, for all five measurement positions, the uncertainties rise for an increasing distance to the peak center. For all analyzed points displayed in figure 5.1, the experimental values overlap with the theoretical predictions of P_L and χ. For P_L there could be an indication that the polarization changes for different points at the Compton peak, but this variation is not significant. The transferred electron momenta at the analyzed points across the Compton profile are the smallest at the measurement position (63.4°, 0°). This could contribute to the best agreement with the theoretical predictions. Stronger indications of a change in the polarization can be found especially for P_L and partially for χ from the obtained values of the other four detection positions. Since at four out of five scattering angles the polarization does not appear to be constant for the entire Compton peak, this suggests that the polarization is affected by the momentum of the electron. Enhancing depolarization appears to occur with increasing transferred electron momentum. One contribution could originate from the prediction that Compton scattering is completely valid only for electrons at rest. By the transformation into the rest frame of the electrons both the photon energy as well as the scattering angle change and lead to deviating results for P_L and χ. In addition, the contribution of the background increases at larger distances to the peak center and could lead to a depolarization.

Table 5.1: Overview of the results of the degree of linear polarization P_L and the orientation of the polarization χ as well as the corresponding theoretical values. They are given for all analyzed energy positions E_pos from each detection position (θ, φ) of the polarimeter.

(θ, φ) (°)	E_pos (keV)	P_L	χ (°)	$P_{L,\text{theory}}$	χ_theory (°)
(63.4, 0)	147.2	0.907 ± 0.033	0.9 ± 1.6	0.875 ± 0.029	1.5 ± 3.7
	141	0.810 ± 0.042	1.1 ± 2.5		
	150	0.912 ± 0.042	0.2 ± 1.9		
	154	0.821 ± 0.048	0.6 ± 2.7		
	158	0.826 ± 0.079	1.2 ± 3.8		
(65.2, 158)	146.1	0.857 ± 0.025	43.9 ± 1.6	0.924 ± 0.012	45.4 ± 2.3
	141	0.859 ± 0.037	42.0 ± 2.0		
	150	0.882 ± 0.047	43.3 ± 1.9		
	154	0.672 ± 0.069	44.0 ± 3.4		
	158	0.727 ± 0.078	39.0 ± 4.2		
(71.7, 133)	141.9	0.918 ± 0.018	74.5 ± 1.7	0.960 ± 0.029	74.18 ± 0.93
	135	0.858 ± 0.035	75.2 ± 2.2		
	146	0.898 ± 0.029	73.8 ± 2.0		
	150	0.898 ± 0.045	73.4 ± 2.5		
	154	0.815 ± 0.061	73.6 ± 3.0		
(88.2, 161)	131.5	0.622 ± 0.033	81.8 ± 1.8	0.736 ± 0.037	85.4 ± 1.6
	127	0.568 ± 0.044	83.1 ± 2.7		
	137	0.545 ± 0.057	71.7 ± 3.2		
	141	0.531 ± 0.079	74.4 ± 4.5		
	145	0.27 ± 0.11	63 ± 13		
(89.1, 136)	131.0	0.843 ± 0.021	87.3 ± 1.1	0.9201 ± 0.0049	89.10 ± 0.51
	127	0.801 ± 0.042	86.8 ± 2.0		
	137	0.846 ± 0.041	83.6 ± 2.0		
	141	0.738 ± 0.059	88.8 ± 3.1		
	145	0.647 ± 0.083	87.4 ± 4.5		
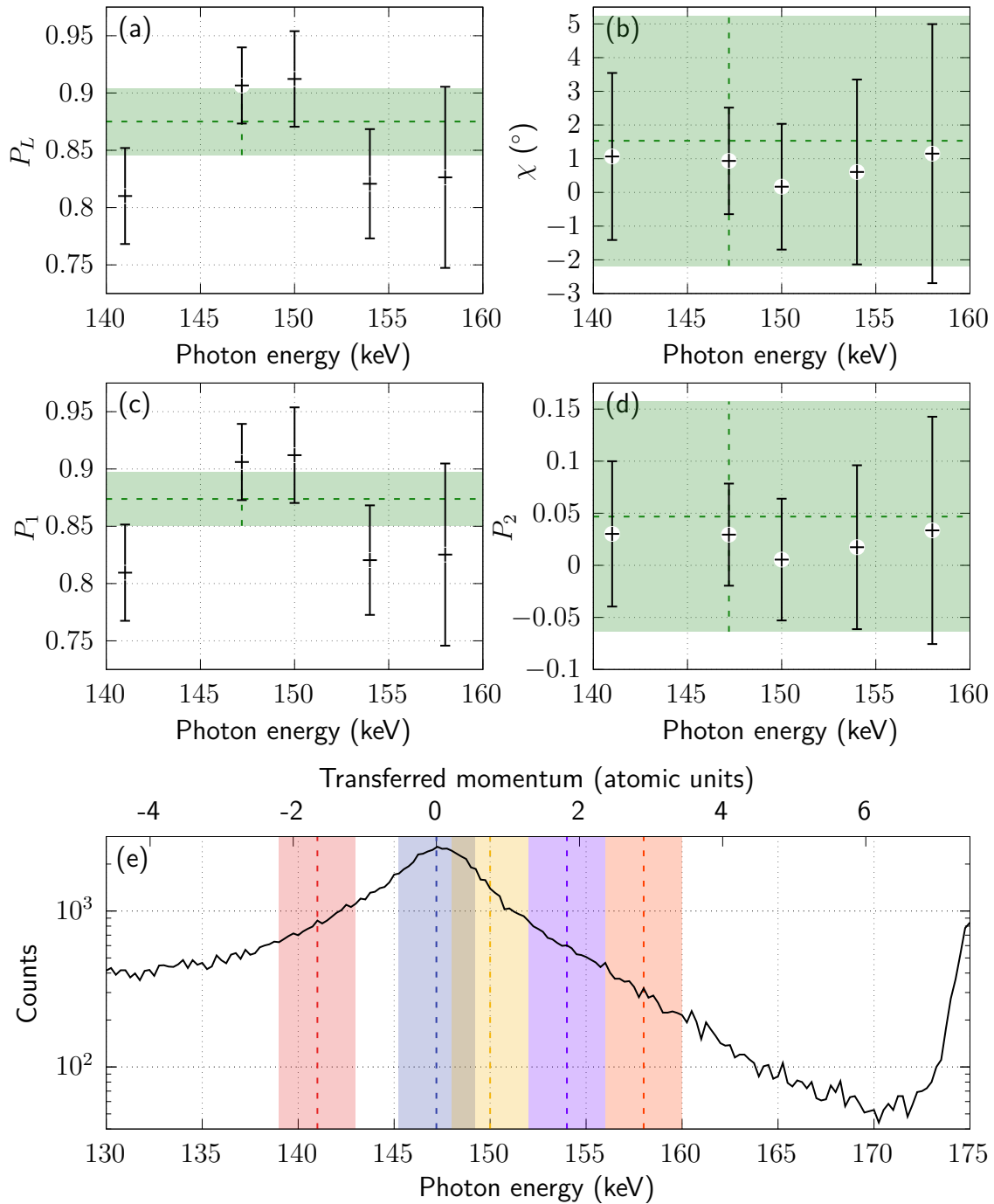
Figure 5.1: Characteristic polarization parameters of Compton scattered photons for the scattering angles $\theta = 63.4°$ and $\varphi = 0°$. (a) Degree of linear polarization P_L, (b) the orientation of the polarization χ and the Stokes parameters (c) P_1 and (d) P_2. The corresponding theoretical values for electrons at rest are indicated with a green dashed line. The uncertainty is marked by the green rectangle. (e) Single hit spectrum in the energy range of the Compton peak, including the corresponding transferred momentum. The dashed lines corresponds to the investigated energies with an energy window of $\pm 2\,\text{keV}$.
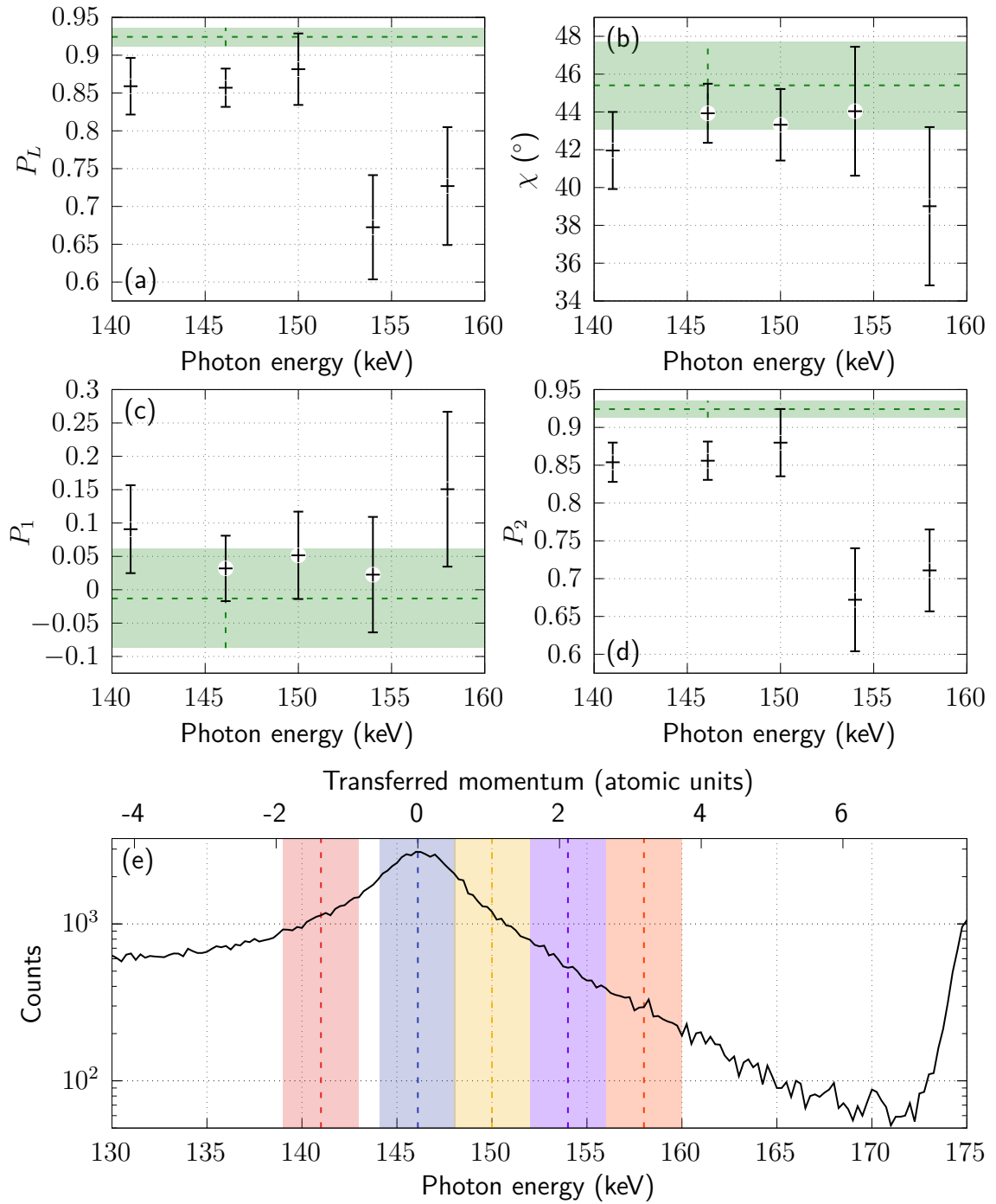
Figure 5.2: Characteristic polarization parameters of Compton scattered photons for the scattering angles $\theta = 65.2°$ and $\varphi = 158°$. For description of (a) to (e), see caption of figure 5.1.
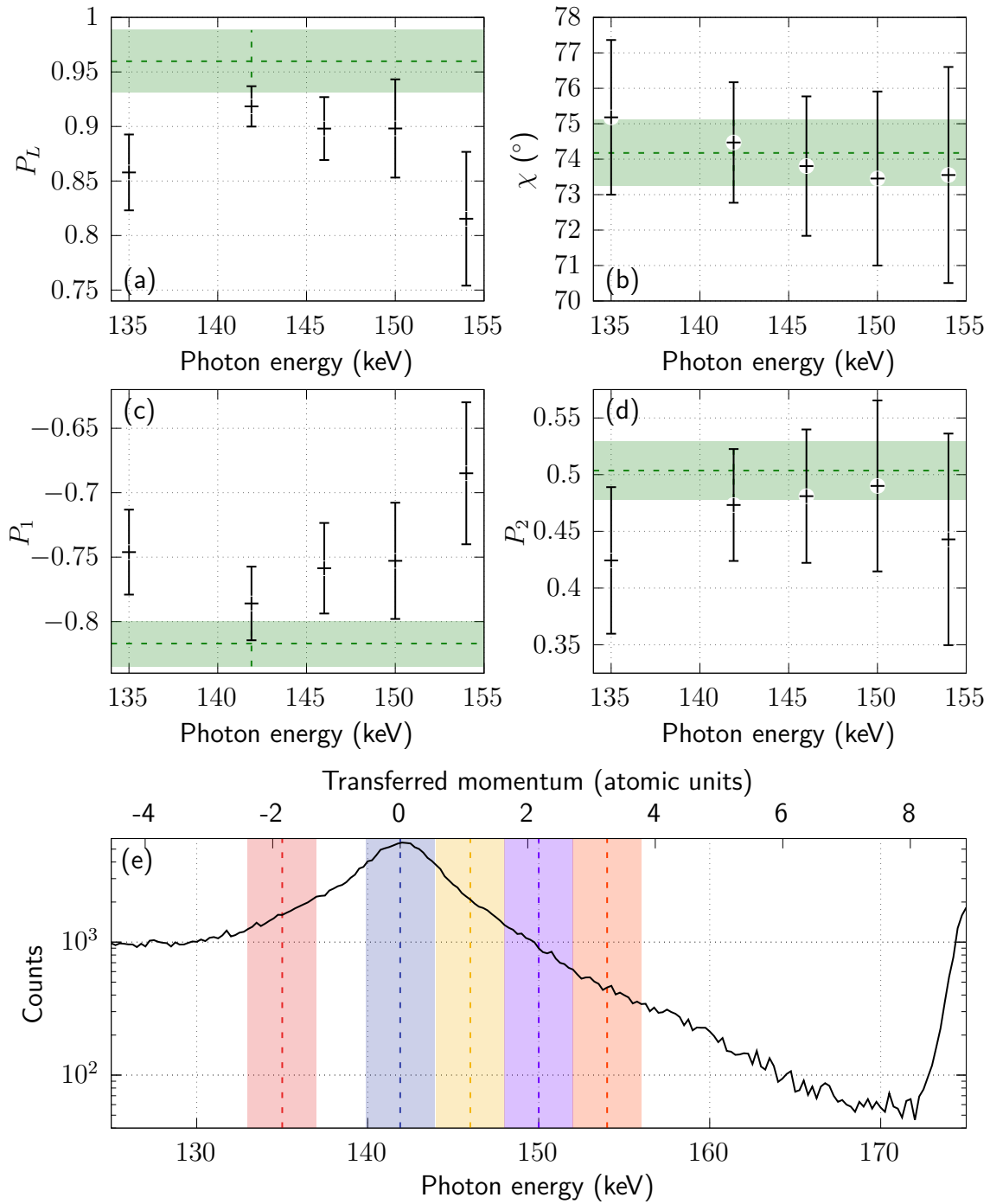
Figure 5.3: Characteristic polarization parameters of Compton scattered photons for the scattering angles $\theta = 71.7°$ and $\varphi = 133°$. For description of (a) to (e), see caption of figure 5.1.
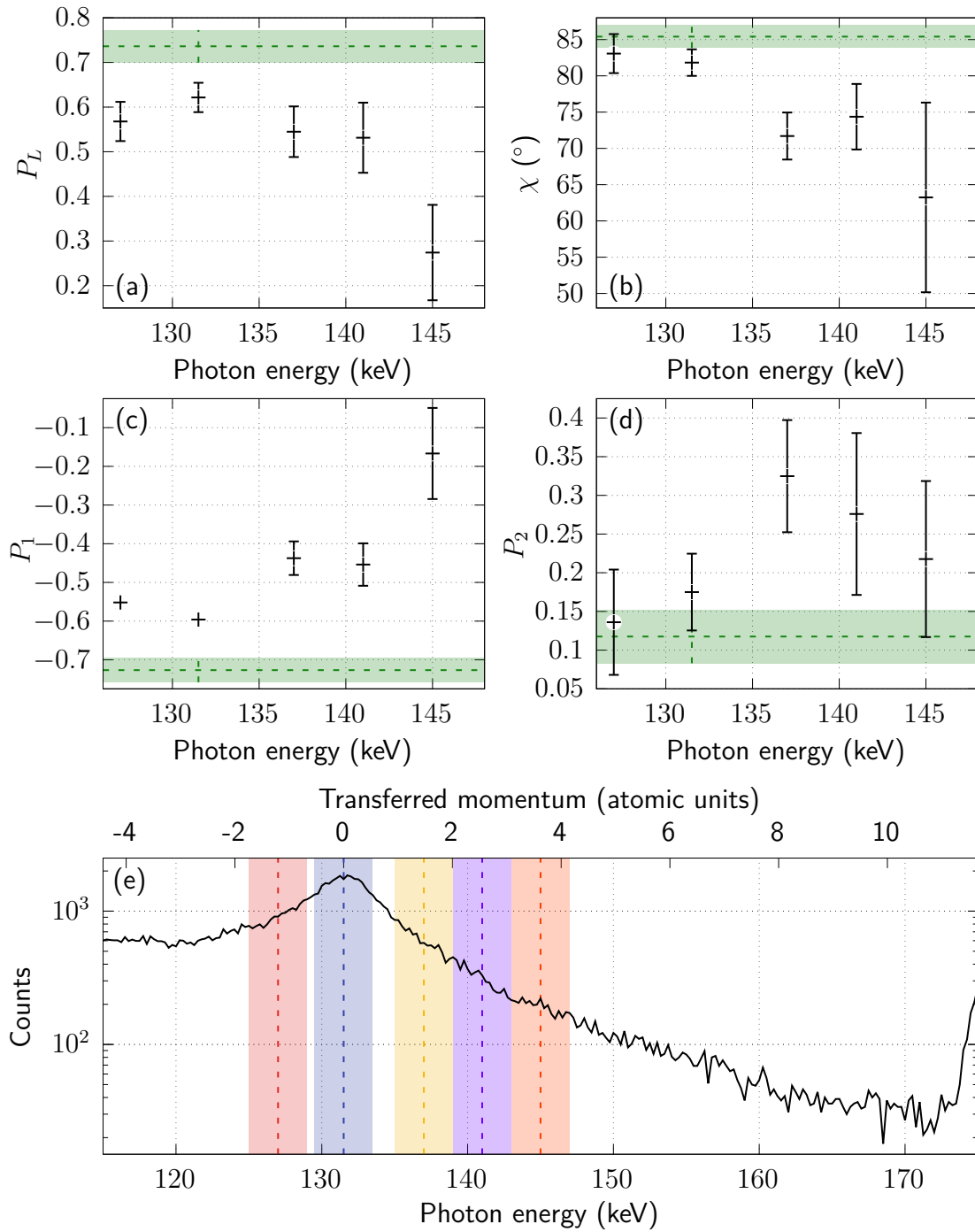
Figure 5.4: Characteristic polarization parameters of Compton scattered photons for the scattering angles $\theta = 88.2°$ and $\varphi = 161°$. For description of (a) to (e), see caption of figure 5.1.
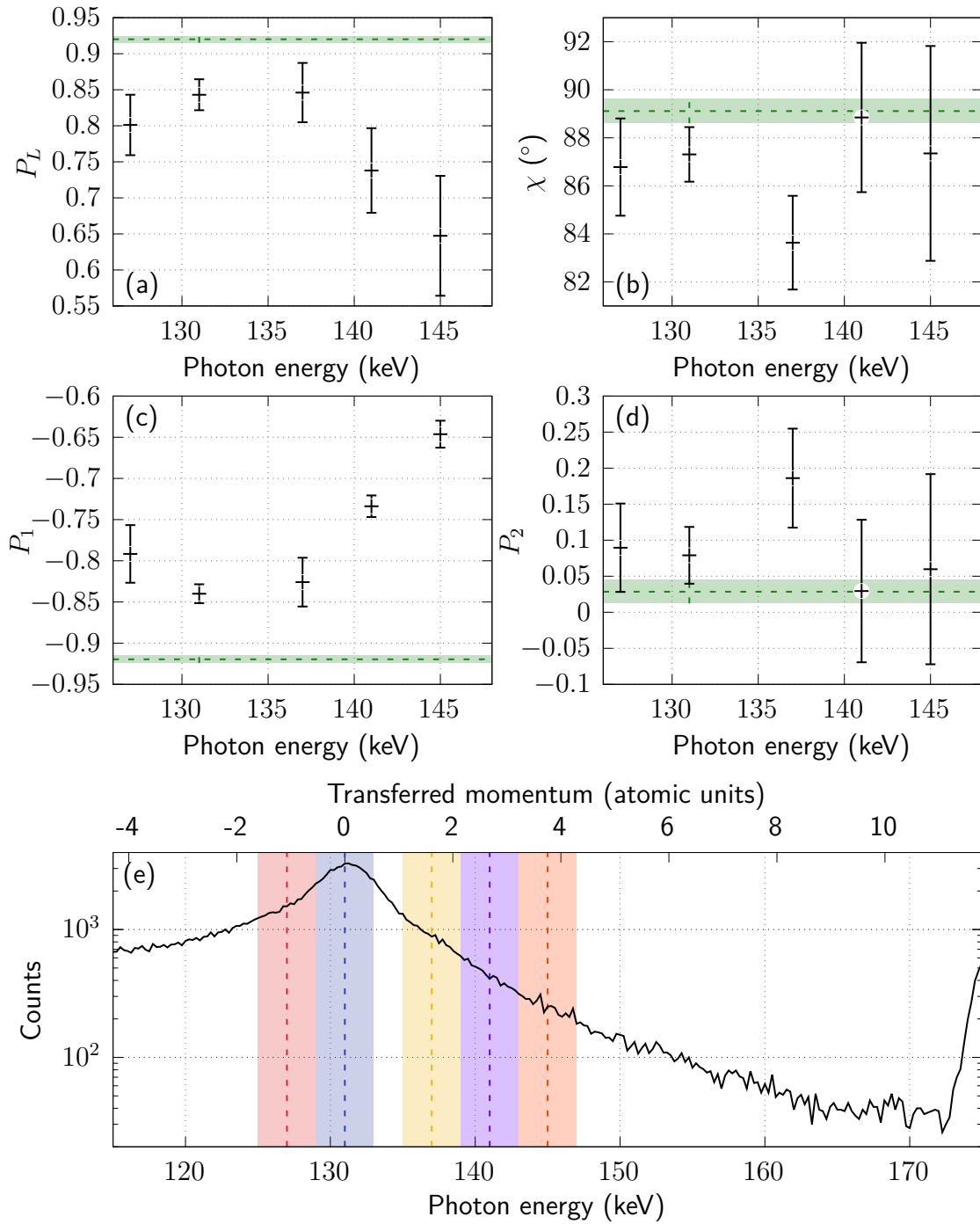
Figure 5.5: Characteristic polarization parameters of Compton scattered photons for the scattering angles $\theta = 89.1°$ and $\varphi = 136°$. For description of (a) to (e), see caption of figure 5.1.

5.2   Linear polarization of the incident beam

The calculated results of the polarization parameters $P_{1,\text{inc}}$ and $P_{2,\text{inc}}$ of the incident photon beam are discussed.

For the reconstruction, the Stokes vector P_{scat} and the transfer matrix $\hat{T}^{(\text{ext})}$ are used, as defined in (4.42). Since $\hat{T}^{(\text{ext})}$ depends on the solid angle element covered by the detector, the transfer matrix is determined for all positions. They are also utilized in the determination of the theoretical prediction in subsection 5.1. The results in the center of the Compton peak, given in table 5.1, are used for P_{scat}.

For $\varphi = 45°$ or $\varphi = 135°$, the Stokes parameter $P_{1,\text{scat}}$ of the scattered photons becomes independent from the Stokes parameter $P_{1,\text{inc}}$ of the incident beam. Due to this, the two measurement positions close to these scattering angles are only suitable for determining the polarization parameter $P_{2,\text{inc}}$ which is assumed to be close to zero. As discussed in subsection 5.1, the statistics for the scattering angles $(88.2°, 161°)$ are low and would therefore cause a large uncertainty. This is due to the minimal cross section at $\theta \approx 90°$. In addition, the contribution of the background, whose polarization is not known, is more dominant. Since two polar scattering angles are close to $90°$, these measurement points are neglected to avoid the influence of the singularity. From the remaining detection positions at $(63.4°, 0°)$ and $(65.2°, 158°)$, the weighted mean of $\boldsymbol{P}_{\text{inc}}$ is determined with equation (4.23) from the results obtained in each case. The uncertainty is calculated as before for weighted means with equation (4.24). It is assumed, that the polarization of the PETRA III beam is constant over time.

The results are summarized in table 5.2. It is expected that the incident beam is highly linearly polarized in the reference plane. Therefore P_1 should be close to $+1$ and P_2 near 0. In addition, reference values for the Stokes parameters of the incident beam are listed [27]. These reference values were obtained via an analysis of the angular-differential cross section of Rayleigh scattering. Since this can be done with a lower uncertainty, these results were used to calculate the theoretical prediction of the polarization parameters given in subsection 5.1. The obtained values in this thesis are in good agreement with the expectation as well as the results from the Rayleigh peak.

Table 5.2: Reconstructed Stokes parameters of the incident photon beam from the Compton peak. In comparison to the results from the Rayleigh peak [27].

Stokes parameter	Compton peak	Rayleigh peak
$P_{1,\text{inc}}$	$0.980^{+0.020}_{-0.040}$	0.988 ± 0.005
$P_{2,\text{inc}}$	-0.012 ± 0.058	0.023 ± 0.042

6   Summary

The polarization of Compton scattered photons was investigated in this thesis. In particular, the polarization characteristics at various positions of the Compton profile were of interest. This results in an analysis of the influence of the high electron momentum transfer at the tails of the Compton peak on the polarization of the scattered photons.

The experiment was performed at the DESY facility. Here, the High Energy Materials Science beamline P07 at the synchrotron radiation source PETRA III was used. The provided photon beam was set to an energy of $175\,\mathrm{keV}$. A $1\,\mu\mathrm{m}$ thick gold foil was used as high Z scattering target. The foil is sufficiently thin so that multiple scattering inside the target can be neglected. It was placed in a vacuum chamber. Due to the evacuated target chamber, the scattering of the beam in air is minimized. At the various flanges of the chamber, two solid state detectors were operated. The incident synchrotron beam is assumed to be highly linearly polarized parallel to the floor of the target chamber. This plane is taken as the reference plane of all measurements. In this plane, a HPGe detector was positioned for different polar scattering angles. This detector was employed to yield high resolution energy spectra. From these data, the differential cross section of Rayleigh scattering was determined [27]. The results were used to obtain the Stokes parameters of the incident beam. The second detector is a Si(Li) strip detector that was placed in- and outside the reference plane at different scattering angles. This detector serves as a highly efficient polarimeter in the hard x-ray regime based on Compton scattering on the detector crystal. With this Compton polarimeter, the linear polarization of the scattered radiation was investigated.

For the determination of the polarization parameters of the scattered radiation, the constant polarization of the synchrotron beam is employed. In addition, the Monte Carlo simulated spectra of different polarization orientations are used. The theoretical predictions were calculated using the transfer matrix formalism. For the Stokes parameters of the incident photon beam, the yields from [27] were taken as reference.

An overview of the results of the polarization parameters are given in table 5.1. The deviation of the obtained values from the different positions of the Compton profile and thus from the theoretical prediction, indicates that the polarization is not constant across the peak. Instead, a depolarization along the tails is indicated. This pattern can be seen for the degree of linear polarization P_L and the orientation of polarization χ at four of five detection positions. Therefore, the influence of the electron momentum on the polarization of the photon seems to be insufficiently taken into account. It has to be considered that for many analyzed points the statistics were relatively low, which caused comparably large uncertainties.

For the incident photons, the Stokes vector was reconstructed from the polarization parameters obtained from the Compton peak center. The data from the scattering angles $(63.4°, 0°)$ and $(65.2°, 158°)$ were used to determine $\boldsymbol{P}_{\mathrm{inc}}$. As expected, $P_{1,\mathrm{inc}}$ is close to $+1$ and $P_{2,\mathrm{inc}}$ near 0. The results obtained from the Compton peak agree with those from the Rayleigh peak, see table 5.2. Since the uncertainties are larger than the error resulting from the Rayleigh scattering analyzes, the latter values are used to calculate the theoretical polarization parameters of the scattered photons.

7 Outlook

The measured polarization parameters of Compton scattered photons indicate that the polarization varies across the peak. This shows that electron momentum needs to be taken into account in theoretical predictions, especially for high transferred electron momenta. In this domain, improved theoretical models could enhance the understanding of the polarization effects of Compton scattered photons.

To further analyze the effects of high electron momenta on the polarization, another experiment could be conducted to investigate only the photons that Compton scattered at an electron of the K-shell. Thereby, a photon Compton scatters from an electron of the K-shell. The Compton scattered and the subsequent emitted K_α or K_β photon would then be detected in coincidence. This allows to limit the analysis to Compton scattering on the K-shell electrons of the target atoms. As in the experiment discussed in this thesis, a polarimeter could be used to measure the polarization of the scattered photon. The disadvantage of this experiment is that the K_α and K_β emission occurs isotropically. Furthermore, the photon flux should not be too large, otherwise the fluorescence photon and the Compton scattered photon cannot be assigned to each other. To achieve a sufficient count rate, several detectors are required to measure the fluorescence in order to cover a large enough solid angle. HPGe detectors would be suitable for this purpose. The effect of the electron momentum is maximized for the selected scattering events, since the electrons of the K-shell have the largest momentum in any target atom. Thus, this condition deviates as far as possible from the assumptions of the impulse approximation.

The photon energy used was 175 keV, a next step could be to investigate the polarization characteristics for various scattering processes at higher energies. For example, Delbrück scattering [81, 82] gains importance among the elastic scattering processes at energies close to 1 MeV. This requires a radiation source that can provide this energy with a high degree of linear polarization. Furthermore, the polarimeter used in this thesis would not be suitable, due to the particularly low efficiency at this high energy. Only experiments with photon energies up to 300 keV can be performed with a relatively high efficiency [16]. Instead of silicon, germanium could be used as the crystal material. Germanium polarimeters have already been used in our group [83, 84]. In the energy regime of about MeV, these detectors also have a too low efficiency and have therefore not operated at such high energies. In addition, these germanium detectors were not designed as polarimeters. The pixels are not square and have a small area. This leads to a larger charge sharing, in particular at high energies. To extend the energy range, in which the Compton polarimeter used in this thesis can operate efficiently, it will be equipped with a second crystal to create a telescope Compton polarimeter [16]. Figure 7.1 shows a cross section view of the extended detector. A germanium crystal will be installed behind the silicon. The latter is then positioned behind the already existing Si(Li) crystal in a telescope structure. Like the silicon crystal, the germanium is segmented with 32 strips on the front and backside that are individually connected to a cooled preamplifier. At higher energies, the contribution of forward scattered Compton photons becomes larger. Due to the telescope structure of the detector, photons that are scattered in the forward direc-
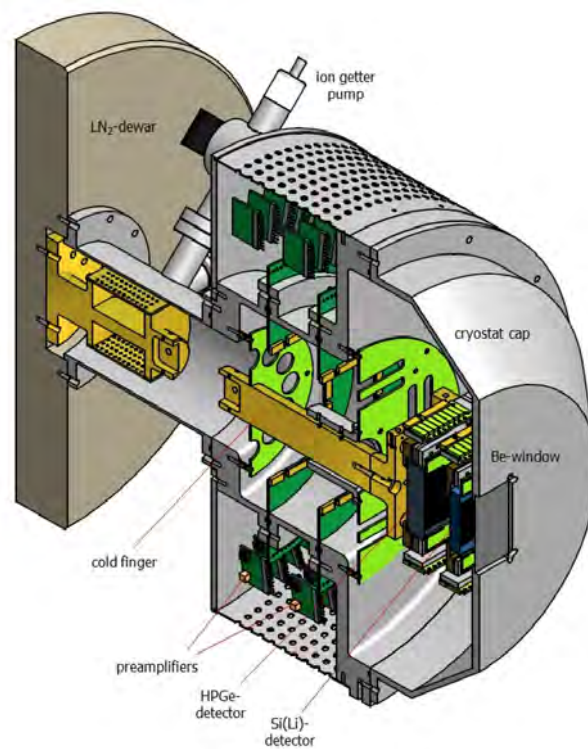
Figure 7.1: Cross section view of the extended Compton polarimeter. Adapted from [16]

tion in the silicon crystal can subsequently be absorbed by the germanium crystal. This structure of the detector can greatly increase the efficiency of the polarimeter for higher energies.

Bibliography

[1] Mulvaney S P and Keating C D 2000 *Analytical Chemistry* **72** 145–158 URL https://doi.org/10.1021/a10000155

[2] Compton A H 1923 *Physical Review* **21**(5) 483–502 URL https://doi.org/10.1103/PhysRev.21.483

[3] Compton A H 1923 *Physical Review* **22**(5) 409–413 URL https://doi.org/10.1103/PhysRev.22.409

[4] Monte E D, Fabiani S and Pearce M 2023 Compton polarimetry arXiv:2301.09934 URL https://doi.org/10.48550/arXiv.2301.09934

[5] Lowell A W, Boggs S E, Chiu C L, Kierans C A, Sleator C, Tomsick J A, Zoglauer A C, Chang H K, Tseng C H, Yang C Y, Jean P, von Ballmoos P, Lin C H and Amman M 2017 *The Astrophysical Journal* **848** 120 URL https://doi.org/10.3847/1538-4357/aa8ccd

[6] Lei F, Dean A J and Hills G L 1997 *Space Science Reviews* **82** 309–388 URL https://doi.org/10.1023/A:1005027107614

[7] Krawczynski H, Garson A, Guo Q, Baring M, Ghosh P, Beilicke M and Lee K 2011 *Astroparticle Physics* **34** 550–567 ISSN 0927-6505 URL https://doi.org/10.1016/j.astropartphys.2010.12.001

[8] Chattopadhyay T, Vadawale S V, Goyal S K, P S M N, Patel A R, Shukla R, Ladiya T, Shanmugam M, Patel V R and Ubale G P 2016 *Experimental Astronomy* **41** 197–214 URL https://doi.org/10.1007/s10686-015-9481-y

[9] Weisskopf M C, Cohen G G, Kestenbaum H L, Long K S, Novick R and Wolff R S 1976 *The Astrophysical Journal* **208** L125–L128 URL https://doi.org/10.1086/182247

[10] Chauvin M, Florén H G, Jackson M, Kamae T, Kawano T, Kiss M, Kole M, Mikhalev V, Moretti E, Olofsson G, Rydström S, Takahashi H, Iyudin A, Arimoto M, Fukazawa Y, Kataoka J, Kawai N, Mizuno T, Ryde F, Tajima H, Takahashi T and Pearce M 2015 *Monthly Notices of the Royal Astronomical Society: Letters* **456** L84–L88 ISSN 1745-3925 URL https://doi.org/10.1093/mnrasl/slv177

[11] Ribberfors R 1975 *Physical Review B* **12**(6) 2067–2074 URL https://doi.org/10.1103/PhysRevB.12.2067

[12] Ribberfors R 1975 *Physical Review B* **12**(8) 3136–3141 URL https://doi.org/10.1103/PhysRevB.12.3136

[13] Pratt R, LaJohn L, Suric T, Chatterjee B and Roy S 2007 *Nuclear Instruments and Methods in Physics Research Section B: Beam Interactions with Materials and Atoms* **261** 175–179 ISSN 0168-583X URL https://doi.org/10.1016/j.nimb.2007.03.085

[14] Blumenhagen K H, Fritzsche S, Gassner T, Gumberidze A, Märtin R, Schell N, Seipt D, Spillmann U, Surzhykov A, Trotsenko S, Weber G, Yerokhin V A and Stöhlker T 2016 *New Journal of Physics* **18** 103034 URL https://doi.org/10.1088/1367-2630/18/10/103034

[15] Thompson A, Attwood D, Gullikson E, Howells M, Kim K J, Kirz J andKortright J, Lindau I, Liu Y, Pianetta P, Robinson A, Scofield J, Underwood J, Williams G and Winick H 2009 X-ray data booklet Tech. rep. Lawrence Berkeley National Lab. (LBNL), Berkeley, CA (United States) 3rd edition URL https://cxro.lbl.gov/x-ray-data-booklet

[16] Middents W, Weber G, Spillmann U, Krings T, Vockert M, Volotka A, Surzhykov A and Stöhlker T 2021 *Annalen der Physik* 2100285 URL https://doi.org/10.1002/andp.202100285

[17] Berger M, Hubbell J, Seltzer S, Chang J, Coursey J, Sukumar R, Zucker D and Olsen K 2010 Xcom: Photon cross sections database (version 1.5) (visited on 01/03/2023) URL https://doi.org/10.18434/T48G6X

[18] Einstein A 1905 *Annalen der Physik* **322** 132–148 URL https://doi.org/10.1002/andp.19053220607

[19] Leo W R 1994 *Techniques for Nuclear and Particle Physics Experiments* 2nd ed (Springer Berlin Heidelberg) ISBN 978-3-642-57920-2 URL https://doi.org/10.1007/978-3-642-57920-2

[20] Roy S C, Kissel L and Pratt R H 1999 *Radiation Physics and Chemistry* **56** 3–26 ISSN 0969-806X URL https://doi.org/10.1016/S0969-806X(99)00286-8

[21] Thomson J 1907 *The corpuscular theory of matter* 2nd ed (London : A. Constable)

[22] Strutt H J 1871 *The London, Edinburgh, and Dublin Philosophical Magazine and Journal of Science* **41** 107–120 URL https://doi.org/10.1080/14786447108640452

[23] Strutt H J 1871 *The London, Edinburgh, and Dublin Philosophical Magazine and Journal of Science* **41** 274–279 URL https://doi.org/10.1080/14786447108640479

[24] Strutt H J 1871 *The London, Edinburgh, and Dublin Philosophical Magazine and Journal of Science* **41** 447–454 URL https://doi.org/10.1080/14786447108640507

[25] Franz W 1935 *Zeitschrift für Physik* **98** 314–320 URL https://doi.org/10.1007/BF01331074

[26] Kane P, Kissel L, Pratt R and Roy S 1986 *Physics Reports* **140** 75–159 ISSN 0370-1573 URL https://doi.org/10.1016/0370-1573(86)90018-9

[27] Middents W, Weber G, Gumberidze A, Hahn C, Krings T, Kurz N, Pfäfflein P, Schell N, Spillmann U, Strnat S, Vockert M, Volotka A, Surzhykov A and Stöhlker T 2023 *Physical Review A* **107**(1) 012805 URL https://doi.org/10.1103/PhysRevA.107.012805

[28] Klein O and Nishina Y 1929 *Zeitschrift für Physik* **52** 853–868 URL https://doi.org/10.1007/BF01366453

[29] Bergstrom P and Pratt R 1997 *Radiation Physics and Chemistry* **50** 3–29 ISSN 0969-806X URL https://doi.org/10.1016/S0969-806X(97)00022-4

[30] Salvat F and Fernández-Varea J M 2009 *Metrologia* **46** S112 URL https://dx.doi.org/10.1088/0026-1394/46/2/S08

[31] Eisenberger P and Platzman P M 1970 *Physical Review A* **2**(2) 415–423 URL https://doi.org/10.1103/PhysRevA.2.415

[32] Du Mond J W M 1929 *Physical Review* **33**(5) 643–658 URL https://doi.org/10.1103/PhysRev.33.643

[33] Pratt R, LaJohn L, Florescu V, Surić T, Chatterjee B and Roy S 2010 *Radiation Physics and Chemistry* **79** 124–131 ISSN 0969-806X URL https://doi.org/10.1016/j.radphyschem.2009.04.035

[34] Cooper M J 1985 *Reports on Progress in Physics* **48** 415–481 URL https://doi.org/10.1088/0034-4885/48/4/001

[35] Qiao C K, Chi H C, Zhang L, Gu P, Liu C P, Tang C J, Lin S T and Huang K N 2020 *Journal of Physics B: Atomic, Molecular and Optical Physics* **53** 075002 URL https://doi.org/10.1088/1361-6455/ab69a7

[36] Bergstrom P M, Surić T, Pisk K and Pratt R H 1993 *Physical Review A* **48**(2) 1134–1162 URL https://doi.org/10.1103/PhysRevA.48.1134

[37] Surić T 1992 *Nuclear Instruments and Methods in Physics Research Section A: Accelerators, Spectrometers, Detectors and Associated Equipment* **314** 240–243 ISSN 0168-9002 URL https://doi.org/10.1016/0168-9002(92)90966-8

[38] Shurcliff W A 1962 *Polarized Light* (Cambridge, MA and London, England: Harvard University Press) ISBN 9780674424135 URL https://doi.org/10.4159/harvard.9780674424135

[39] Maria Chekhova P B 2021 *Polarization of light : in classical, quantum, and nonlinear optics* Graduate (Berlin ; Boston: De Gruyter) ISBN 978-3110668018 URL https://doi.org/10.1515/9783110668025

[40] Vockert M 2022 *Radiative Elektroneneinfang als Quelle stark linear polarisierter Röntgenstrahlung* Ph.D. thesis Friedrich-Schiller-Universität Jena, Physikalisch-Astronomische Fakultät Jena URL https://www.db-thueringen.de/receive/dbt_mods_00052373

[41] Goldstein D H 2011 *Polarized light* third edition ed (Boca Raton, Fla. ; London ; New York: CRC Press) ISBN 978-1-4398-3040-6 URL https://doi.org/10.1201/b10436

[42] Stokes G G 1852 *Transactions of the Cambridge PhilosophicalSociety* **9** 399

[43] Blumenhagen K H 2016 *Experimental studies on polarization correlations in hard x-ray Rayleigh scattering* Ph.D. thesis Friedrich-Schiller-Universität Jena, Physikalisch-Astronomische Fakultät Jena URL https://www.db-thueringen.de/receive/dbt_mods_00030049

[44] McMaster W H 1961 *Reviews of Modern Physics* **33**(1) 8–28 URL https://doi.org/10.1103/RevModPhys.33.8

[45] Fano U 1949 *Journal of the Optical Society of America* **39** 859–863 URL https://doi.org/10.1364/JOSA.39.000859

[46] Kaaret P E, Novick R, Martin C, Shaw P S, Hamilton T, Sunyaev R, Lapshov I Y, Silver E H, Weisskopf M C, Elsner R F, Chanan G A, Costa E, Manzo G, Fraser G W and Perola G C 1990 *Optical Engineering* **29** 773 – 780 URL https://doi.org/10.1117/12.55660

[47] Bellazzini R, Baldini L, Brez A, Costa E, Latronico L, Omodei N, Soffitta P and Spandre G 2003 *Nuclear Instruments and Methods in Physics Research Section A: Accelerators, Spectrometers, Detectors and Associated Equipment* **510** 176–184 ISSN 0168-9002 proceedings of the 2nd International Symposium on Applications of Particle Detectors in Medicine, Biology and Astrophysics URL https://doi.org/10.1016/S0168-9002(03)01695-4

[48] Novick R 1975 *Space Science Reviews* **18** 389–408 ISSN 1572-9672 URL https://doi.org/10.1007/BF00212912

[49] Wojtsekhowski B, Tedeschi D and Vlahovic B 2003 *Nuclear Instruments and Methods in Physics Research Section A: Accelerators, Spectrometers, Detectors and Associated Equipment* **515** 605–613 ISSN 0168-9002 URL https://doi.org/10.1016/j.nima.2003.07.009

[50] Metzger F and Deutsch M 1950 *Physical Review* **78**(5) 551–558 URL https://doi.org/10.1103/PhysRev.78.551

[51] Collins S P, Laundy D, Brahmia A, Jones S, Timms D, Cooper M J and Rollason A J 1990 *Nuclear Instruments and Methods in Physics Research Section A: Accelerators, Spectrometers, Detectors and Associated Equipment* **290** 254–256 ISSN 0168-9002 URL https://doi.org/10.1016/0168-9002(90)90370-L

[52] Tashenov S 2005 *Hard X-Ray polarimetry with position sensitive germanium detectors - studies of the recombination transitions into highly charged ions (o.D.)* Ph.D. thesis Johann Wolfgang Goethe-Universität Frankfurt/Main Darmstadt URL https://repository.gsi.de/record/55441

[53] Ferguson A 1979 *Nuclear Instruments and Methods* **162** 565–586 ISSN 0029-554X URL https://doi.org/10.1016/0029-554X(79)90733-X

[54] Märtin R 2011 *Röntgenpolarimetrie angewandt zur Untersuchung der Bremsstrahlung spinpolarisierter Elektronen* Ph.D. thesis Ruprecht-Karls-Universität Heidelberg URL https://doi.org/10.11588/heidok.00012675

[55] Weber G, Bräuning H, Hess S, Märtin R, Spillmann U and Stöhlker T 2010 *Journal of Instrumentation* **5** C07010 URL https://doi.org/10.1088/1748-0221/5/07/C07010

[56] Vockert M, Weber G, Spillmann U, Krings T, Herdrich M and Stöhlker T 2017 *Nuclear Instruments and Methods in Physics Research Section B: Beam Interactions with Materials and Atoms* **408** 313–316 ISSN 0168-583X proceedings of the 18th International Conference on the Physics of Highly Charged Ions (HCI-2016), Kielce, Poland, 11-16 September 2016 URL https://doi.org/10.1016/j.nimb.2017.05.035

[57] Wille K 1992 *Physik der Teilchenbeschleuniger und Synchrotronstrahlungsquellen, Eine Einführung* (Vieweg+Teubner Verlag Wiesbaden, Springer Fachmedien Wiesbaden 1992) ISBN 978-3-519-03087-4 URL https://doi.org/10.1007/978-3-663-11850-3

[58] Peter Schmüser Martin Dohlus J R 2008 *Ultraviolet and Soft X-Ray Free-Electron Lasers, Introduction to Physical Principles, Experimental Results, Technological Challenges* Springer Tracts in Modern Physics (Springer-Verlag Berlin Heidelberg 2009) ISBN 978-3-540-79572-8 URL https://doi.org/10.1007/978-3-540-79572-8

[59] DESY. Wiggler (visited on 02/28/2023) URL https://photon-science.desy.de/sites/site_photonscience/content/e62/e189219/e189248/e189389/e196698/e189410/wiggler_eng.png

[60] DESY. Undulator (visited on 02/28/2023) URL https://photon-science.desy.de/sites/site_photonscience/content/e62/e189219/e189248/e189389/e196698/e189412/undulator_eng.png

[61] DESY. PETRA III - Facility Information (visited on 02/25/2023) URL https://photon-science.desy.de/facilities/petra_iii/facility_information/index_eng.html

[62] Helmholtz Association. Deutsches Elektronen Synchrotron (visited on 02/25/2023) URL https://www.helmholtz.de/en/about-us/helmholtz-centers/centers-a-z/centre/deutsches-elektronen-synchrotron-desy/

[63] Bieler M, Agapov I, Ehrlichmann H, Keil J, Sahoo G, Wanzenberg R *et al.* 2017 Petra iii operation *Proc. of International Particle Accelerator Conference (IPAC'17) Copenhagen, Denmark* (*International Particle Accelerator Conference* no 8) JACOW, Geneva, Switzerland (JACoW) pp 2589–2591 URL https://doi.org/10.18429/JACoW-IPAC2017-WEPAB014

[64] DESY. PETRA III - P07 - Overview (visited on 02/28/2023) URL https://photon-science.desy.de/sites/site_photonscience/content/e58/e176720/e177229/e178413/e314012/P07overview_eng.png

[65] Schell N, King A, Beckmann F, Fischer T, Müller M and Schreyer A 2014 The high energy materials science beamline (hems) at petra iii *Mechanical Stress Evaluation by Neutrons and Synchrotron Radiation VI* (*Materials Science Forum* vol 772) (Trans Tech Publications Ltd) pp 57–61 URL https://doi.org/10.4028/www.scientific.net/MSF.772.57

[66] DESY. PETRA III - P07 - Unified Data Sheet (visited on 02/25/2023) URL https://photon-science.desy.de/facilities/petra_iii/beamlines/p07_high_energy_materials_science/unified_data_sheet_p07/index_eng.html

[67] DESY. PETRA III - P07 - Experimental Setup (visited on 02/28/2023) URL https://photon-science.desy.de/facilities/petra_iii/beamlines/p07_high_energy_materials_science/p07___physics_and_chemistry_desy/experimental_setup/index_eng.html

[68] Kolanoski H and Wermes N 2020 *Particle Detectors: Fundamentals and Applications* (Oxford University Press) ISBN 9780198858362 URL https://doi.org/10.1093/oso/9780198858362.001.0001

[69] ORTEC 2019 quality Assurance Data Sheet (GEM-SP5020P4-B)

[70] Stöhlker T, Beyer H F, Bräuning-Demian A, Brandau C, Gumberidze A, Grisenti R E, Hagmann S, Herfurth F, Kozhuharov C, Kühl T, Liesen D, Litvinov Y, Maertin R, Nörtershäuser W, Kester O, Petridis N, Quint W, Schramm U, Schuch R, Spillmann U, Trotsenko S, Weber G and Winters D 2011 *AIP Conference Proceedings* **1336** 132–137 URL https://doi.org/10.1063/1.3586073

[71] Spillmann U private communication 2023

[72] Vockert M, Weber G, Bräuning H, Surzhykov A, Brandau C, Fritzsche S, Geyer S, Hagmann S, Hess S, Kozhuharov C, Märtin R, Petridis N, Hess R, Trotsenko S, Litvinov Y A, Glorius J, Gumberidze A, Steck M, Litvinov S, Gaßner T, Hillenbrand P M, Lestinsky M, Nolden F, Sanjari M S, Popp U, Trageser C, Winters D F A, Spillmann U, Krings T and Stöhlker T 2019 *Physical Review A* **99**(5) 052702 URL https://doi.org/10.1103/PhysRevA.99.052702

[73] Krings T 2016 Semikon Detector GmbH / Forschungszentrum Jülich. documentation of the 2D-SiLi detector system (ST-16-1) Private communication 2023

[74] Blumenhagen K H, Spillmann U, Gaßner T, Gumberidze A, Märtin R, Schell N, Trotsenko S, Weber G and Stöhlker T 2015 *Physica Scripta* **2015** 014032 URL https://doi.org/10.1088/0031-8949/2015/T166/014032

[75] Weber G private communication 2022

[76] James F 2006 *Statistical Methods In Experimental Physics (2nd Edition)* (World Scientific Publishing Company) ISBN 9789813101845

[77] Weber G, Bräuning H, Surzhykov A, Brandau C, Fritzsche S, Geyer S, Grisenti R E, Hagmann S, Hahn C, Hess R, Hess S, Kozhuharov C, Kühnel M, Märtin R, Petridis N, Spillmann U, Trotsenko S, Winters D F A and Stöhlker T 2015 *Journal of Physics B: Atomic, Molecular and Optical Physics* **48** 144031 URL https://doi.org/10.1088/0953-4075/48/14/144031

[78] Altmann S L 2005 *Rotations, Quaternions, and Double Groups* (New York, United States: Dover Publications Inc.) ISBN 978-0-486-44518-2

[79] Rao K S 1988 *The rotation and Lorentz groups and their representations for physicists* (New York: Wiley) ISBN 9780470210444

[80] Hirayama H, Namito Y, /KEK T, Bielajew A F, Wilderman S J, U M, Nelson W R and /SLAC 2005 URL https://doi.org/10.2172/877459

[81] Meitner L and Kösters H 1933 *Zeitschrift für Physik* **84** 137–144 URL https://doi.org/10.1007/BF01333827

[82] Schumacher M 1999 *Radiation Physics and Chemistry* **56** 101–111 ISSN 0969-806X URL https://doi.org/10.1016/S0969-806X(99)00289-3

[83] Weber G 2010 *Untersuchung zur Anisotropie und linearen Polarisation radiativer Prozesse in energiereichen Ion-Atom-Stößen* Ph.D. thesis Ruprecht-Karls-Universität Heidelberg URL https://doi.org/10.11588/heidok.00010759

[84] Heß S 2010 *Compton-Polarimetrie mit ortsauflösenden Röntgendetektoren* Ph.D. thesis Johann Wolfgang Goethe-Universität Frankfurt a. M. URL https://publikationen.ub.uni-frankfurt.de/frontdoor/index/index/start/0/rows/10/sortfield/score/sortorder/desc/searchtype/simple/query/Compton+-+Polarimetrie+mit+ortsauflÃűsenden+RÃűntgendetektoren/docId/7496

Selbstständigkeit und Veröffentlichung

Hiermit erkläre ich, die vorliegende Arbeit selbstständig verfasst, und keine anderen als die im Literaturverzeichnis angegebenen Quellen und Hilfsmittel verwendet zu haben.

Vonseiten des Verfassers bestehen keinerlei Einwände, diese Arbeit der Thüringer Universitäts- und Landesbibliothek zur öffentlichen Nutzung zur Verfügung zu stellen.

Jena, den 6. Juli 2023

                                                  _____

Tobias Over